TÉCNICO LISBOA

Observability analysis and optimization of autonomous orbit determination through relative sensing

Pedro Rocha Cachim

Thesis to obtain the Master of Science Degree in

Aerospace Engineering

Supervisors: Prof. João Pedro Castilho Pereira Santos Gomes
Prof. Rodrigo Martins de Matos Ventura

Examination Committee

Chairperson: Prof. Paulo Jorge Coelho Ramalho Oliveira
Supervisor: Prof. João Pedro Castilho Pereira Santos Gomes
Member of the Committee: Dr. Nuno Ricardo Salgueiro Filipe

October 2020

Acknowledgments

The process of writing this thesis was the final and greatest challenge of my six years of academic studies at IST and ISAE-SUPAERO. I was very fortunate to have the support of my supervisors, João Pedro Gomes and Rodrigo Ventura, who diligently accompanied me through this endeavour. For their availability, patience and guidance, I express my endless gratitude.

I would also like to thank Jeffrey Stuart for his kindness in clarifying some questions regarding the SunRISE mission concept, and Nuno Filipe, for accepting the call to take part in the thesis defense and providing invaluable feedback.

To my friends, I also wish to show my gratitude, specially to those who kept me company both in Lisbon and Toulouse, for making the hardships along the way more endurable and the moments of celebration more rewarding.

Finally, I want to thank my family for their constant moral and emotional support, particularly in face of the unique challenges posed by the months of epidemic-induced isolation, which were much easier to endure in their close company.

Resumo

O conceito de formações de satélites em proximidade tem vindo a consolidar-se fortemente na última década, nomeadamente pelo seu potencial de reduzir custos, revolucionar aplicações como a interferometria e radares de abertura sintética e de abrir as portas a novos conceitos de missões científicas.

O método mais frequente de determinação de órbita de formações em missões próximas da Terra tem sido baseado no sistema GPS. Para conceitos de formações para fora da zona de influência da gravidade terrestre, os métodos propostos consistem na utilização de medições de telemetria com estações de solo. No entanto, este método não permite realizar localização em tempo real. Para além disso, as medições com estações de solo ou constelações de satélites tornam-se indisponíveis se a formação for eclipsada por outro corpo celeste.

Um método alternativo de localização autónoma e em tempo-real consiste no uso da evolução de medições de posição *relativa* num referencial inercial entre os satélites de uma formação para estimar a posição *absoluta*. Nesta tese, o conceito da missão *SunRISE* será usado para exemplificar a funcionalidade deste método. Seguidamente, um estudo de otimização será feito para posicionar um novo satélite de maneira a maximizar a precisão do sistema de localização. Finalmente, será feito um estudo sobre a possibilidade de remover o sistema de medição de orientação da posição relativa entre os elementos da formação no referencial inercial mantendo a observabilidade da posição absoluta dos mesmos, e o desempenho resultante será avaliado e comparado com os resultados do sistema de posicionamento relativo completo.

Palavras-chave: formações de satélites, posicionamento relativo, estudo de observabilidade, optimização de trajetória

Abstract

The concept of spacecraft flying formations has been consolidating itself over the last decade, mainly for its potential in reducing mission costs, revolutionizing applications such as interferometry and synthetic aperture radars, and opening the door to new scientific mission concepts.

The most frequent orbit determination method for these formations has been based on the use of GPS receivers. For Flying Formation (FF) concepts outside the range of GPS signals, proposed methods are based on telemetry with ground stations. However, this type of methods does not allow for real-time positioning. Moreover, such measurements may also become unavailable if the FF is eclipsed by another body.

An alternative real-time autonomous localization method consists in measuring the time evolution of *relative* position in an inertial frame between the spacecraft in the formation to estimate their *absolute* position. In this thesis, the *SunRISE* mission concept will be used to exemplify a potential use for this method. With this template, an optimization study will be made to place a new satellite in order to maximize the precision of the positioning system. Finally, a new study will be done on the possibility of removing the relative bearing measurement system from the spacecraft in the formation while maintaining the observability of their absolute position, and the resulting performance will be evaluated and compared with the complete relative positioning system.

Keywords: spacecraft formation flying, relative positioning, observability study, trajectory optimization

Contents

List of Tables

List of Figures

Nomenclature

Greek symbols

α	Angular radius of eclipsing object.
β	Angular radius of eclipsed object.
γ	Angular distance between eclipsing and eclipsed object.
μ	Gravitational parameter.
ψ	Right ascension angle.
ρ	Range measurement.
σ	Standard deviation.
θ	Declination angle.

Roman symbols

C_r	Coefficient of reflectivity.
$\mathcal{L}$	Lie derivative.
$\mathcal{O}$	Observability Matrix.
r	Position vector.
v	Velocity vector.
x	Position and Velocity vector.

Subscripts

$\odot$	Sun parameter.
$\oplus$	Earth parameter.
i, j, n	Spacecraft indexes.
k	Time sample index.
m_i	Third body parameter.

x, y, z Cartesian components.

Superscripts

(m) mth-order time derivative.

* Adjoint.

+ *A posteriori*.

- *A priori*.

. First-order time derivative.

T Transpose.

Glossary

AOA	Angle-Of-Arrival
CEPE	Predict–Evaluate–Correct–Evaluate
CN	Condition Number
COE	Classical Orbital Elements
CoM	Center of Mass
DST	Dynamical Systems Theory
ECEF	Earth Centered Earth Fixed
ECI	Earth Centered Inertial
EKF	Extended Kalman Filter
FF	Flying Formation
GEO	Geostationary Orbit
GNC	Guidance, Navigation and Control
GNSS	Global Navigation Satellite System
GPS	Global Position System
ISL	Inter-Satellite Link
JAT	Java Astrodynamics Toolkit
JPL	Jet Propulsion Laboratory
LEO	Low Earth Orbit
LI	Local Inertial
LOS	Line-Of-Sight
LUI	Local Unobservability Index
LVLH	Local-Vertical Local-Horizontal
LiAISON	Linked Autonomous Interplanetary Satellite Orbit Navigation
MMS	Magnetospheric Multiscale
ODTBX	Orbit Determination ToolBoX
OG	Observability Gramian
PRISMA	Prototype Research Instruments and Space Mission technology Advancement
PSO	Particle Swarm Optimization

PVA	Position-Velocity-Acceleration
RF	Radio Frequency
RMSE	Root Mean Squared Error
SAR	Synthetic Aperture Radar
SFIM	Standard Fisher Information Matrix
SR-SFIM	Square Root Standard Fisher Information Matrix
STM	State Transition Matrix
SunRISE	Sun Radio Interferometer Space Experiment
UHF	Ultra High Frequency
WLS	Weighted Least Squares

Chapter 1

Introduction

1.1 Motivation

Over the last few decades, a great focus has been given to the goal of reducing the costs of space exploration missions. Among the new concepts and developments being studied for this purpose, formation flying may prove to be one of the most important technological shifts to influence the space industry. The interest in Flying Formations stems from the ability to divide the payload and operational functions of a spacecraft between several elements [1].

The fractioning of a large, monolithic satellite into several small satellites should not only lead to a reduction in cost, but also to an enhanced reliability of the mission, since the loss of one element would not necessarily lead to the collapse of the system [2]. Furthermore, FF can extend the realm of possible science missions that would otherwise be impractical with a single spacecraft [3]. Applications that require large and precise baseline separations such as interferometry [4] and gravimetry [5] could particularly benefit from the flexibility and reliability of FF [1].

One of the most challenging aspects of spacecraft FF missions is the design of on-board guidance, navigation and control (GNC) techniques [6]. So far, the navigation solutions adopted by most FF missions have relied on GNSS receivers. Even in the Magnetospheric Multiscale (MMS) mission, in which the formation reached orbital apogees extending as far as 25 times the Earth's radius, opted to use a GPS receiver tuned to acquire low strength GNSS signals to allow for positioning at high altitudes [7]. In deep space missions, absolute positioning/orbit determination usually relies on ground station telemetry [8].

However, ground station telemetry in deep space missions does not allow for real-time observation of the spacecraft's absolute position and velocity due to the time delay. For certain missions, such as those that involve the landing of equipment on a planet's surface, that time delay becomes a considerable predicament [9]. Overcoming this challenge will require autonomous, real-time navigation methods.

Seeking to find a solution to the previous problem, Markley demonstrated that knowledge of the time history of the relative positioning of the spacecraft in a formation within an inertial frame of reference can allow for the observation of their absolute position [10]. This method has since been extensively

researched in the literature, as it provides an autonomous and real-time means of observing the absolute position, regardless of the distance or visibility to the ground stations or GPS constellation. Previous studies have looked into its potential performance for martian [11], lunar [12] and asteroid [13] FF missions. Despite the extensive research demonstrating the feasibility of this autonomous navigation method, it is yet to be implemented in practice.

In order to fully explore the full potential of this method, it is useful to understand how the orbital configuration of the spacecraft in the formation impacts the positioning performance. Developing an effective optimization strategy to maximize the positioning accuracy would prove particularly useful for the trajectory design of future FF concepts seeking to implement this navigation solution.

Minimizing the sensor suite required for this navigation solution could also help to make it a more appealing choice for future FF mission concepts. In order to observe the spacecraft's relative position, both ranging and bearing measurement systems are necessary. In a formation with more than two elements, not all of the ranging and bearing systems may be necessary for the navigation solution to work [14, 15]. Understanding the redundancy of these systems may provide a way to cut mission costs.

1.2 Thesis Objectives

In order to contribute to the research effort around the relative positioning autonomous navigation method proposed in [10], this study firstly seeks to evaluate the performance of this solution, namely its stability, speed of convergence and accuracy. We intend to perform this evaluation in an environment where the method may be competitive with alternative navigation solutions.

Secondly, we propose to study which orbital configuration for an additional spacecraft of a FF maximizes the gains in terms of observability/performance of the system, considering different measurement systems for the new spacecraft. Our goal is to test and compare novel objective functions to determine which would more accurately predict the performance of the navigation system without being too computationally heavy. We aim to study the impact of the additional spacecraft's orbital configuration on said objective functions in order to understand how it affects the system's performance.

Finally, this study also aims to find a redundancy in the sensor suite of the relative positioning autonomous navigation solution that can be eliminated to reduce costs. More specifically, we aim to study how many relative bearing measurement systems can be removed from a FF's navigation sensor suite while conserving the method's observability.

1.3 Contributions

This work yielded a number of contributions to the method of autonomous navigation through relative positioning. More specifically, the following was achieved:

- An evaluation of the performance of an EKF based on the relative positioning autonomous navigation method in the context of a FF mission concept above the GNSS belt;

- A comparison of said performance with that of other proposed navigation solutions for the mission concept, demonstrating its potential to achieve superior relative positioning accuracy;
- An optimization study for the placement of a new spacecraft in the formation in an orbital configuration that maximizes the accuracy of the autonomous navigation method;
- A comparison of the optimization results with different objective functions based on the Observability matrix and Square Root Standard Fisher Information Matrix, considering different measurement systems and constraints;
- Study on the impact of certain orbital parameters of the new spacecraft on the objective functions;
- Study on the observability of the autonomous navigation method when all pairs of spacecraft have access to relative ranging measurements but only one pair has access to relative bearing measurements;
- Assessment of the optimization results and the sensor-reduced system's observability in a simulation environment.

1.4 Thesis Outline

In the present Chapter 1, we provide a brief introduction to the work. After presenting motivating reasons to study the method of absolute positioning through relative position measurements, we briefly define the proposed problems and achievements of the thesis.

In Chapter 2, we overview some background for our solution. A summary of the fundamentals of satellite navigation is presented, followed by an overview of spacecraft formation flying. We also introduce the topic of observability analysis and evaluation, as well as the *SunRISE* mission and its associated positioning requirements.

In Chapter 3, an overview is given of the previously proposed navigation solutions for the *SunRISE* mission concept. These will be used as a benchmark for the newly proposed navigation solution that uses relative position measurements to estimate the absolute position. In the final section of this chapter, the performances of these solutions are compared.

The observability/performance optimization study is described in Chapter 4, as well as the observability study for the relative bearing reduced system. While the resulting orbital configurations of the optimization problems are shown and discussed in this chapter, the simulation results for both of these studies are presented in detail in Chapter 5.

Finally, Chapter 6 presents a summary of the conclusions drawn from the studies throughout this Thesis and suggestions are given on the potential developments of this line of work.

Chapter 2

Background

2.1 Fundamentals of Satellite Navigation

The operation of a spacecraft in orbit is heavily dependent on one's ability to locate and communicate with it, regardless of its level of autonomy. Navigation is therefore a critical aspect of spacecraft operations [8]. In this work, we refer to navigation has the process of determining/predicting the trajectory and/or orientation of a spacecraft. Any navigation done by a spacecraft based on capabilities resident within that spacecraft and without ground intervention is considered autonomous [16].

For satellite navigation, 3 classes of sensors are tipically used [17]:

- Inertial sensors (p.e. accelerometers and gyrometers), which measure variations in movement with respect to the inertial space without any field-of-view or link to ground-station, satellite or local force fields;
- Position/navigation sensors, used to observe the spacecraft motion relative to known spatial references, such as ground stations or other satellites (GNSS);
- Attitude sensors, which observe the spacecraft orientation with respect to a frame of reference characterized by visible references, such as the Sun, Earth, and stars, requiring therefore a field-of-view to observe these objects (Sun and Earth sensors, star trackers). As an alternative, they may also couple with some local field to observe the orientation (p.e. measuring the Earth's magnetic field with magnetometers).

In this study, special focus will be given to position/navigation sensors and orbit determination.

2.1.1 Spacecraft Positioning Systems

In order to perform orbit determination of an artificial satellite, it is necessary to have access to measurements that allow for the observation of the satellite's position or velocity. These measurements are tipically based on the observation of properties of electromagnetic wave propagation transmitted between the satellite and a tracking system. The most common types of tracking systems used for spacecraft nav-

igation are radar tracking, laser tracking and GNSS [8]. Another interesting concept worth mentioning is the use of X-ray Pulsars for deep space navigation, which is also briefly reviewed in this section.

Radar tracking

Radar techniques have been used to observe the position and velocity of spacecraft since the early times of spaceflight. Ground stations can perform 3 types of measurement: the *pseudo-range* to the spacecraft through round-trip travel time of a radar signal emitted from the ground station antenna to the satellite and re-transmitted back to the station; the *pointing angle* towards the spacecraft that is obtained by measuring the direction of the maximum amplitude of the spacecraft's signal; and the *range rate* of the spacecraft relative to the ground station can be derived from the Doppler shift of the round-trip radar wave [8].

Radar tracking is the conventional way to obtain data for orbit determination of deep space missions. While this technique may provide very accurate range measurements in the Earth-spacecraft direction, its fixed angular resolution leads to large errors in the perpendicular plane that grow with the distance between the spacecraft and the Earth [18].

Laser tracking

Satellite Laser Ranging (SLR) is a technique similar to radar tracking, in which a laser, rather than a radar signal, is emitted from a ground laser station to retro-reflectors equipped on-board of a spacecraft to obtain a precise measurement of its distance to the station. Several laser tracking networks have been deployed since the technique's early demonstrations in the 1960s, together with a steady improvement of its accuracy [8].

SLR data is particularly useful for applications requiring a high degree of accuracy, such as in the fields of crustal dynamics, gravimetry and Earth rotation parameter estimation. SLR has also contributed to the development of precise satellite motion dynamic models and the calibration of more innacurate tracking instruments [19]. One drawback that SLR presents, however, is its dependence on the availability of high-precision "predicted" knowledge of the spacecraft's trajectory for antenna pointing. Furthermore, the use of SLR is also limited by the weather at the laser stations, as well as the operations schedule of the ground segment [8].

Global Navigation Satellite System

Global Navigation Satellite Sytems (GNSS) are systems of satellites that broadcast signals carrying precise information on their position and time, obtained from the on-board atomic-clock time-standard. These in turn can be used for autonomous absolute positioning through multi-lateration. GNSS signals provide 3 types of measurement [20]:

- Pseudo-range: Measure of the difference between the receiver clock time upon the signal arrival and the GNSS satellite clock time upon signal transmission. By multiplying this difference by the

speed of light, an observation of the satellite-receiver distance is obtained. The asynchronity of the two clocks and some other delays lead to a precision that is tipically in the dm-range;

- Carrier phase: Measure of the instantaneous signal phase and the amount of zero-crossings obtained after having the signal mixed with another of nominal frequency. The evolution of carrier phase measurements over time reflects that of the pseudo-range, although ≈ 2 orders more precise than the latter. If the tracking is interrupted, the accumulated cycle count is lost in what is called a cycle slip. This is a result of the information provided by a carrier phase measurement on the pseudo-range being ambiguous by an integer multiple of one cycle;

- Doppler: The ratio between the measured signal frequency by the receiver and that of the signal upon transmission provides information on the range-rate/line-of-sight velocity due to the Doppler effect.

GNSS signals can also be used for the relative positioning of different spacecraft through differential GNSS positioning or DGNSS, akin to the terrestrial case of a GPS receiver on a vehicle that is positioned with respect to a reference station. The difference in pseudo-range and carrier phase measurements provides information on the relative position of the spacecraft, and also allows for the elimination and reduction of part of its bias. The space-borne case has one main advantage, however: while the motion of a terrestrial vehicle is generally unpredictable, the relative dynamics between two spacecraft in orbit can be modelled and predicted to a high degree of accuracy [21].

GNSS signals have been the most common localization method for earth-centered FF. Formations like PRISMA and CAN-X 4/5 achieved meter level absolute positioning and cm-level relative positioning [6].

Pulsar X-ray

Among the potential celestial x-ray sources, X-ray emitting pulsars represent a subset that can be used as reference in a spacecraft's x-ray based navigation system [22]. One example of how such can be accomplished is provided in Figure 2.1.

Given the celestial source of these signals, pulsars provide good coverage throughout the solar system, and conceivably beyond it. Most importantly, they exhibit great potential in reducing the LOS perpendicular error from radar tracking and increasing the overall navigation performance [22].

The ability to accurately position a spacecraft through these signals could help to increase the autonomy of spacecraft operations and navigation. X-ray pulsars have the potential to not only correct the spacecraft's time and position, but also its attitude, therefore providing a complete navigation solution. This makes them an attractive choice for a new celestial-based spacecraft navigation system [22].

The only precedent for this positioning method was established by the XPNAV-1 mission, which achieved an average navigation error of $38.4\,\mathrm{km}$ [24].

Recent studies estimate craft positioning uncertainties of ~ 5 and $\sim 1.5\,\mathrm{km}$ in the direction of the pulsar can be achieved, with a sampling time of $T_{obs} = 5 \times 10^3\,\mathrm{s}$ and $5 \times 10^4\,\mathrm{s}$ respectively [25].

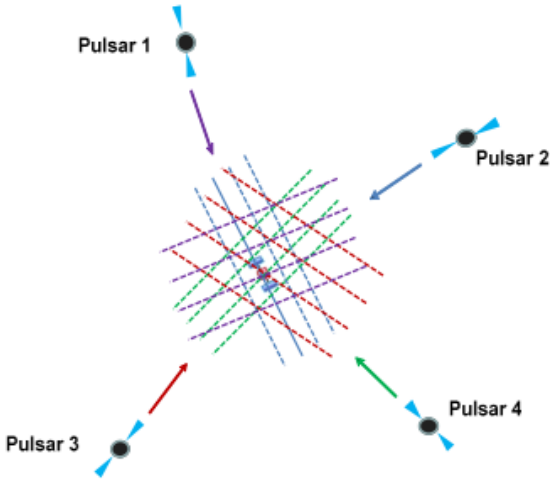

Figure 2.1: Absolute navigation through the simultaneous observation of the pulse phase of four pulsars. This represents the minimum amount of measurements required to observe the spacecraft's position and on-board clock time-offset error. The dashed lines represent the positioning ambiguity of each pulse phase observation, separated by the pulsar's wavelength [23].

Although pulsar navigation will not outperform GNSS navigation where navigation satellite signals are available, it could become practical as a complement/alternative to radar/laser tracking in deep space missions. The key advantages for pulsar navigation are the potential for increased autonomy from Earth-based systems and that, unlike with ground tracking, pulsar navigation does not grow more innacurate the further away the spacecraft is from the Earth [25].

2.1.2 Reference frames

In order to describe an earth-centered positioning problem for a multi-satellite mission, it is necessary to introduce the frames of reference that will be used to describe the motion of the spacecraft, be it in an absolute or relative frame.

Earth Centered Inertial coordinate system

For near-Earth spacecraft, the ability to describe the geocentric (Earth-centered) system as an inertial reference frame can significantly simplify the dynamic models from which the velocity and acceleration components can be derived [1]. The ECI coordinate system fits this purpose, being centered on the Earth's center of mass, with the axis fixed with respect to the stars. The fundamental plane of this system aligns with the equator, and the unit vector x is aligned with the direction of the vernal equinox. The z axis is aligned with the Earth's axis of rotation, and the y axis is the vector orthonormal to x and z that completes the triad for a right-handed system.

The equatorial plane is not fixed with respect to the celestial sphere, however. Due to the Earth's shape and the gravitational pull of the Sun and the Moon, the Earth's equatorial plane presents oscillations relative to the celestial sphere. Since the x-axis is defined with respect to the celestial sphere and the z-axis relative to the equatorial plane, the ECI is therefore not truly inertial [26]. This can be solved by defining the orientation of the axis for a fixed instant in time (epoch). One commonly used ECI frame

is the J2000, which uses the orientation of the equatorial plane at 12:00 (UTC) on January 1, 2000. By fixing the orientation of the axis, the ECI can be considered inertial, and is particularly useful to describe the absolute states (position and velocity) of a spacecraft [27].

Earth Centered Earth Fixed system

It is useful to consider a frame of reference that is fixed with respect to the Earth's surface. Because the Earth rotates with respect to the ECI frame, of which the x-axis points the direction of the vernal equinox, this new frame of reference would need to present a similar rotation with respect to said frame. This ECEF (Earth-Centered Earth-Fixed) frame's z-axis also points to the geographic north, while its x-axis points to latitude $0°$, longitude $0°$ and its y-axis to latitude $0°$, longitude $90°$ [28]. Considering the Earth's fixed rotation speed $\omega_{\oplus}$, the ECEF frame corresponds to the ECI frame rotated of an angle θ_{GMT} around its z-axis, called the Greenwich Mean Time (GMT) [1].

Local Vertical Local Horizontal coordinate system

Within the context of formation flying, a local reference frame originating at a given spacecraft is necessary for the representation of the relative motion of the formation spacecraft with respect to each other. This spacecraft at the origin of a local frame is designated the chief spacecraft. The Local-Vertical Local-Horizontal (LVLH) reference frame is suited for this purpose. The x-axis of the LVLH frame is designated the radial track direction, and is aligned with the vector starting at the Earth's center of mass and ending at the chief spacecraft's position. The z-axis/cross-track direction points in the direction of the orbit angular momentum vector. Finally, the y-axis/along-track direction completes the triad through the right hand rule. For a chief spacecraft with known position vector r_c and velocity vector v_c, the orthonormal unit vectors for the LVLH frame are calculated as follows [1]:

$$\begin{cases} X_{LVLH} = \dfrac{r_c}{\|r_c\|}, \\ Y_{LVLH} = Z_{LVLH} \times X_{LVLH}, \\ Z_{LVLH} = \dfrac{r_c \times v_c}{\|r_c \times v_c\|} \end{cases} \tag{2.1}$$

This frame of reference is exemplified in Fig. 2.2:

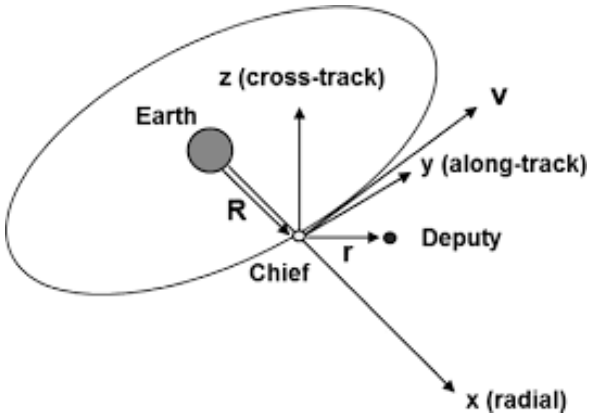

Figure 2.2: Local-Vertical Local-Horizontal frame [29]. The chief spacecraft is the one on which the LVLH frame is centered, while the remaining are the deputy spacecraft.

Local quasi-inertial coordinate system

The LVLH frame is useful to portray the movement of spacecraft in a local frame of reference. However, this frame of reference is not inertial, as it rotates along with the movement of the chief spacecraft along its orbit. A new inertial local reference frame is necessary to represent the movement of the spacecraft in the formation with respect to the chief spacecraft. For this purpose, another frame of reference will be used that will be centered on the chief spacecraft and have its axes aligned with those of the ECI frame. This local quasi-inertial frame of reference is not typically considered in the literature, the only example of which found by the author being in the reference [30]. For this work, this frame of reference will be abbreviated to LI (Local Inertial) frame.

2.1.3 Orbital mechanics

Using the reference frames described in the previous section, it is possible to describe the mathematical model of orbital dynamics necessary to predict the trajectory of a spacecraft as accurately as possible. This description will start with Kepler's laws and the two-body problem dynamics, and then move on to secondary perturbations that impact the spacecraft's movement.

Two-body problem

The fundamental laws that describe planetary motion were first developed by Johann Kepler. Paraphased from [31], these laws are:

- **Kepler's first law - The Elliptical Orbit Law** : The trajectory of a planet orbiting the Sun follows the shape of an ellipse, with the Sun being located in one of the ellipse's *focus*;
- **Kepler's second law - The Equal Area Law** : The area covered by the line drawn from the Sun to a planet for a fixed period of time is always constant;
- **Kepler's third law - The Law of Periods** : The square of the time it takes for a planet to complete a revolution around the Sun (orbital period) is proportional to the cube of the mean distance between

the Sun and the planet.

Kepler's discoveries describe the geometry of planetary motion, but not the reason behind it. A mathematical theory providing a justification to Kepler's findings would later be proposed by Newton, capable of explaining the orbital motion of a body around another [1].

According to Newton's laws, assuming a perfectly spherical Earth with uniform density, the equation of motion of a satellite in the ECI frame due exclusively to its gravitational force can be written as [32]:

$$\frac{d^2r}{dt^2} = -\frac{\mu_\oplus}{\|r\|^3}r, \tag{2.2}$$

where $\mu_\oplus$ is the product of the mass of the Earth and the Gravitational constant (valuing $3.986\,005 \times 10^{14}$ m^3s^{-2} in datum *WGS-84*), r is the position vector of the satellite in the ECI frame, and $\|r\|$ is the L2-norm of this vector. This applies to the so-called two-body problem or Keplerian satellite motion. Three assumptions need to be made for this approach to be valid. These assumptions (paraphrased from [1]) are:

- **Assumption 1 - The Massive Primary:** The mass of the orbiting satellite is much smaller and therefore negligible when compared to the mass of the central body;
- **Assumption 2 - Newtonian Dynamics:** The motion of the two bodies is described exclusively by the mutually attractive Newtonian gravitational forces;
- **Assumption 3 - Spherical Bodies:** Both bodies are treated as particle point masses, following the assumption that they are spherically symmetric.

However, several approximations need to be made to consider these assumptions. In reality, the Earth is not spherical nor symmetric, and the presence of other bodies in the vicinity, as well as other disturbing forces, mean that the true orbital dynamics is not restricted to the dynamics of the central body and the satellite [1]. Figure 2.3 shows the comparison of the average impact of the different forces on an orbiting satellite around the Earth, such as the Earth's gravitational force (marked GM), the harmonic coefficients that describe the assymetries of the Earth's gravity field (marked J_{ik}), the radiation pressure from both the sun and the Earth's albedo, the gravitational fields of other bodies in the solar system and atmospheric drag.

In the following sections, the main non-keplerian dynamic forces affecting spacecraft motion in Earth orbit will be described.

Gravity Potential Model

As already described, the keplerian two-body problem is built on the assumption that the Earth is spherically symmetrical. This is naturally an approximation, as the Earth presents an uneven shape and density distribution that distorts its gravity field. In order to describe a more complex gravity field than that of a point-mass or perfectly spherical body, the planet's gravity potential needs to be defined. We remind that the potential of a vector field is the integration over space of said field. Vice versa, the gravity

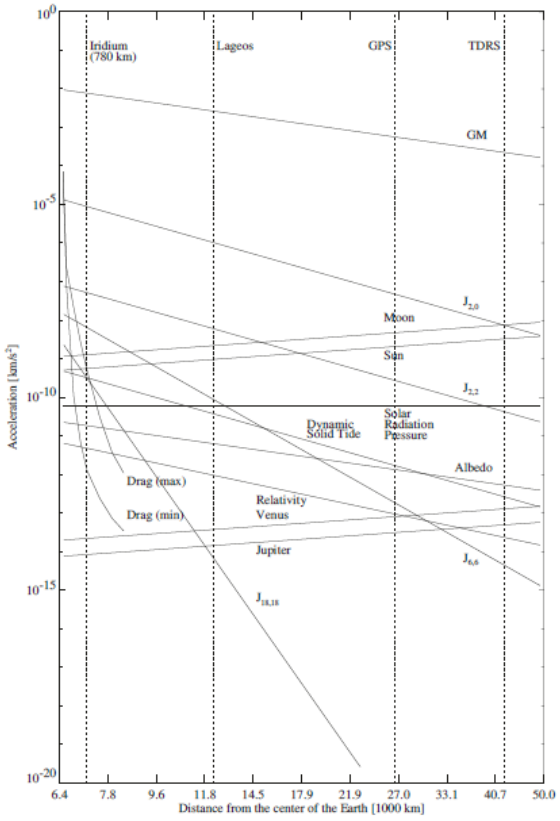

Figure 2.3: Comparison of the magnitude of different sources of acceleration on a spacecraft as a function of its distance to the Earth [8].

field is the spatial derivative of the gravity potential function, as shown in (2.3) (considering a spherically symetric model) [33].

$$g = -\frac{\mu}{r^2} = \frac{d}{dr}\left(\frac{\mu}{r}\right) = -\frac{d}{dr}U = -\nabla U(r) \tag{2.3}$$

The potential function for the gravity field of an uneven body can be described by the use of a spherical harmonics function $U(r, \theta, \psi)$ such that $U(r, \theta, \psi) = R(r)P(\theta)Q(\psi)$, where r, θ and ψ are spherical coordinates in a reference frame inertial with respect to the central body (in the Earth's case, the ECEF frame). They represent the radius, latitude and longitude, respectively.

This gravity potential function is defined as [33]

$$U(r,\theta,\psi) = -\frac{\mu}{r}\left\{1 + \sum_{n=2}^{N_z}\left(\frac{R}{r}\right)^n \widetilde{J}_n P_n^0(\sin\theta) + \sum_{n=2}^{N_t}\sum_{m=1}^{n}\left(\frac{R}{r}\right)^n P_n^m(\sin\theta)\left[\widetilde{C}_n^m\cos(m\psi) + \widetilde{S}_n^m\sin(m\psi)\right]\right\} \tag{2.4}$$

where R is the central planet's mean radius, P_n^0 are Legendre polynomials and P_n^m the associated Legendre functions, $\widetilde{J}_n$ are the zonal harmonics terms, $\widetilde{C}_n^m$ and $\widetilde{S}_n^m$ are the terms that compose the sectorial harmonics for $n = m$ and tesseral harmonics for $n \neq m$ and the terms N_z and N_t describe the degree and order, respectively, of the gravity potential model [33].

Figure 2.4 presents a visual representation of the behaviour of spherical harmonics:

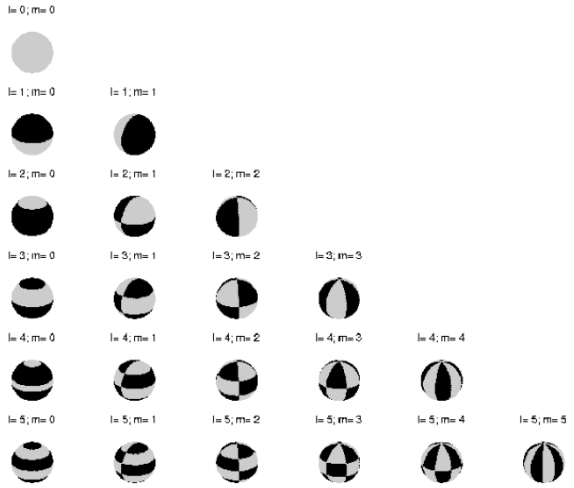

Figure 2.4: Visual representation of some spherical harmonics terms [33].

Ideally, the terms N_z and N_t in (2.4) would go up to infinity. In practice, computation requires the number of coefficients to be finite and for each model to present a certain degree of error.

Planetary Third-body Gravity

Newton's gravity model describes the gravitational pull exerted on one body by another to be inversely proportional to the distance between them. This implies that, while the gravitational force may weaken the further apart the bodies are, it never disappears entirely. This leads to the conclusion that the second assumption necessary for the keplerian motion approach to be valid can only be made as an approximation.

In earth orbit, the gravitational pull of the Sun and Moon tipically integrates the orbit prediction model. This third-body acceleration perturbation is usually modelled as [8]:

$$a_{m_i} = \mu_{m_i} \left(\frac{r_{m_i} - r}{\|r_{m_i} - r\|^3} - \frac{r_{m_i}}{\|r_{m_i}\|^3} \right) \tag{2.5}$$

in which a_{m_i} is the acceleration on the spacecraft due to the third-body, μ_i is the gravitational parameter of the third-body, r_{m_i} is the position vector of the third-body in the ECI frame, and r the position vector of the spacecraft in the ECI frame.

The Sun and Moon's ephemerides can be taken from an astronomical almanac such as *DE405*, and follow the low precision methods suggested by Montenbruck & Gill [8].

Solar Radiation Pressure

The exposure of a satellite to solar radiation impacts its trajectory due to the force produced by the change in momentum of the photons that are absorbed or reflected by the spacecraft. Unlike with the gravitational perturbations discussed up this point, this perturbation depends on the mass and exposed

surface area of the satellite [8]. The standard approach for modelling this effect is the cannonball model:

$$a_{SRP} = -\nu_{IF} P_{\odot} \frac{C_r A_s}{m} (AU)^2 \frac{r_{\odot} - r}{\|r_{\odot} - r\|^3}, \tag{2.6}$$

where a_{SRP} is the acceleration on the spacecraft due to the solar radiation pressure, ν_{IF} is the illumination factor, $P_{\odot}$ is the nominal solar radiation pressure at 1AU, C_r is the radiation pressure coefficient, A_s is the surface area exposed to solar radiation, m is the mass of the spacecraft, $r_{\odot}$ is the position vector of the sun with respect to the earth, and r the position vector of the spacecraft with respect to the earth [1].

The illumination factor ν_{IF} is included in (2.6) to determine the eclipse condition at which the Earth blocks the sun from view of the spacecraft.

The model adopted considers the shadow zone of the Earth to be axissymetrical and aligned with the sun-Earth position vector in the inertial frame. The spacecraft can be totally, partially or not eclipsed by the central body. In order to establish the conditions that identify the state the spacecraft is in, three variables need to be established. The first variable is the angle β that defines the apparent radius of the occulted body (i.e., the Sun) within the spacecraft's field-of-view [8]:

$$\beta = \arcsin\left(\frac{R_{\odot}}{\|r_{\odot} - r\|}\right), \tag{2.7}$$

where $R_{\odot}$ is the Sun's radius, r is the position of the spacecraft with respect to the central body in its inertial frame, and $r_{\odot}$ the position of the sun with respect to the central body in that same frame of reference. Secondly, we consider α, the apparent radius of the occulting body within the spacecraft's field-of-view:

$$\alpha = \arcsin\left(\frac{R}{\|r\|}\right), \tag{2.8}$$

where R is the radius of the central body. Finally, γ is the apparent separation between center of both the occulted and occulting bodies within the spacecraft's field-of-view:

$$\gamma = \arccos\left(-\frac{r}{\|r\|} \cdot \frac{r_{\odot} - r}{\|r_{\odot} - r\|}\right). \tag{2.9}$$

Figure 2.5 provides a visual representation of these 3 variables.

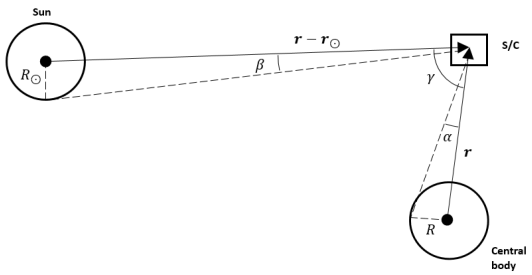

Figure 2.5: Visual representation of parameters α, β and γ used to determine the eclipse condition and illumination factor ν_{IF}.

If the apparent separation γ is greater than the sum of the apparent radius of the sun and the central body within the spacecraft's field-of-view, then there is no eclipse and $\nu_{IF} = 1$. If the apparent radius of the central body α is greater than its apparent separation to the sun γ and the sun's apparent radius β combined, then the spacecraft is fully eclipsed and $\nu_{IF} = 0$. The remaining scenario is the one in which the spacecraft is partially illuminated, and $\nu_{IF} = 1 - A/\alpha^2\pi$, where the solid angle of the eclipsed portion of the star in the spacecraft's field-of-view is given by

$$A = \beta^2 \arccos\left(\frac{x}{\beta}\right) + \alpha^2 \arccos\left(\frac{\gamma - x}{\alpha}\right) - \gamma y, \tag{2.10}$$

where in turn

$$y = \sqrt{\beta^2 - x^2} \tag{2.11}$$

and

$$x = \frac{\gamma^2 + \beta^2 - \alpha^2}{2\gamma} \tag{2.12}$$

In short, the illumination factor is determined by the position of the sun and the central body relative to the spacecraft as shown below [8].

$$\nu_{IF} = \begin{cases} 0, & \text{if } \alpha > \gamma + \beta \\ 1, & \text{if } \gamma > \beta + \alpha \\ 1 - \dfrac{A}{\alpha^2\pi}, & \text{otherwise.} \end{cases} \tag{2.13}$$

Atmospheric Drag

The most significant non-keplerian perturbations affecting low Earth orbit spacecraft motion are a result of atmospheric forces. These forces are difficult to model, however, due to three main reasons: the accuracy of the available data on the density of the upper atmosphere, the need to account for the interaction of the neutral gas and charged particles in the atmosphere with the different surfaces of the spacecraft, and also the impact of the attitude of a non-spherical spacecraft on these forces [8].

The modelling of the effect of atmospheric forces on spacecraft dynamics can be simplified by not considering the atmospheric lift and binormal forces, which are negligible when compared to atmospheric drag. The latter can be modelled as a force acting on the spacecraft in the opposite direction of the spacecraft's velocity vector with respect to the atmosphere:

$$a_{AD} = -\frac{1}{2} C_D \frac{A}{m} \rho \|v - v_{atm}\| (v - v_{atm}), \tag{2.14}$$

where C_D is the spacecraft's drag coefficient, A is the cross-sectional surface of the spacecraft being hit by the atmosphere, m is the mass of the spacecraft, ρ the atmospheric density, and v and v_{atm} are the spacecraft and atmosphere's velocity vectors, respectively. One common approximation that is made regarding the atmospheric velocity is to assume that it follows the Earth's rotation ($v_{atm} = \omega_\oplus \times r$), which equates to the atmosphere being motionless in the ECEF frame [8].

2.2 Spacecraft formation flying

Multiple definitions have been proposed for the concept of formation flying accross the literature. In this thesis, we will consider the definition proposed by NASA's Goddard Space Flight Center and mentioned in [28], describing formation flying as "The tracking or maintenance of a desired relative separation, orientation or position between or among spacecraft".

Several missions have been flown since the 1990s using the concept of formation flying for applications such as astronomy, communications and weather observation. These past flying formation missions have successfully demonstrated and validated the advantages and significance of this concept. These advantages can be summarized in the following main points [2]:

- *System cost reduction*: The design and manufacture of multiple smaller spacecraft through standardized processes results in a lower production cost when compared to that of a large monolythic spacecraft. Furthermore, there is the potential to cut launch costs due to the smaller size of the spacecraft. The maintenance cost of the system can also be reduced, as the need to replace a malfunctioning satellite can be more cheaply and quickly fixed;

- *System performance improvement*: The use of multiple spacecraft leads to an inherent level of redundancy in resources that can improve the robustness of the system. It may also lead to an increased level of autonomy from ground stations and of the GNC subsystem. Finally, the need to distribute and parallelize tasks between the multiple formation elements can improve the system efficiency.

- *System reliability enhancement*: The coordenative control design of a network of formation flying spacecraft can be implemented in modules with standardized communication and control components. This makes it possible for the system to remain operational if one or more of the spacecraft halt their functions, since only the links related to these inoperative elements will be affected.

2.2.1 Formation keeping

Spacecraft formations can be categorized according to their relative coordination scheme and formation keeping. The main types of formation coordination approach are the following [28]:

- *Orbit tracking*: In orbit tracking missions, each satellite in the formation is controlled with respect to a pre-determined reference orbit, with occasional station-keeping manoeuvers to keep them on track. This approach presents the advantage of increasing the autonomy each spacecraft in the formation has from the remaining elements in their formation keeping strategy;

- *Leader/follower*: In the leader/follower coordination approach, one leader spacecraft is designed to follow a given orbit, and the remaining follower spacecraft are designed to control their states with respect to the leader. The task of the follower spacecraft of maintaining their relative states is made easier due to the reference point being a spacecraft that is subjected to a similar dynamic

environment. Examples of previous formations following this configuration are the Can-X 4 and 5 precision control demonstration [34] and the PRISMA mission [35];

- *Virtual structure*: In a virtual structure formation keeping approach, the spacecraft in the formation are controlled as a single structure. This approach has a particular interest for applications such as interferometry, in which it may be more practical to treat the formation as a single rigid body [36];
- *Swarming*: The concept of swarming consists in the arrangement of a large number of vehicles based on locally available information. This approach has the advantage of scalability [28], and may serve potential applications such as optical relays or massively distributed sensing applications. SWIFT is the most discussed concept for spacecraft swarms in the literature. The feasibility of this concept relies on the development of the technology required to build a 100g class of spacecraft that can be actively controlled in all six degrees of freedom at a low cost-per-unit [37].

2.2.2 Cooperative Localization Systems

The positioning systems described in Section 2.1.1 allowed for the measurement of the absolute position of a spacecraft, as well as relative position between spacecraft through differential methods. Some positioning systems, however, serve exclusively the purpose of relative positioning within a multi-satellite mission. Since this thesis will focus on the use of relative positioning history to estimate the absolute position, an overview is given of relative positioning systems apt for use in spacecraft formations.

Vision-based system

Vision-based systems are a key technology for relative navigation and attitude determination in FF's, especially in close proximity. These systems are described as active if they are equipped with laser range finders to illuminate retroreflectors mounted on the tracked satellite. The target spacecraft is considered cooperative from the navigation standpoint if it is equipped with LEDs or reflectors meant to ease the chaser's camera imaging. These systems require techniques and algorithms capable of extracting features of the tracked satellite in order to determine its relative position and orientation [38]. An example of a previously flown and tested FF vision-based system is the PRISMA mission's VBS system [6].

RF crosslinks

The use of Radio Frequency (RF) technology for relative navigation shows great potential, both for geocentric and deep space missions. RF-based systems aim to estimate the relative states between spacecraft through the use of range and range rate measurements between a transmitter and receiver equipped on-board separate spacecraft [38]. The ability of RF signals in the microwave bandwidth to pass through certain physical barriers is a particularly appealing feature of RF communication. However, it is also a challenge to achieve a sufficient data rate for RF communications due to the available bandwidth's costly budget and the rate at which power consumption rises with greater distances and data transmission [39].

RF-based navigation systems generally use a transmitter, receiver and several antennas. Coarse distance estimates (meter-level) can be obtained with pseudo-range measurements. Finer distance and line-of-sight estimates can also be obtained by combining carrier phases with the pseudo-range [6].

The FFRF sensor on the PRISMA mission sucessfully demonstrated this technology. The system could provide range and LOS measurements with an operational range from $10\,\mathrm{m}$ to $10\,\mathrm{km}$ and could be used for up to 4 spacecraft. It achieved accuracies under $1\,\mathrm{cm}$ alongtrack and $\sim 33\,\mathrm{cm}$ crosstrack for an inter-spacecraft distance below $1\,\mathrm{km}$ [6].

Another promising technology for RF crosslink navigation is the *GAMALINK*, an advanced Software-Defined Radio (SDR) communications platform for space vehicles developed by *Tekever Space-Sistemas Espaciais, Lda*[1], which provides simultaneous support for different types of ground and inter-satellite links. *GAMALINK* was initially developed for use in small satellites. Besides its main functions, it is also capable of attitude determination, GNSS receiving, ranging and clock synchronization [40]. It has already been used in the 3 CubeSat constellation mission TW-1 [41], and a newer version is being developed for the PROBA-3 mission[2].By the end of the mission, a deep space qualified ISL (Inter-Satellite Link) version of *GAMALINK* will be available for use in other deep space missions.

Laser-based system

Laser systems operate similarly to RF systems, only with a signal at a different wavelength (tipically on the order of $1000\,\mathrm{nm}$, depending on the available laser technology). The transmission of a signal from an emitter equipped on a spacecraft to an optical reflector on the tracked spacecraft and its subsequent reflection allows for the observation of range, range-rate and LOS. The latter can be observed by scanning the incoming signal to determine the direction from which it is being received [6].

The operational range of these systems can range from below $1\,\mathrm{m}$ to a few kilometers, with an accuracy ranging from the mm to the cm-level. Their high precision compared to the other relative navigation sensors comes at the expense of a greater mass, power consumption and cost [6].

2.3 System Observability Analysis

As stated previously, in this thesis special focus will be given to the use of relative position measurements to estimate the absolute position of a spacecraft within a formation. For this reason, it is important to go over the methodology that is used to demonstrate that a given system is capable of observing the states in question, as well as quantifying how well it observes them. We will therefore survey the typical tools used in the literature to study a system's observability, and the metrics that are used to quantify it. Then, we shall use these tools to demonstrate how relative positioning measurements between spacecraft over time allow for the estimation of their absolute position.

[1] `http://space.tekever.com/` (Last accessed 18/06/2020)
[2] `https://directory.eoportal.org/web/eoportal/satellite-missions/p/proba-3` (Last accessed 18/06/2020)

2.3.1 System Observability

In order to understand the reasoning behind the tools used to study observability, it is important to establish the definition of observability. Let us consider the observed dynamical system

$$\dot{x}(t) = f(t, x(t)) \tag{2.15a}$$

$$y(t) = h(t, x(t)) \tag{2.15b}$$

where $x(t)$ is a n dimensional vector and $y(t)$ a p dimensional vector, n being the number of states in the system and p the number of observations. $x(t)$ is assumed to belong to a C^ω (analytic) n-dimensional manifold M (p.e. $\mathbb{R}^n$), and h is a C^ω map from M into $\mathbb{R}^p$. Considering $\gamma(t, x_0)$ to be the solution to (2.15a) at time t with initial condition $\gamma(0) = x_0$. $x_1, x_2 \in M$ are said to be *indistinguishable* (with respect to the set $\sum$ of domains of functions f, h and trajectory γ) if

$$h(\gamma(t, x_1)) = h(\gamma(t, x_2)) \tag{2.16}$$

for every $t \geq 0$, for which both sides are defined. Otherwise, they are *distinguishable* (with respect to $\sum$). The set $\sum$ is considered to be locally observable at $x \in M$ if there is a neighborhood U of x such that, for every $y \in U$, x and y are *distinguishable* [42].

Observability matrix

Several tools and methods exist to study the observability of a system. The most common tool for checking local observability (or local weak observability according to [43]) is the observability rank condition [44]. This condition is met when the observability matrix $\mathcal{O}$ has rank equal to the number of states n. The observability matrix can be described as the Jacobian of the observation equations and respective derivatives with respect to the states, as shown in (2.17) below, in which n is the number of states in the system, p the number of observations, m the highest differentiation order in consideration, and $\overset{(m-1)}{y}(t)$ is the (m-1)-th order time-derivative of y.

$$\mathcal{O} = \frac{d}{dx} \begin{bmatrix} y(t) \\ \dot{y}(t) \\ \vdots \\ \overset{(m-1)}{y}(t) \end{bmatrix} \in \mathbb{R}^{mp \times n} \tag{2.17}$$

If this matrix is invertible (and therefore has full rank), then the state $x(t)$ can be recovered from the set of observations $y(t)$ and its respective derivatives. If the observed dynamical system is linear (with

constant $\frac{df}{dx} = A$ and $\frac{dh}{dx} = C$), the observability matrix is simply defined as

$$\mathcal{O} = \begin{bmatrix} C \\ CA \\ \vdots \\ CA^{m-1} \end{bmatrix} \in \mathbb{R}^{mp \times n}, \tag{2.18}$$

being independent of time t or state vector x. For nonlinear systems, this matrix is calculated by differentiating the observation equations through Lie algebra. A Lie derivative of a function h by a function f is defined as

$$\mathcal{L}_f(h)(x) = \frac{\partial h(x)}{\partial x} f(x) \in \mathbb{R}^{p \times 1}. \tag{2.19}$$

The same Lie derivative of order k is defined as

$$\mathcal{L}_f^k(h)(x) = \frac{\partial \mathcal{L}_f^{k-1}(h)(x)}{\partial x} f(x) \in \mathbb{R}^{p \times 1}. \tag{2.20}$$

The observability matrix $\mathcal{O}$ of a nonlinear dynamic system such as the one described in (2.15a) and (2.15b) is therefore defined by these Lie derivatives [44]:

$$\mathcal{O} = \begin{bmatrix} \frac{\partial h(x)}{\partial x} \\ \vdots \\ \frac{\partial \mathcal{L}_f^{m-1}(h)(x)}{\partial x} \end{bmatrix} \in \mathbb{R}^{mp \times n}. \tag{2.21}$$

For the rank condition to be met, it is necessary that the highest differentiation order in consideration m be greater than n/p, otherwise the observability matrix will always be rank defficient. In some scenarios, the increasing order of the Lie derivatives leads to exponentially more complex and computation-heavy expressions, such that the observability matrix may be rendered impractical to calculate. An alternative approach is to obtain the observability matrix from the linearized and discretized version of the dynamic system in (2.15) [45]. Let us consider the discrete-time dynamic system

$$x(t_k) = \Phi_{k|k-1} x(t_{k-1}) \tag{2.22a}$$

$$y(t_k) = H_k x(t_k) \tag{2.22b}$$

where $t \in \{t_0, t_1, \ldots, t_k\}$, $\Phi_{i+j|i}$ is the state transition matrix from the set of states $x(t_i)$ to $x(t_{i+j})$ and $H_k = \frac{dh}{dx}(x(t_k))$. The discrete-time version of the observability matrix can be calculated as

$$\begin{bmatrix} y(t_0) \\ y(t_1) \\ \vdots \\ y(t_{m-1}) \end{bmatrix} = \mathcal{O}_d x(t_0) \Rightarrow \mathcal{O}_d = \begin{bmatrix} H_0 \\ H_1 \Phi_{1|0} \\ \vdots \\ H_{m-1} \Phi_{m-1|0} \end{bmatrix} \in \mathbb{R}^{mp \times n}. \tag{2.23}$$

If $\mathcal{O}_d$ from (2.23) above has rank n, that means that the initial condition $x(t_0)$ can be obtained from the observations $y(t_{0:m-1})$.

Observability Gramian

An alternative tool that can be used to evaluate local observability is the observability Gramian [46]. The linearized least squares observer solution to the nonlinear system in (2.15) is given as

$$\hat{x}_{ls}(0) = \underbrace{\left(\int_{t_0}^{T} \Phi_{t_0}^T(\tau) H^T H \Phi_{t_0}(\tau) d\tau\right)}_{W_0}^{-1} \int_0^T \Phi_{t_0}^T(\bar{t}) H^T(\tau) y(\bar{t}) d\bar{t} \tag{2.24}$$

where $H(\tau) = \dfrac{dh}{dx}(x(\tau))$ is the jacobian matrix of the observation equation with respect to the states at time τ and $\Phi_{t_0}(\tau)$ is the state transition matrix from $x(t_0)$ to $x(\tau)$ ($x(\tau) = \Phi_{t_0}(\tau)x(t_0)$) [47]. This problem can only be solved if W_0 within the equation is invertible. Sharing the same property with the observability matrix that enables it to evaluate the observability of an observed dynamic system, this formula is known as the local observability Gramian. For a continuous nonlinear system, the local observability Gramian can therefore be calculated as follows [44]:

$$W_0 = \int_0^T \Phi_{t_0}^T(\tau) H^T(\tau) H(\tau) \Phi_{t_0}(\tau) d\tau. \tag{2.25}$$

For a discrete-time nonlinear system such as the one in (2.22), the adapted formulation of the observability Gramian is the following:

$$W_0 = \sum_{i=0}^{k} \Phi_{i|0}^T H_i^T H_i \Phi_{i|0}. \tag{2.26}$$

Standard Fisher Information Matrix

Both the observability matrix and Gramian are used to evaluate the observability of a deterministic observed dynamic system. For dynamic systems with stochastic dynamic and/or observation models, the concept of observability is replaced with that of Fisher information.

Fisher information quantifies the amount of information that a set of random variables y contain about unknown parameters/states x. More precisely, it is the variance of the expected value of the observed information. This information can be described by the Fisher Information Matrix, which is equivalent to the inverse of the state/parameter covariance matrix. Akin to the observability Gramian, the Fisher Information Matrix is invertible when the entire set of states is observable.

In this study, we focus on the SFIM (Standard Fisher Information Matrix) pertaining to the following discrete-time nonlinear system of equations

$$x_k \triangleq x(t_k) = \phi(x(t_{k-1})) \tag{2.27}$$

$$y_k \triangleq y(x_k) = h(x_k) + \nu_k, \;\; \nu_k \sim \mathcal{N}(0, R_k) \tag{2.28}$$

where $t \in \{t_0, t_1, ..., t_k\}$ and $\mathcal{N}(0, R_k)$ is a centered gaussian white noise with covariance R_k. The SFIM for this system of equations is calculated as

$$\text{SFIM} = \sum_{i=0}^{k} \Phi_{i|0}^T H_i^T R_i^{-1} H_i \Phi_{i|0}, \tag{2.29}$$

in which $H_i = \dfrac{dh}{dx}(x_i)$, $\Phi_{i|0}$ is the state transition matrix from x_0 to x_i and R_i is the observation noise covariance matrix [48]. The purpose of the SFIM can be made more clear by looking at the solution of a discrete-time weighted nonlinear least squares observer for the system of (2.27) and (2.28)

$$\hat{x}_{wls}(t_0) = \hat{x}_0 + \left(\sum_{i=0}^{k} \Phi_{i|0}^T H_i^T R_i^{-1} H_i \Phi_{i|0} \right)^{-1} \left(\sum_{i=0}^{k} \Phi_{i|0}^T H_i^T R_i^{-1} (y_i - h(\hat{x}_i)) \right), \tag{2.30}$$

where $\hat{x}$ is the initial estimate for the set of states of the system respecting the dynamics described in (2.27) [8]. For this estimation method, the inverse of the SFIM describes the state covariance matrix of the weighted least-squares observer ($\text{SFIM}^{-1} = E\{(\hat{x}_{wls}(t_0) - \hat{x}_0)(\hat{x}_{wls}(t_0) - \hat{x}_0)^T\}$).

2.3.2 Observability metrics

Hermann-Krener's rank condition serves to determine whether a nonlinear system is locally observable or not. However, in order to perform an observability optimization study, it is necessary to find a metric that quantifies the degree of observability.

The following scalar measures of the observability gramian or SFIM have been used in the literature with various interpretations related to the uncertainty in the systems [48]:

- Determinant of the inverse matrix (or reciprocal of the matrix determinant);
- Trace of the inverse matrix;
- Negative trace of the matrix;
- Reciprocal of the matrix's minimum singular value (also known as *unobservability index* [44]);
- Reciprocal of the matrix's maximum eigenvalue;
- The condition number of the matrix.

In a previous spacecraft formation relative positioning observability study from Ou [45], the condition number of the discretised observability matrix shown in (2.23) was used. Due to the complex orbit propagation model chosen, *Ou* chose to use the discretised version of the observability matrix, rather than the analytical formulation with Lie algebra shown in (2.21).

As stated in [44], the local singular values of the system in (2.15) at $x(0)$ are equivalent to the square root of the eigenvalues of the observability gramian shown in (2.25). This comes as a result of the fact that, from equations (2.23) and (2.26), it is possible to calculate the OG as $W_0 = \mathcal{O}_d^T \mathcal{O}_d$. This article refers to the reciprocal of the square root of the smallest eigenvalue of the OG as the *local*

unobservability index and to the square root of the ratio of the largest to the smallest eigenvalue the *local estimation condition number*.

2.3.3 Relative state observability analysis

The concept of using relative positioning within a multi-satellite mission for autonomous navigation was first suggested by Markley [10]. In his paper, Markley demonstrated the full observability of a positioning system with two spacecraft in Keplerian orbits around the same body, and with relative position measurements (in the inertial frame) using the linearized observability matrix.

Let us consider a continuous nonlinear system such as the one in (2.15), with state vector $x = [r_0^T \ v_0^T \ r_{1/0}^T \ \delta v_{1/0}]^T$, where r_0 is the position vector of the chief spacecraft in the inertial central-body-centered frame, v_0 is the respective velocity vector in the same frame, $\delta r_{1/0}$ is the position vector of the deputy spacecraft with respect to the chief spacecraft in an inertial frame of reference, and $\delta v_{1/0}$ is the respective velocity vector in the same frame. The nonlinear system is therefore described by the following set of equations:

$$\begin{cases} \begin{bmatrix} \dot{r}_0 \\ \dot{v}_0 \\ \dot{\delta r}_{1/0} \\ \dot{\delta v}_{1/0} \end{bmatrix} = \begin{bmatrix} v_0 \\ -\mu \dfrac{r_0}{\|r_0\|^3} \\ \delta v_{1/0} \\ -\mu \left(\dfrac{r_0 + \delta r_{1/0}}{\|r_0 + \delta r_{1/0}\|^3} - \dfrac{r_0}{\|r_0\|^3} \right) \end{bmatrix} \\ y = \delta r_{1/0} \end{cases} \tag{2.31}$$

where μ is the constant gravitational parameter of the central body. The respective local observability matrix calculated through Lie algebra is defined as:

$$\mathcal{O} = \begin{bmatrix} 0 & 0 & I & 0 \\ 0 & 0 & 0 & I \\ G_1 - G_0 & 0 & G_1 & 0 \\ \dot{G}_1 - \dot{G}_0 & G_1 - G_0 & \dot{G}_1 & G_1 \end{bmatrix} \tag{2.32}$$

where

$$G_i = \frac{\mu}{\|r_i\|^3} \left(3\hat{r}_i \hat{r}_i^T - I \right) \tag{2.33a}$$

$$\dot{G}_i = \frac{3\mu}{\|r_i\|^4} \left[v_i \hat{r}_i^T + \hat{r}_i v_i^T - \left(\hat{r}_i^T v_i \right) \left(5\hat{r}_i \hat{r}_i^T - I \right) \right] \tag{2.33b}$$

$$\hat{r}_i = \frac{r_i}{\|r_i\|} \tag{2.33c}$$

and recalling that $r_1 = r_0 + \delta r_{1/0}$ and $v_1 = v_0 + \delta v_{1/0}$. From the shape of the observability matrix, we can deduce that it will have full rank as long as $G_1 - G_0$ has rank 3. The only scenario in which it does not is when $\|r_1\| = \|r_0\|$. Extending the number of differentiations done to the observation equations

beyond $m = 3$, Markley [10] reached the conclusion that this system will become unobservable if both spacecraft have the same altitude time histories, and are either coplanar or oriented so that they cross the line of intersection of the two orbital planes at the same instant.

Further studies have been done on the observability of this system. Psiaki considered the use of relative positioning for the estimation of a planet's gravity field coefficients along with autonomous navigation, demonstrating its feasibility [12].

Since relative positioning systems that do not depend on tracking systems estimate the relative position through separate measurements of the range and LOS vector, studies have also been done on the observability of a system with ranging-only [14] and LOS vector-only [15].

Ranging-only observability

Hill found that ranging measurements in the two-body problem could observe the shape, phase and relative orientation of the orbits of the two spacecraft, but not the absolute orientation with respect to the inertial frame of reference, due to the symmetry of the gravity field [14]. Under a more complete dynamic model that considers the asymmetries of the gravity field of the central body, the problem can become observable [14, 49]. Another way to render this system observable through ranging measurements is to consider three-body dynamics, in which one of the spacecraft is in the Lagrange points 1 or 2. This concept of navigation for the Earth-Moon system is known as LiAISON [50], and has been proposed as a method of autonomous navigation for vehicles on the far side of the lunar surface.

LOS-only observability

According to Yim's paper [15], relative LOS vector measurements with inertial attitude information allow for the system to be observable, even without J_2 perturbations from the Earth's oblateness effect on its gravity field. This system is only not observable when the two spacecraft are in the same equatorial orbiting plane. Increasing the complexity of the gravity field of the central body or the inclination of both orbits will also make the system more observable.

2.4 Case study - SunRISE mission

In this thesis, the *SunRISE* mission will be used as a template for the relative positioning autonomous method simulation and analysis. This section provides a brief introduction to the mission, its objectives, requirements and chosen orbital configuration, based on the information provided in [51].

The SunRISE mission, proposed by NASA's Jet Propulsion Laboratory, aims at studying the acceleration of solar energetic particles at Coronal Mass Ejections and their release into interplanetary space. SunRISE consists of a cluster of six spacecraft operating in loose formation as a space-based interferometer to form a synthetic aperture with a $5\,\mathrm{km}$ radius. The mission requirements for these scientific goals include:

1. 6-month baseline science operations;

2. Sun-pointed dipole antennas;
3. Operations above the Earth's ionosphere;
4. Minimum of 5 spacecraft;
5. Maximum spacecraft separation bigger than 10 km;
6. Smallest spacecraft separation lower than 1 km;
7. 17 ns relative timing uncertainties between spacecraft pairs, translating to maximum 3 m relative position accuracy.

Taking these requirements into consideration, the SunRISE mission was designed to be a spacecraft formation with 6 identical 6U CubeSat forming an observatory in a 25-hour circular orbit slightly above GEO. The formation is kept passively, with only biweekly statistical correction maneuvers to ensure the spacecraft separation requirement is respected and to avoid collisions.

The chief orbit of the formation, around which the spacecraft are positioned, is described in Table 2.1 through its keplerian elements.

Keplerian elements	**a (km)**	**e**	**i (rad)**	**ω (rad)**	**Ω (rad)**	**ν (rad)**
Chief Orbit	43399	0	0	0	0	0

Table 2.1: Initial Keplerian elements of the SunRISE formation's chief orbit.

The method for the orbital design of the formation around the chief orbit, described in [30], is replicated in Appendix B. Parameters are provided that allow for the replication of a valid orbital configuration for the mission. The resulting relative orbits of the 6 spacecraft around the chief orbit in the LI and LVLH frame are shown in Figures 2.6(a) and 2.6(b), respectively.

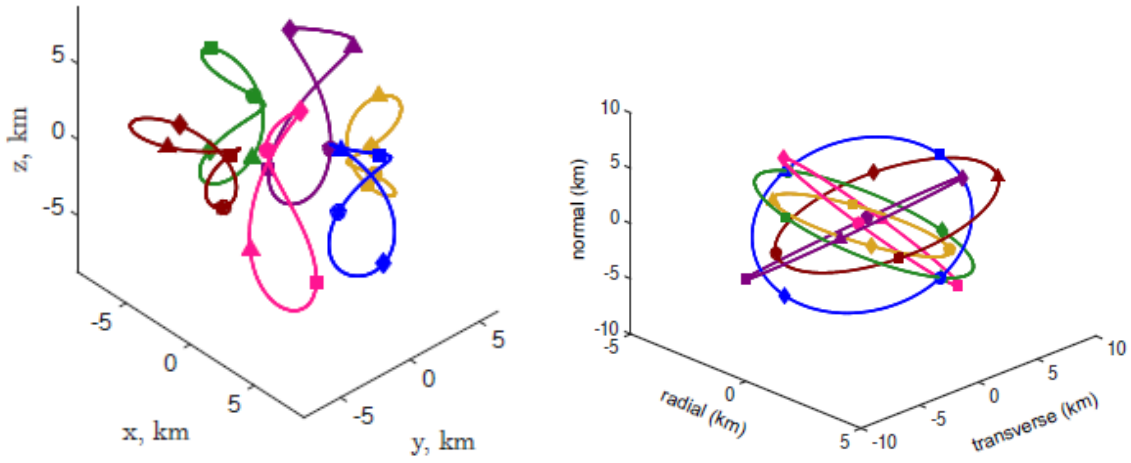

(a) Orbital configuration in the LI frame centered on the chief orbit.

(b) Orbital configuration in the LVLH frame centered on the chief orbit.

Figure 2.6: Example of a potential orbital configuration for the SunRISE flying formation [30].

2.5 Performance evaluation

Aside from the observability metrics defined in the previous section, performance metrics will also be necessary to evaluate the performance of the filtering algorithm in the different simulation configurations. Special focus will be given to the filter's accuracy upon convergence. Several options exist when evaluating the accuracy of a filtering algorithm within a multi-vehicle system [52]. Throughout this work, the root mean squared error (RMSE) will become the basic tool to construct these accuracy metrics.

Let us consider our set of estimated states $\hat{x}(t)$, which contains the subsets with the estimated positions of each spacecraft $\hat{r}_i(t)$, where i is the spacecraft's index. The position error at time t_k is given by

$$e_i(t_k) = \|\hat{r}_i(t_k) - r_i(t_k)\| \tag{2.34}$$

where $r_i(t)$ describes the true position of spacecraft i at time t. Similarly, the relative position error of deputy spacecraft i with respect to the chief spacecraft 1 is described as

$$e_{i/1}(t_k) = \left\|\delta\hat{r}_{i/1}(t_k) - \delta r_{i/1}(t_k)\right\| = \|\hat{r}_i(t_k) - \hat{r}_1(t_k) - [r_i(t_k) - r_1(t_k)]\|. \tag{2.35}$$

The RMSE is calculated as

$$e_{i,\mathrm{rms}} = \sqrt{\frac{1}{N+1-n}\sum_{k=n}^{N} e_i(t_k)^2} \tag{2.36}$$

where t_k is the first time sample in consideration (chosen so as to not account for the initial positioning error convergence period). This formula applies to both absolute and relative positioning errors. For a Monte-Carlo simulation with M trials, the mean Monte-Carlo spacecraft's time-averaged RMSE is calculated as

$$\overline{e}_{i,\mathrm{rms}} = \frac{1}{M}\sum_{m=1}^{M} e^m_{i,\mathrm{rms}} \tag{2.37}$$

where $e^m_{i,\mathrm{rms}}$ is the ith-spacecraft's RMSE in Monte-Carlo trial m. Finally, it will be interesting to split the absolute and the relative positioning error into two metrics. Since the deputy spacecraft's position will be expressed with respect to the chief spacecraft, the average of their positioning error will provide the average relative positioning error. Therefore, considering that the formation has I elements, where index 1 pertains to the chief spacecraft's absolute position in the ECI frame, the average relative positioning error of the formation is expressed as

$$\overline{e}_{2:I/1,\mathrm{rms}} = \frac{1}{I-1}\sum_{i=2}^{I} \overline{e}_{i/1,\mathrm{rms}}. \tag{2.38}$$

These metrics will be used throughout this work to evaluate and compare (both in terms of relative and absolute positioning accuracy) the localization algorithms that will be described in detail in the next chapter.

Chapter 3

Localization methods

In this chapter we will discuss the localization methods designed to achieve the relative positioning requirements of the SunRISE mission. Firstly, we will discuss the solutions proposed in [30], starting with the chosen GNSS-based solution, and then move on to the alternative RF-based method that was insufficiently accurate to meet the mission requirements. Finally, a new proposal will be made, based on the latter method's sensing strategy, but with added absolute position estimation.

3.1 GNSS-based system

Although GNSS positioning is a well-established method for orbit determination in Earth-centered missions, the mission's position above the GNSS belt implies that signal availability will be more limited than it would be for typical LEO missions. This is a result of the GNSS signals being directed towards orbits below the belt, meaning that above this belt only signals transmitted from navigation satellites on the opposite side of the Earth can be captured, as demonstrated in Figure 3.1 [30].

Despite this setback, previous above-the-belt missions have managed to achieve good positioning accuracy. One remarkable example of such precedent was the *MMS* mission, which attained GNSS positioning at altitudes above 12 earth radii [7]. In [30], the proposed GNSS-based system for the SunRISE mission was predicted to be able to achieve an average root mean square (RMS) error for the six satellites of 1.08-m in 3D position and 3.5-ns for clock error. These predicted uncertainties meet the mission concept's requirements of maximum 3-m relative positioning accuracy and 17-ns for clock error.

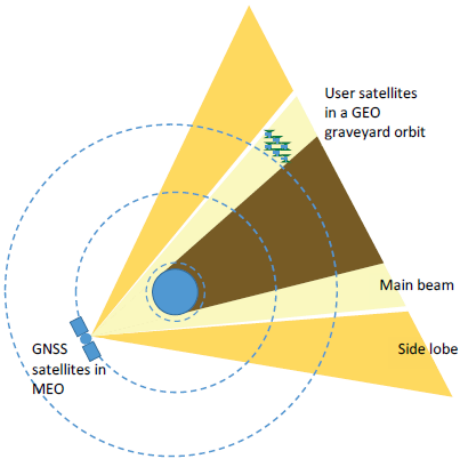

Figure 3.1: Representation of GNSS signal strength in a GEO graveyard orbit. The shaded area shows the zone where the signal is blocked by the Earth, and the lighter area shows the main beam zone available to the spacecraft above the GNSS-belt [30].

3.2 RF-based system

The alternative proposed method for relative navigation was based on relative range and bearing measurements among the formation spacecraft. In this scheme, each spacecraft will carry a ultra-high frequency (UHF) radio which can perform pseudo-range measurements between the formation spacecraft. Furthermore, each spacecraft will carry a star tracker, a camera that can measure the attitude of each spacecraft with respect to the celestial background. This star tracker can also be used to track a light-emitting diode (LED) equipped on the surface of each spacecraft in the formation. This allows the camera to measure the relative bearing (right ascension and declination) of a spacecraft with respect to another in an inertially aligned frame of reference [30].

3.2.1 Crosslink UHF schedule

Range measurements between two spacecraft in the formation can only be taken after their UHF radios lock on to each other. Similarly, the spacecraft also need to slew to point their cameras towards each other to obtain relative bearing measurements with respect to an inertially aligned frame of reference. This entire process takes approximately 9 minutes [30]. Once the radios are locked-on and the spacecraft have finished the slewing maneuver, new relative range and bearing measurements can be taken every second [30].

A measurement schedule is necessary to determine which spacecraft pairs should perform relative range and bearing measurements at a given time step. This schedule should take into account two main points. The first is that relative range and bearing measurements can be combined to obtain the relative position, the variable the navigation system is trying to estimate. If these measurements are taken asynchronously, the filter will require a dynamic model of the relative motion to estimate the relative states. For this reason, the navigation system will benefit from having synchronous range and

bearing measurements between two spacecraft. The second point to consider is that, for the filter to estimate the relative positions of the spacecraft in the formation with respect to each other in a balanced manner, the measurement schedule should proportionally include every possible pairwise combination of range and bearing measurements between different spacecraft. Such a schedule will inevitably lead to frequent periodic slewing maneuvers.

Based on these two points, [30] proposed the measurement schedule shown in Table 3.1, in which the spacecraft are refered to by the index attributed to them in Table B.3. This measurement schedule cycles every 50 minutes, which is the least amount of time required to go through every possible pairwise spacecraft combination. The table shows the time intervals during which the shown spacecraft pairs perform synchronous range and bearing measurements with each other, at a frequency of 1 Hz.

Time Interval, min	S/C Pairs
$[t_0 + 9 + 50k, t_0 + 10 + 50k]$	**1-2 3-4 5-6**
$[t_0 + 19 + 50k, t_0 + 20 + 50k]$	**1-3 2-5 4-6**
$[t_0 + 29 + 50k, t_0 + 30 + 50k]$	**1-4 2-6 3-5**
$[t_0 + 39 + 50k, t_0 + 40 + 50k]$	**1-5 2-4 3-6**
$[t_0 + 49 + 50k, t_0 + 50 + 50k]$	**1-6 2-3 4-5**

Table 3.1: Measurement schedule, where t_0 is the starting epoch and $k \in \mathbb{Z}^+$ [30]

The filtering technique described in [30] for this method is an EKF (Extended Kalman Filter) [53]. In the following section, we will describe the formulation of the EKF, and the associated prediction and observation model.

3.2.2 Extended Kalman Filter

A Kalman Filter is an estimation algorithm designed to minimize a quadratic function of the estimation error of a linear dynamic system, of which the measurement and dynamic model errors are treated as white noise. The EKF is an adaptation of the Kalman Filter for nonlinear dynamic systems, which, for systems with no dynamic input, can be generalized according to the following equations:

$$\dot{x}(t) = f(x(t), t, w) \tag{3.1}$$

$$y(t) = h(x(t), t, \nu) \tag{3.2}$$

where $y \in \mathcal{R}^m$ denotes the available observations on the system's states, $w \in \mathcal{R}^p$ represents process noise meant to describe the innacuracies in the filter's dynamic model and $\nu \in \mathcal{R}^m$ represents mea-

surement noise. These latter two are modelled as zero-mean white noise, such that $w \sim \mathcal{N}(0, Q)$ and $\nu \sim \mathcal{N}(0, R)$. The EKF acts sequentially on a set of observations y, filtering the dynamics and measurements through time. Henceforth, estimates will be denoted with the hat operator, and the index k will be used to differentiate time samples of the filter associated with a new state estimate.

The state estimate $\hat{x}$ at time t_{k+1} is calculated in 2 steps. In the first step, the nonlinear state propagation model is used to predict the current state estimate based on the previous state estimate at time t_k. This is called the prediction phase of the EKF, of which the resulting predicted states are the *a priori* states, and denoted by $\hat{x}_{k+1}^-$. In the update phase, the measurements y, being modelled after the states x according to (3.2), are used to correct the predicted states. The resulting *a posteriori* estimated states are denoted by $\hat{x}_{k+1}^+$.

Once initialized, the algorithm repeats the predict-update sequence for each time step k, where each stage requires the computation of a state vector and its respective covariance matrix. If an estimate is required from the filter at a time step with no available measurements, the filter can alternatively provide the *a priori* estimates propagated from the last update phase, up until a new set of observations arrives.

Initial conditions

In order to initiate the recursive algorithm, the EKF requires both the estimated states at the first epoch t_0 and their respective covariance matrix, $\hat{x}_0^+$ and P_0^+.

Prediction Phase

Based on the nonlinear system model from (3.1), the discrete-time state estimate dynamics must adhere to the state propagation equation

$$\hat{x}_{k+1}^- = \phi(\hat{x}_k^+, t_k, 0), \tag{3.3}$$

where $x_{k+1}^- = \phi(x_k^+, t_k, w_d)$ is the discrete-time nonlinear equivalent of the system in (3.1). Because the discrete-time process noise w_d from t_k to t_{k+1} is assumed to be centered and uncorrelated to the process noise in the previous time steps, its contribution can be ignored in (3.3).

The *a priori* state covariance matrix is propagated accordingly through

$$P_{k+1}^- = \Phi_{k|k-1} P_k^+ \Phi_{k|k-1}^T + Q_d, \tag{3.4}$$

where Φ_k is the jacobian matrix of $\phi(\cdot)$ with respect to the states x, and calculated using the previous *a posteriori* states, $\Phi_k = \dfrac{d\phi}{dx}(x_k^+, t_k, 0)$, P_k^+ is the previous *a posteriori* state covariance matrix and Q_d is the (discretized) process noise covariance matrix.

Update phase

During the update phase, the state estimate will be updated with the Kalman gain K_{k+1} and the measurements at time t_{k+1} according to

$$\hat{x}_{k+1}^{+} = \hat{x}_{k+1}^{-} + K_{k+1}(y_{k+1} - \hat{y}_{k+1}), \tag{3.5}$$

in which the estimated measurements $\hat{y}_{k+1}$ are calculated as $h(\hat{x}_{k+1}^{-}, t_{k+1}, 0)$. The Kalman gain K_{k+1} is calculated as

$$K_{k+1} = P_{k+1}^{-} H_{k+1}^{T} (H_{k+1} P_{k+1}^{-} H_{k+1}^{T} + R_k)^{-1}, \tag{3.6}$$

where $H_{k+1} = \dfrac{dh}{dx}(\hat{x}_{k+1}^{-}, t_{k+1}, 0)$ is the (discretized) observation matrix, and R_k is the measurement noise covariance matrix. Finally, the state covariance matrix is updated as

$$P_{k+1}^{+} = (I - K_{k+1} H_{k+1}) P_{k+1}^{-}. \tag{3.7}$$

Prediction Model

The EKF proposed in [30] was designed based on the conservative assumption that no information is available on the formation's initial absolute position. Assuming there is no information on the spacecraft's absolute position, orbital mechanics were not used to predict the spacecraft's motion. Instead, the filter follows a PVA (Position-Velocity-Acceleration) prediction model, meaning that its state vector accounts for the position, velocity and acceleration of each of the elements within the formation [54]. The PVA model of motion prediction takes the acceleration as a Brownian motion, as depicted in Figure 3.2.

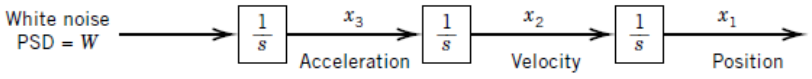

Figure 3.2: PVA model state space [55].

Let us consider $\delta r_{j/1}$ the position vector of spacecraft $j \in [2, ..., 6]$ with respect to spacecraft 1 in the LI frame centered at the latter. Its corresponding velocity vector in the same frame of reference is $\delta v_{j/1}$, and its acceleration vector is $\delta a_{j/1}$. In matricial form, the continuous time propagation of these states in the PVA model is

$$\begin{aligned} \dot{x}_j &= A_j x_j + G_j w_j \Leftrightarrow \\ \Leftrightarrow \begin{bmatrix} \dot{\delta r}_{j/1} \\ \dot{\delta v}_{j/1} \\ \dot{\delta a}_{j/1} \end{bmatrix} &= \begin{bmatrix} 0_{3\times3} & I_{3\times3} & 0_{3\times3} \\ 0_{3\times3} & 0_{3\times3} & I_{3\times3} \\ 0_{3\times3} & 0_{3\times3} & 0_{3\times3} \end{bmatrix} \begin{bmatrix} \delta r_{j/1} \\ \delta v_{j/1} \\ \delta a_{j/1} \end{bmatrix} + \begin{bmatrix} 0_{3\times3} \\ 0_{3\times3} \\ I_{3\times3} \end{bmatrix} \begin{bmatrix} w_{j_1} \\ w_{j_2} \\ w_{j_3} \end{bmatrix} \end{aligned} \tag{3.8}$$

where w_j is a centered Gaussian white noise process with covariance

$$E\{w_j(t) w_j^{T}(\tau)\} = Q_j \delta(t - \tau) = q_j I_{3\times3} \delta(t - \tau), \tag{3.9}$$

where, in [30], $q_j = (1\text{e}{-07})^2(\text{m/s}^{3.5})^2 \forall j \in \{2, \ldots, 6\}$. The full state vector x for the formation is a direct sum of the individual propagation system of each relative spacecraft motion state vector x_j for $j \in \{2, ..., 6\}$. The complete full state dynamic model is therefore

$$\dot{x} = Ax + Gw, \tag{3.10}$$

where $A = \text{diag}(A_2, \ldots, A_6)$, $G = \text{diag}(G_2, \ldots, G_6)$, $x = \{x_j\}$ and w is the concatenation of the white noise processes w_j, akin to that of the full state vector, with covariance matrix $Q = \text{diag}(Q_2, \ldots, Q_6)$.

The discrete-time propagation of the estimated state can be calculated as

$$\hat{x}(t_{k+1}) = \Phi_{k+1|k}\hat{x}(t_k), \tag{3.11}$$

where the STM (State Transition Matrix) $\Phi_{k+1|k}$ for a time-invariant linear system is calculated as

$$\Phi_{k+1|k} \triangleq \Phi_k(t_{k+1}) = e^{A(t_{k+1}-t_k)} \tag{3.12}$$

and then used to update the state covariance matrix according to (3.4). In that same equation, the discretised process noise covariance matrix is calculated as

$$Q_d(t_{k+1}) = \int_{t_k}^{t_{k+1}} \Phi_k(t) G Q G^T \Phi_k(t)^T dt. \tag{3.13}$$

which has an exact closed-form solution [30].

Observation Model

According to the measurement schedule in Table 3.1, measurements will be made between any pair of two spacecraft indexed j and n. The range and bearing measurements within a pair describe the relative position vector in the inertial frame from one spacecraft to the other, $\delta r_{j/n} = [\delta r_{x,j/n}\ \delta r_{y,j/n}\ \delta r_{z,j/n}]^T$. Relative positions between a pair of which the chief spacecraft (indexed 1) is not a part of can be decomposed into relative position vectors that belong to the state vector x as

$$\delta r_{j/n}(t) = \delta r_{j/1}(t) - \delta r_{n/1}(t), \forall j \neq n \in \{2, ..., 6\}. \tag{3.14}$$

Range measurements between spacecraft j and n are expressed as

$$\rho_{j/n}(t) = \left\|\delta r_{j/n}(t)\right\| + \nu_\rho(t), \tag{3.15}$$

where $\nu_\rho(t)$ is a Gaussian white noise process with covariance

$$E\{\nu_\rho(t)\nu_\rho(\tau)\} = (1/3)^2\delta(t-\tau)\text{m}^2, \tag{3.16}$$

Bearing measurements of spacecraft j in the inertial frame centered at spacecraft n are divided into

right ascension ψ and declination θ angles. These two are expressed as

$$\begin{aligned}\psi_{j/n}(t) &= \arctan 2(\delta r_{y,j/n}(t), \delta r_{x,j/n}(t)) + \nu_\psi(t) \\ \theta_{j/n}(t) &= \arctan\left(\frac{\delta r_{z,j/n}(t)}{\sqrt{\delta r^2_{y,j/n}(t) + \delta r^2_{x,j/n}(t)}}\right) + \nu_\theta(t)\end{aligned} \tag{3.17}$$

where ν_ψ and ν_θ are independent Gaussian white noise processes with covariance

$$E\{\nu_\psi(t)\nu_\psi(\tau)\} = E\{\nu_\theta(t)\nu_\theta(\tau)\} = (35)^2\delta(t-\tau)\text{arcsec}^2. \tag{3.18}$$

The variance of the ranging, right ascension and declination are incorporated into the diagonal entries of the measurement noise covariance matrix R.

Finally, for the state and state covariance update step, the observation matrix $H_k = \dfrac{dh}{dx}(\hat{x}_{k|k-1})$ will be necessary. The only non-null entries of the Jacobian matrix rows pertaining to the measurements between spacecraft j and l are their partial derivatives with respect to the relative position states from the respective spacecraft, $\delta r_{j/1}$ and $\delta r_{l/1}$, which are the following:

$$\frac{d\rho_{j/n}}{d\delta r_{j/1}} = -\frac{d\rho_{j/n}}{d\delta r_{n/1}} = \begin{bmatrix}\dfrac{\delta r_{x,j/n}}{\|\delta r_{j/n}\|} & \dfrac{\delta r_{y,j/n}}{\|\delta r_{j/n}\|} & \dfrac{\delta r_{z,j/n}}{\|\delta r_{j/n}\|}\end{bmatrix} \tag{3.19}$$

$$\frac{d\psi_{j/n}}{d\delta r_{j/1}} = -\frac{d\psi_{j/n}}{d\delta r_{n/1}} = \begin{bmatrix}\dfrac{-\delta r_{y,j/n}}{\sqrt{\delta r^2_{x,j/n} + \delta r^2_{y,j/n}}} & \dfrac{\delta r_{x,j/n}}{\sqrt{\delta r^2_{x,j/n} + \delta r^2_{y,j/n}}} & 0\end{bmatrix} \tag{3.20}$$

$$\frac{d\theta_{j/n}}{d\delta r_{j/1}} = -\frac{d\theta_{j/n}}{d\delta r_{n/1}} = \begin{bmatrix}-\delta r_{x,j/n}\delta r_{z,j/n} & -\delta r_{y,j/n}\delta r_{z,j/n} & \delta r^2_{x,j/n} + \delta r^2_{y,j/n}\end{bmatrix}\left(\sqrt{\delta r^2_{x,j/n} + \delta r^2_{y,j/n}}\|\delta r_{j/n}\|^2\right)^{-1} \tag{3.21}$$

This filter runs at a fixed time step of 1 s. In between measurement sets, *a priori* state estimates are used, propagated from the last *a posteriori* measurement available. Once a new set of measurements arrives, the filter resumes its prediction-update cycle.

3.3 Proposed RF-based method

The filter described in the previous section was designed assuming that no information would be available on the spacecraft's initial absolute position. However, in [30] it is stated that this is a worst case scenario assumption, since the results are meant to provide an upper bound on the predicted navigation error of the system. In reality, some information is expected to be available on the spacecraft's absolute position [30].

In this section an improvement will be proposed to the EKF in [30] and described in the previous section, now based on the assumption that there is information on the initial absolute position of the spacecraft. The improvements affect only the state vector and prediction model, which will be described next.

Modified state vector

The previously proposed state vector incorporated the position, velocity, and acceleration vectors in an inertial frame centered at an arbitrary chief spacecraft (chosen to be the spacecraft indexed 1 in Table B.3). This led to 3 sets of 3 states for each spacecraft's relative state with respect to the chief spacecraft, therefore a full state vector comprising $3 \times 3 \times 5$ states. We now propose to remove the relative acceleration vector states for each of the spacecraft, and to add the absolute position and velocity vectors of the chief spacecraft 1 in the ECI frame to the state vector, leading to a state vector composed of $2 \times 3 \times 6$ states. This new state vector containts all the necessary degrees of freedom to describe and predict the Keplerian motion for each of the formation's spacecraft.

Modified propagation model

By including the absolute position into the state vector, we can now incorporate the Keplerian dynamic model into the EKF. The propagation of the absolute position is done with the following set of equations:

$$\begin{cases} \dot{r}_1 &= v_1 \\ \dot{v}_1 &= -\mu_\oplus \dfrac{r_1}{\|r_1\|^3} + w_1 \end{cases} \tag{3.22}$$

The relative states of spacecraft j with respect to chief spacecraft 1 in the LI frame, in turn, are propagated according to the following set of equations:

$$\begin{cases} \dot{\delta r}_{j/1} &= \delta v_{j/1} \\ \dot{\delta v}_{j/1} &= -\mu_\oplus \left(\dfrac{r_1 + \delta r_{j/1}}{\|r_1 + \delta r_{j/1}\|^3} - \dfrac{r_1}{\|r_1\|^3} \right) + w_j \end{cases} \tag{3.23}$$

This model is based on the one described in Eqs. (2.31). Like in the previous model, w_j is a centered Gaussian white noise process with covariance described by the model in Eq. (3.9). The default value of q_1 was set to $(1\mathrm{e}{-06})^2(\mathrm{km/s}^{2.5})^2$, while the remaining relative values $q_j, \forall j \in \{2, \ldots, 6\}$ were set to $(1\mathrm{e}{-09})^2(\mathrm{km/s}^{2.5})^2$. The full process covariance matrix Q is constructed similarly to the relative-only filter, with the direct sum of all Q_j.

As described in [53], because this is a discrete-time variant of the EKF, these continuous-time equations need to be discretized. *MATLAB*'s *ODE45* was chosen, with the default relative and absolute tolerance of $1\mathrm{e}{-3}$ and $1\mathrm{e}{-6}$, respectively. The integration is performed from the previous iteration to the next with an intermediate propagation time step. The STM (State Transition Matrix) is also numerically computed through this integration method and used for the term $\Phi_{k|k-1}$ in the EKF equations. Finally, the discretised process noise covariance matrix Q_d is obtained through Eq. (3.13). Because the prediction model is not linear, the Q_d matrix does not have a closed-form solution. The integral in Eq. (3.13) can instead be solved through quadrature as an approximation [56]:

$$Q_d(t_{k+N_q}) \simeq \sum_{i=1}^{N_q} \Phi_{k+i|k} G Q G^T \Phi_{k+i|k}^T (t_{k+i} - t_{k+i-1}). \tag{3.24}$$

Because this filter also runs at a fixed time step of $1\,\mathrm{s}$, the number of quadrature points N_q used to approximate the integral will be equal to the number of new *a priori* estimates since the last measurement (1 within measurement sets, 9×60 in between sets). It is important to note that some sources such as [8] show Q_d in Eq. (3.13) being calculated with the state transition matrix from the time-like variable being integrated t to the next time step t_{k+1}, instead of from t_k to t as described in [56] and [53]. While in the original RF-based system with linear dynamics this difference does not change the resulting Q_d, with nonlinear dynamics that may not be the case. In this thesis, the latter was used.

3.4 Filtering algorithm comparison

In this section, we show the results of Monte-Carlo simulations meant to compare the two configurations of the EKF and their performance in terms of accuracy.

3.4.1 Simulation setup

In order to test the feasibility of the method, the trajectory generation approach in [30] consists only of a two-body dynamic model with an added constant acceleration in a fixed arbitrary direction representing non-keplerian perturbations. Since the study focuses exclusively on relative positioning and does not account for orbit dynamics in its filter prediction step, the simulation period can be reduced to a portion of an orbital period. For that reason, no complex orbit dynamics propagation is necessary.

As we have mentioned before, however, in this study we intend to propose an improved filter that includes the estimation of the absolute position. For this reason, the decision was made to test the new filtering technique with a simulation period comprising one orbital period, and with as accurate a trajectory as possible. The simulation is therefore run with the trajectory generated as described in Appendix C, and compared with the results from the article.

The simulation is run with a fixed time step of $1\,\mathrm{s}$. As already mentioned, the *a priori* state estimates will be used instead of the *a posteriori* for the time steps without new measurements.

Filter initialization

In order to test the filters, it will be necessary to provide them with the initial state and respective covariance. In [30], an error of $100\,\mathrm{m}$ and $1\,\mathrm{cm/s}$ in a random direction was given to the initial relative position vector state estimates $\hat{\delta r}_{j/1}(t_0)$ and relative velocity vector state estimates $\hat{\delta v}_{j/1}(t_0)$, respectively, while the initial accelerations are assumed to be zero. The corresponding diagonal entries of the initial state covariance matrix are the squared value of that same initial error ($0.01\,\mathrm{km}^2$ for position entries and $1 \times 10^{-10}\,(\mathrm{km/s})^2$ for velocity entries), with the exception of acceleration entries, which are set at $1 \times 10^{-14}\,(\mathrm{km/s^2})^2$.

For the filter with the included absolute position states, it is important to test how sensitive the filter will be to initial errors in the absolute states. For this reason, the filter will be tested for initial errors in absolute position of $100\,\mathrm{m}$, $10\,\mathrm{km}$, $1000\,\mathrm{km}$ and $10\,000\,\mathrm{km}$, with an equally adjusted initial state covariance matrix. The relative states will be initialized in the same manner as the original filter.

3.4.2 Results

The true trajectories of the formation spacecraft in the LI frame centered at the chief spacecraft are shown in Figure 3.3(a), while the absolute state of the chief spacecraft is shown in Figure 3.3(b). These trajectories are common to the results in this section.

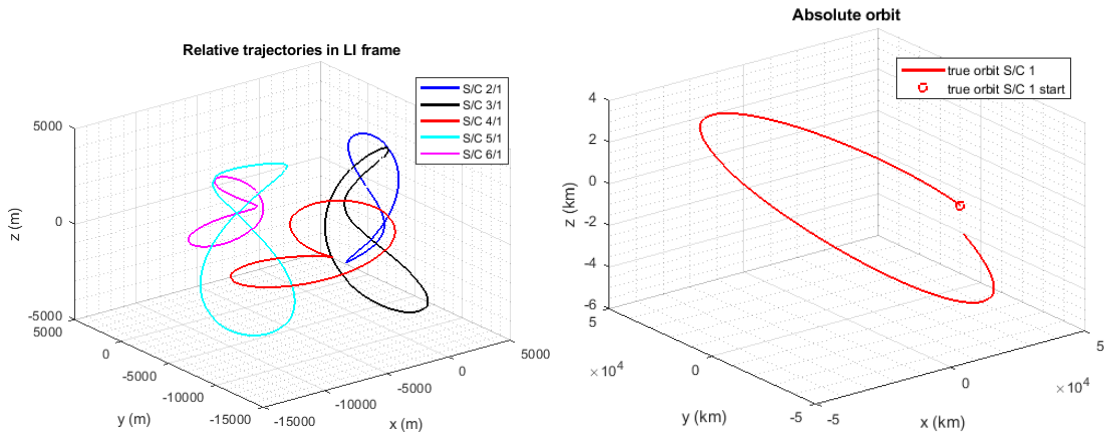

(a) Trajectories of the formation spacecraft in the LI frame with respect to the chief spacecraft.

(b) Trajectory of the chief spacecraft in the ECI frame.

Figure 3.3: True position state trajectories.

We will now evaluate the performance of the original relative-only filter in the new simulation setup, followed by an evaluation of the reconfigured EKF's performance, and then a comparison of the obtained results with those shown in [30].

Relative-only EKF

A total of $M = 40$ Monte-Carlo simulations were run with the Relative-only PVA filter. The plot of the evolution of the relative position error of each deputy spacecraft with respect to the chief spacecraft for an arbitrary Monte-Carlo simulation run is shown in Figure 3.5(a). The filter shows convergence from the initial $100m$ relative position error towards a base value at the meter-level accuracy. The filter converges relatively quickly with respect to the simulation period ($\approx 100\,\text{min}$). The Monte-Carlo averaged RMSE values of the positioning error are shown below in Table 3.2, where they can be compared with the rest of the results.

EKF with absolute states

Considering the initial absolute position error of the chief spacecraft to be $100\,\text{m}$, the same number of Monte-Carlo simulations were run with the newly proposed filter as with the original PVA filter in the new simulation environment. In order to verify whether relative positioning does in fact provide information on the absolute position of the formation, the evolution of the filter's estimated absolute position error of the chief spacecraft is compared to the drift of that same error using only the filter's prediction model. In this work, prediction model error designates the error that is observed when the states are propagated

from the initial set of states through the filter's Keplerian prediction model and compared to the true trajectory's more complex model. This plot is shown in Figure 3.4(a), along with a plot of the respective trajectories in Figure 3.4(b) for an arbitrary Monte-Carlo simulation run. The numerical integration of the Keplerian dynamics for the prediction model error plots is done using *MATLAB*'s *ODE45* with relative and absolute tolerance values set at $1\mathrm{e}{-14}$ and $1\mathrm{e}{-20}$, respectively, so as to present more accurately the true trajectory's drift from the Keplerian model's trajectory.

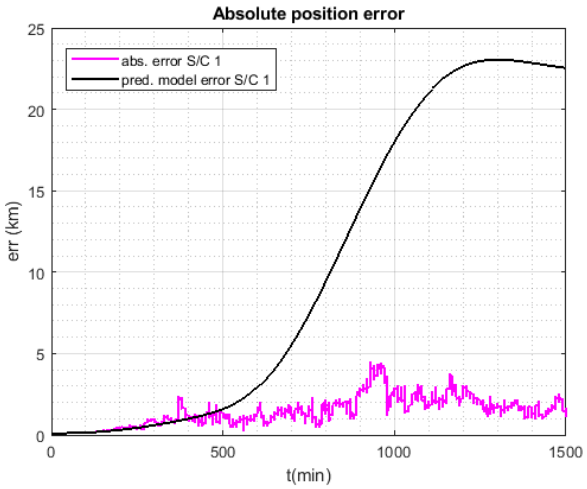

(a) Chief spacecraft absolute position error of the new EKF and Keplerian prediction model.

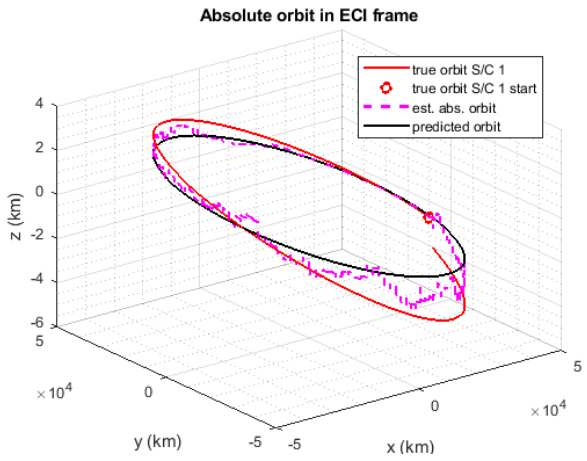

(b) Chief spacecraft true, estimated and predicted absolute trajectory.

Figure 3.4: Evolution of the absolute position and respective error with 100m initial absolute position error of the newly proposed filter.

Figure 3.4 shows that the relative position measurements correct the absolute position prediction model, as the EKF achieves greater absolute positioning accuracy than the prediction model alone. The absolute positioning error of the filter is in the order of a few kilometers. Focus will now be given to the relative positioning error of the deputy spacecraft with respect to the chief spacecraft shown in Figure 3.5(b).

The relative positioning estimated states also show convergence towards their true counterparts. These results, however, are based on the assumption that the initial absolute position is known with 100 meter precision. It is necessary to evaluate whether this method will still converge if the initial absolute error is larger. For that reason, Monte-Carlo simulations were also run ($M = 40$) with $10\,\mathrm{km}$, $1000\,\mathrm{km}$ and $10\,000\,\mathrm{km}$ initial absolute position error (with the initial state covariance matrix adjusted accordingly) to test the filter's robustness to poor initial conditions. The evolution of the absolute position error of the chief spacecraft, as well as the mean relative position error for all deputy spacecraft with each of these initial absolute position errors from arbitrarily chosen Monte-Carlo runs is shown in Figure 3.6.

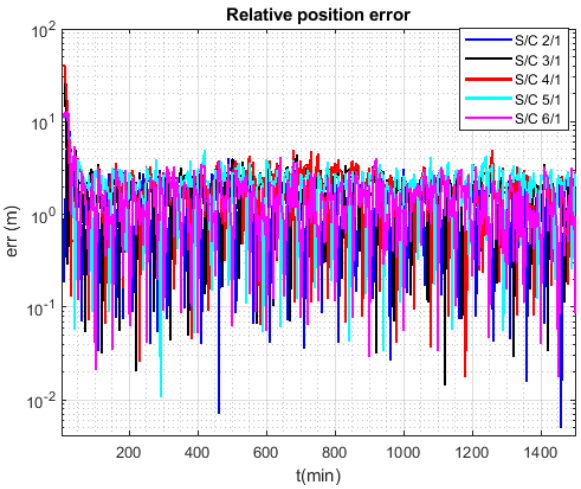

(a) Relative position error of formation spacecraft with respect to the chief spacecraft of the PVA EKF.

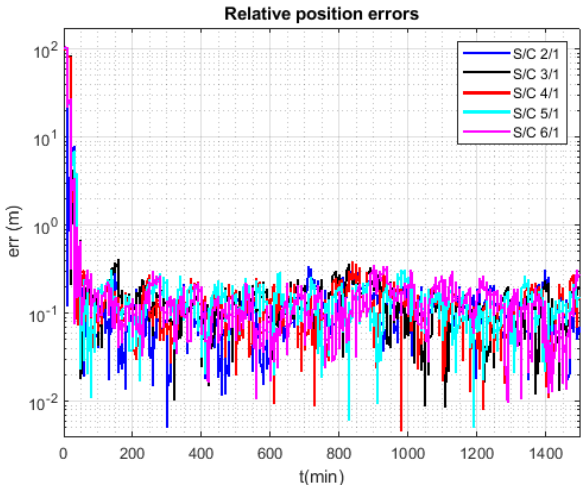

(b) Relative position error of formation spacecraft with respect to the chief spacecraft of the new EKF with orbital dynamics.

Figure 3.5: Comparison of the relative position error of formation spacecraft with respect to the chief spacecraft of the PVA EKF and the proposed EKF.

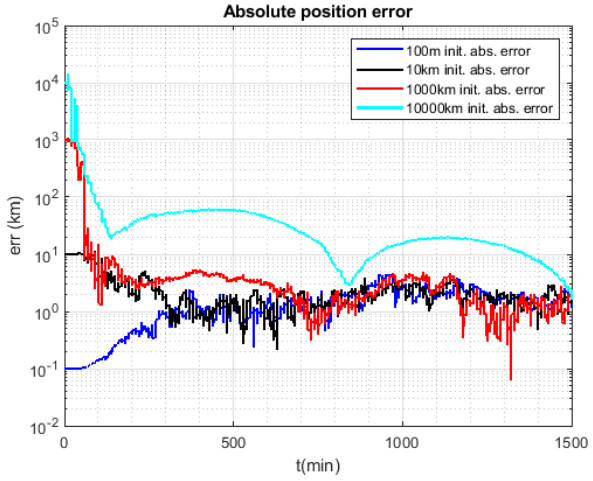

(a) Chief spacecraft absolute position error.

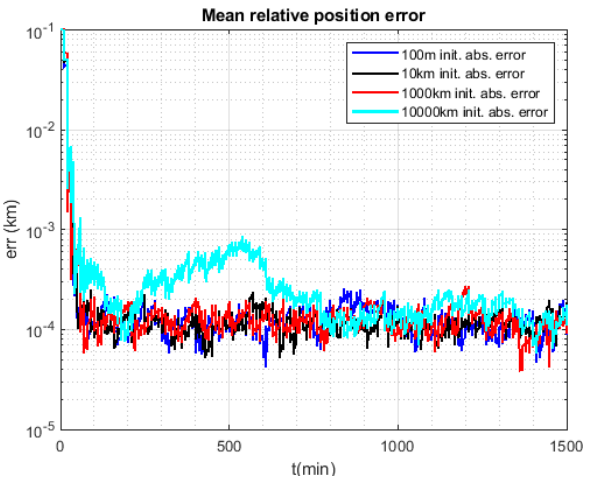

(b) Deputy spacecraft mean relative position error.

Figure 3.6: Evolution of the absolute and mean relative position errors with varying initial chief spacecraft absolute position error.

The results show that an initial absolute position error up to $1000\,\mathrm{km}$ will not cause the filter to diverge. With an initial error of $10\,000\,\mathrm{km}$, however, the filter's convergence speed is such that it does not entirely reach the same level of error as the remaining configurations within the simulation's period of one orbit. Only in this last most unfavourable scenario is the relative positioning performance visibly affected by this slower convergence. For the configurations with $1000\,\mathrm{km}$ initial absolute position error or lower, the relative positioning error does not seem to converge much slower than the original scenario with $100\,\mathrm{m}$ initial error, showing an average convergence time of $\approx 200\,\mathrm{min}$, while the absolute position converges in $\approx 300\,\mathrm{min}$. The resulting relative and absolute positioning converged accuracy is similar as well, for which the Monte-Carlo averaged RMSE values are shown in Table 3.2.

Results comparison

In the Table 3.2 below, the Monte-Carlo averaged RMS error values are shown for the two filters and respective configurations discussed above. These values only take into account the simulation period after which the filters have converged, considered to start at the $200\,\mathrm{min}$ for both, regardless of initial position error. Figure 3.7 shows these same values for the chief spacecraft's absolute positioning error ($\overline{e}_{\mathbf{1,rms}}$) and the deputy spacecraft's average relative positioning error ($\overline{e}_{\mathbf{2:6/1,rms}}$), with the respective maximum and minimum RMS error values obtained in the Monte Carlo runs.

RMS error	**Init. abs. error**	**Absolute Position Error (km)**	**Relative position error (m)**					
Filter		$\overline{e}_{1,\mathrm{rms}}$	$\overline{e}_{2/1,\mathrm{rms}}$	$\overline{e}_{3/1,\mathrm{rms}}$	$\overline{e}_{4/1,\mathrm{rms}}$	$\overline{e}_{5/1,\mathrm{rms}}$	$\overline{e}_{6/1,\mathrm{rms}}$	$\overline{e}_{2:6/1,\mathrm{rms}}$
Rel-only (results in [30])	-	-	2.8	4.1	4.1	4.2	2.8	3.6
Rel-only (new simulation)	-	-	2.8	4.1	4.2	4.2	2.6	3.6
Added abs. states	100 m	1.73	0.12	0.13	0.15	0.14	0.13	0.13
	10 km	2.06	0.12	0.13	0.15	0.14	0.13	0.13
	1000 km	2.76	0.12	0.13	0.15	0.14	0.13	0.13
	10 000 km	60.56	0.37	0.54	0.81	0.65	0.37	0.55

Table 3.2: Comparison of RMS Error values between the two EKF comparisons in different conditions.

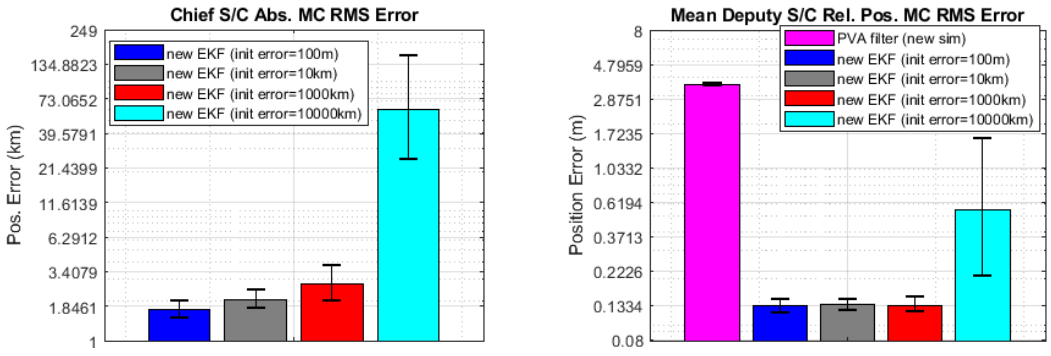

(a) Chief spacecraft absolute position Monte-Carlo averaged RMS error.

(b) Formation's deputy spacecraft mean relative position Monte-Carlo averaged RMS error.

Figure 3.7: Monte-Carlo averaged RMS error results for the absolute and relative position errors shown in Table 3.2, with upper and lower error bounds.

The results of the relative-only filter in this new simulation environment are nearly identical to those obtained in [30], showing that the filter performs similarly in both simulation environments. The addition of the absolute states and keplerian dynamics to the algorithm significantly improves its relative accuracy (by a factor of ~ 30).

The original filter was designed as a means to estimate the upper bound on the relative position error by assuming the worst case scenario that no information is available on the formation's initial position, so this result was expected. However, as stated in [30], some information is expected to be available on the initial states of the formation.

The variation in initial absolute position error, meant to test the new filter's robustness to poor initial absolute position knowledge showed generally positive results. The new filter is capable of converging

within the degrees of innacuracy considered (up to $10\,000\,\mathrm{km}$), although its convergence period extended beyond one orbital period for the worst case considered. However, the filter's robustness to a disparity between the initial "guess" in positioning error (expressed by the entries in the initial state covariance matrix) and the real initial positioning error was not tested.

The proposed modifications to the RF-based navigation solution seem to improve the overall performance of the system, not only increasing the relative positioning accuracy, but also allowing the formation to autonomously determine its absolute position. This proposed relative positioning method also presents the advantage of not being dependent on GNSS or ground station signals, therefore being apt for deep space missions requiring autonomous and real-time navigation. However, the absolute positioning accuracy of this method is considerably worse than the preferred GNSS-based solution for the SunRISE mission concept (by a factor of ~ 1000).

In order to explore to its full potential the absolute positioning performance of the proposed filter, the next chapter conducts an optimization study in which a new spacecraft is added to the formation, so that its orbital configuration maximizes the system's absolute and relative positioning accuracy. Secondly, a study will also be done on the possibility of removing the relative bearing sensors while maintaining full observability.

Chapter 4

Observability Analysis

In the previous chapter, we presented the GNSS-based and RF-based navigation solutions that were considered for the SunRISE mission, proposed a modification on the RF-based filtering algorithm to incorporate absolute position estimation into the solution, and compared their performances. Although the modified RF-based solution achieved more precise relative positioning accuracy, its absolute positioning performance is considerably worse than the GNSS-based solution (by a factor of around 1000).

As suggested in the first study that proposed the concept of autonomous navigation through the observation of the time history of the relative position of spacecraft in an inertial frame [10], the observability of the system is heavily dependent on the orbits of the spacecraft performing the measurements. In order to further explore the potential of this method, this chapter will firstly focus on adding a new spacecraft to the formation, such that its orbital configuration optimizes the navigation system's performance. Effectively, this may be seen as deploying a single-satellite auxiliary "constellation" to enhance absolute localization.

Secondly, and leveraging the presence of the optimized new spacecraft, a study will be made on whether the new system can remain observable when the relative bearing sensors from the original formation are removed.

4.1 Observability Optimization

This section describes the optimization problem in question. The optimization problem at hand was further split into several ones, with variations in the objective function, measurement system and conditions. The optimization results will also be presented and discussed.

4.1.1 Problem Description

As stated above, the objective of this study is to find the optimal orbital configuration of a new spacecraft in the *SunRISE* mission that maximizes the formation's navigation accuracy, both in terms of absolute and relative positioning.

Knowing that a mathematical constrained optimization problem can be defined as [57]:

$$\begin{aligned} \underset{x\in\mathcal{D}}{\text{minimize}} \quad & f(x) \\ \text{subject to} \quad & f_i(x) \leq 0,\ i \in \{1, ..., m\} \\ & h_j(x) = 0,\ j \in \{1, ..., p\} \end{aligned}$$

where:

$$\begin{aligned} x &= \text{set of variables to be optimized} \\ f(x) &= \text{Objective/Cost function} \\ f_i(x) &= \text{Inequality constraint} \\ h_j(x) &= \text{Equality constraint} \end{aligned}$$

The solution to this problem is denoted as $x_{opt} = \underset{x\in\mathcal{D}}{\arg\min} f(x)$. For this study, the set of variables to be optimized will define the initial classical orbital elements (or a subset of them) of the new spacecraft, which in its totality is described as $x = \{a_{new}, e_{new}, i_{new}, \Omega_{new}, \omega_{new}, \nu_{new}\}$.

Different methods were considered to assess the observability of the satellite system. In the following section, various choices for the objective function will be discussed.

4.1.2 Objective function

In Section 2.3, an overview was made of the tools and metrics that can be used to evaluate the observability of a nonlinear dynamic system, with a given set of available observations. This Section describes the tools and metrics chosen for this study, as well as the associated dynamic and observation systems and their respective approximations.

Dynamic system approximations

Because of the complexity of the dynamic system in question, composed of 7×6 states in total propagated for one orbital period, methods were required to reduce the computational load associated with the objective function. For this reason, the dynamics of the system will be restricted to the two-body problem in every formulation. The initial set of states will therefore be propagated through the Keplerian model in order to compute their corresponding trajectory and STMs (State Transition Matrices), which will be necessary for calculating the objective functions. The numerical integration is performed using *MATLAB*'s *ODE45* with relative and absolute tolerance of $1\mathrm{e}{-03}$ and $1\mathrm{e}{-06}$ respectively.

Previous optimization studies on this method of autonomous navigation generally lead to the belief that greater differences in gravitational acceleration intensity between spacecraft lead to better absolute position observability [11, 58]. From these previous results, it can be foreseen that the results that will be obtained in this study will lead to an auxiliary orbit with a much greater distance to the formation than the intersatellite distance within the formation. From this assumption, the decision was made to reduce the

formation to its chief virtual orbit (the parameters of which are described in Table 2.1) for the purposes of (simplified) observability analysis. The approximated system is therefore composed exclusively of the chief and new spacecraft.

Changes were also made to the sampling schedule. Rather than performing one sample per second for a minute every 10 minutes, leading to an average sampling period of $10\,\mathrm{s}$, a sampling period was chosen such that 1000 samples are taken during one orbital period of the chief orbit. Since the chief orbit has a period of 25 hours, the sampling period considered for the cost function is around $90\,\mathrm{s}$, significantly reducing its computation time.

Objective function choice

Of the tools used to evaluate the observability and performance of a navigation system described in Section 2.3, two were ultimately chosen for this study: the Lie-algebra continuous-time observability matrix described in (2.31), and the SFIM, for which the formula is described in (2.29):

- The *Observability matrix* $\mathcal{O}$ characterizes local observability. Within the context of this study, it will be used to study which results would optimize local observability across the trajectory, in the absence of measurement noise;
- The inverse of the SFIM (*Standard Fisher Information Matrix*) serves as an estimate of the state covariance matrix of a discrete-time nonlinear system [48]. Although it describes more accurately the batch WLS estimation method rather than sequential bayesian ones such as the EKF, it still accounts for the effect of measurement noise in the state estimation accuracy and is relatively quick to compute.

The localization method in question is expected to present a large disparity in the degree of observability of states (as is shown below in Table 4.1 and Figure 4.4(a) in the values of the condition number of the *Observability matrix*). The SFIM presents a structure close to that of the discrete-time *Observability Gramian* described in Eq. (2.26). Because this *Observability Gramian* is the equivalent of the discrete-time *Observability matrix* multiplied by its transpose, its condition number is expected to be the square value of the *Observability matrix*'s condition number. This would mean that both the *Observability Gramian*, as well as the SFIM, should present condition number values around or below the floating point precision value $eps \simeq 1\mathrm{e}{-16}$, which would render the SFIM in this context as nearly singular.

In order to obtain more precise results, we will therefore take advantage of the fact that the SFIM is a square symmetric matrix that can be constructed from a matrix $\mathcal{I}$ such that SFIM $= \mathcal{I}^T\mathcal{I}$:

$$\mathcal{I} = \begin{bmatrix} R_0^{-1/2} H_0 \\ R_1^{-1/2} H_1 \Phi_{1|0} \\ \vdots \\ R_{m-1}^{-1/2} H_{m-1} \Phi_{m-1|0} \end{bmatrix} \in \mathbb{R}^{3m \times 12}. \tag{4.1}$$

The SFIM's singular values are equal to the square of the singular values of $\mathcal{I}$. Since the observability metrics will be based on the singular values of these matrices, using this Square Root SFIM (SR-SFIM) $\mathcal{I}$

will provide us with numerically more stable results. This approach of using the square root of the Fisher Information Matrix has been mentioned and validated before in the literature as a means of obtaining numerically more stable results [59]. Within the context of orbit determination through relative sensing, the SR-SFIM was used in [58] to predict the performance of a nonlinear least squares batch filter.

Of the observability metrics discussed in Section 2.3.2, two were chosen for optimization: the smallest singular value and the condition number (ratio of largest to smallest singular values):

- Maximizing the smallest singular value (or minimizing its negative value, which will be referred to in this study as *Local Unobservability Index*, or LUI) can be explained as increasing the observability of the least observable subspace in the context of the observability matrix, or decreasing its estimation error variance when considering the SR-SFIM;
- Minimizing the condition number (or its negative reciprocal) should lead to a better conditioned matrix, decreasing the disparity in observability or estimation error between the least and most observable subspaces.

These metrics can be taken from any matrix and used to evaluate how close to singular it is. The observability matrix in question, however, only evaluates local observability within a given point in time. In order to evaluate the observability of a trajectory using the observability matrix, it was decided to average the corresponding metric across time steps. The SR-SFIM matrix is calculated considering a set of observations from a given trajectory, and therefore can be used directly. The negative reciprocal of the condition number is used rather than the condition number itself so that the eclipse condition can be implemented, as it is explained further down in this section.

In total, four different configurations of the objective function were considered, resulting from the combination of two different observability tools and observability metrics. These objective functions are described in Eqs. (4.2), (4.3), (4.4) and (4.5). In these equations, $\mathcal{O}$ denotes the observability matrix-based objective functions, $\mathcal{I}$ the SR-SFIM-based ones, LUI the smallest singular value configurations and CN the condition number ones. The purpose of f_i, f_{eclipse} and f_{period} will be explained in greater detail in the following sections.

$$J^{\mathcal{O}}_{LUI} = -\sum_{i=0}^{N} f_i \sigma_{\min}(\mathcal{O}(x_i)) \tag{4.2}$$

$$J^{\mathcal{O}}_{CN} = -\sum_{i=0}^{N} f_i \frac{\sigma_{\min}(\mathcal{O}(x_i))}{\sigma_{\max}(\mathcal{O}(x_i))} \tag{4.3}$$

$$J^{\mathcal{I}}_{LUI} = -\sigma_{\min}(\mathcal{I}(x)) f_{\text{eclipse}} f_{\text{period}} \tag{4.4}$$

$$J^{\mathcal{I}}_{CN} = -\frac{\sigma_{\min}(\mathcal{I}(x))}{\sigma_{\max}(\mathcal{I}(x))} f_{\text{eclipse}} f_{\text{period}} \tag{4.5}$$

Observation equations

Since the observability matrix does not account for measurement noise, the tranformation from the range and bearing measurement equations to relative position in an inertial frame can be made, allowing for a

simpler formulation of the observability matrix shown in Eq. (2.31).

The SR-SFIM, however, accounts for the measurement noise covariance matrix R in its formula. In a system with fixed noise standard deviation for bearing measurements, the further away the spacecraft, the more innacurate the positioning will be in a direction perpendicular to the relative position vector. For this effect to be taken into consideraton, the observation equations used to calculate the SR-SFIM $\mathcal{I}$ must be split into range and bearing measurements.

Since the accuracy and properties of the measurement system will affect the SR-SFIM, the choice of system is relevant to this study. In the next section, the two relative positioning systems considered in this study and their properties will be described.

Eclipse condition

When the new spacecraft has a wider search space available, it is possible for the Earth to obstruct the field-of-view between it and the formation. This obstruction should be accounted for in the objective function, such that measurements become unavailable during the "eclipse" period. The eclipse condition is based on the model of the illumination factor ν_{IF} described in Section 2.1.3 for the solar radiation pressure model. This eclipse model is adapted to this situation by replacing the sun with the opposing spacecraft in the system, and if $r_{\odot}, \beta \approx 0$, eliminating partial observations from the model.

For the observability matrix-based optimization problems, the use of the negative value of the smallest singular value and of the negative reciprocal of the condition number allows for the "local" objective function of any given time sample be set to zero whenever the eclipse condition is verified, having the desired effect on the final objective function (consisting of the average of all "local" objective functions). This is represented by the factor f_i in Eqs. (4.2) and (4.3).

For the SR-SFIM optimization problems, the eclipsed measurements are omitted. Because these results will be tested in a simulation environment with a sequential filter, we want to discourage the presence of eclipsed periods even further. For this reason, the objective functions of these SR-SFIM optimization problems are multiplied by a factor accounting the percentage of eclipsed time, $f_{\text{eclipse}} = (T_{\text{total}} - T_{\text{eclipsed}})/T_{\text{total}}$.

4.1.3 Relative positioning system

Based on precedents established by previous missions and current available technology, 2 measurement systems were considered in this optimization problem: one is the same relative positioning system described previously with RF ranging and vision-based bearing measurements, and the other is an RF-only method. In this section, we will establish the accuracy of these systems, as well as their associated limitations that will incorporate constraints into the problem.

Vision-based system

In our first relative positioning system, we consider the same system described in [30] for the crosslink UHF study, for which the measurement noise was modelled as Gaussian white noise with standard

deviations of $1/3\,\mathrm{m}$, 35 arcsecond and 35 arcsecond for the range, right ascension and declination measurements, respectively.

The RF ranging and LOS vision-based system should present a maximum measurement distance constraint that needs to be implemented. Without any information on the operational range of the camera system described in [30], the value for this constraint had to be based on the vision-based system of another FF instead.

For the PRISMA mission, the vision-based LOS had a maximum measurement distance of $500\,\mathrm{km}$. The RF system (FFRF) had a maximum distance of $30\,\mathrm{km}$ [60]. However, this RF system was developed *ad-hoc* for a close chaser-target formation. RF ranging systems can have much larger baselines, as shown by the GNSS constellation, of which the signals have even been read at the apogee of a highly elliptic orbit, as demonstrated by the MMS mission [7]. If we consider that the observation satellite has *ad-hoc* RF transmitting capacity adjusted for the orbital distances, then the maximum distance would be defined by the LOS sensing camera at $500\,\mathrm{km}$. The implementation of this constraint as an inequality constraint and restricted search space will be described in Section 4.1.4.

RF-only system

The operating range of vision-based LOS sensing is typically very limited. An alternative solution that could allow for a longer operating distance between satellites would be if the spacecraft in the formation were fitted with an antenna array, allowing them to determine AOA through carrier-phase and time-of-arrival differences. In this scenario, the maximum distance is determined by the RF ranging system, which could be set based on the functional range of the GPS constellation.

Maessen and Gil studied the observability of a spacecraft formation using RF ranging with several receivers on the chief spacecraft [61]. In the article, they modeled each pseudo-range measurement noise as centered white noise. The resulting relative position error from the combination of 3 measurements depended on the arrangement and distance between the receivers. Generally, the larger the baseline between the receivers and the shorter the distance to the transmitter, the more accurate the positioning system was.

This method was tested in the PRISMA mission, which managed to achieve a $1°$ LOS accuracy through this method for low elevation angles [62]. Multipath effects made high elevation angles less robust [60]. However, the distance between the spacecraft was on the order of tens of meters, whereas in this study it is expected to be much larger, which would certainly impact LOS accuracy. For the sake of simplicity, an AOA model will be considered with centered white noise with $1°$ standard deviation for elevation and right ascendancy error, and $1/3\,\mathrm{m}$ for ranging accuracy. Other than a greater LOS measurement error, this system will be given the advantage of having no range limitation within the gravitational sphere of influence of the Earth, as it is considered that the new auxiliary spacecraft is designed with suitable *ad-hoc* RF-transmitting capacity to achieve the necessary range.

The question of whether or not to apply the restriction of synchronizing the orbital motion of the new spacecraft with the formation led to the study of two different configurations for the RF-only measurement system:

- *Free-period configuration*: In this configuration, the new spacecraft has the freedom to have a different orbital period than that of the formation, which equates to a_{new} being a part of the variables x. This configuration incurs the problem that the orbits will become asynchronous, making it difficult to evaluate how the system will perform over time;

- *Fixed-period configuration*: The semi-major axis a_{new} is set equal to that of the formation a_1, synchronizing the orbits and making the orbital motion time-invariant. By evaluating the performance of the system over one orbital period, the assumption can be made that such results will apply to the remainder of the mission.

If we consider that the measurements used to calculate the SR-SFIM are taken from one orbital period of the chief orbit, then the new spacecraft's orbit would not be evaluated in its entirety if its orbital period were greater than that of the chief orbit. For this reason, the measurements are considered to be taken at a constant sampling time of around $90\,\mathrm{s}$ for the duration of the longest orbital period of either the chief or new orbit.

Because this might favour new orbits with longer durations due to the addition of more observations, the free-period configuration objective functions are multiplied by a factor $f_{\text{period}} = T_{\text{chief}}/\max(T_{\text{chief}}, T_{\text{new}})$ that accounts for the amount of extra observations, with T_{chief} the orbital period of the chief orbit and T_{new} the orbital period of the new spacecraft. For the remaining RF/vision-based and RF-only fixed period configurations, this factor is unnecessary as $T_{\text{new}} = T_{\text{chief}}$.

4.1.4 Constraints and Search Domain

In this section, the constraints and search domain of each of the different configurations of the optimization problem are reviewed. We discuss first the formulation of the inter-spacecraft distance restriction for the vision-based bearing measurement system configuration for the new spacecraft. Secondly, the search domain of the configurations with free orbital period and no distance restrictions is discussed (configurations with the observability matrix and with the SR-SFIM for the RF-only system for the new spacecraft). Finally, the same is done for the SR-SFIM optimization with the RF-only system of the new spacecraft, in which the orbital period is fixed to that of the formation.

Inter-satellite range restriction

The constraints and search space in the bearing vision-based observation spacecraft optimization problem are defined by the camera's functional range, set at $500\,\mathrm{km}$. Because the formation spacecraft orbit at a distance of $\sim 10\,\mathrm{km}$ around the chief orbit, a margin of $20\,\mathrm{km}$ was added to the maximum distance between the chief and new orbit, such that $d_{max} = 480\,\mathrm{km}$.

In order to describe the maximum distance constraint with respect to the initial Keplerian elements to be optimized, relative motion is modelled by the following approximated equations in the LVLH frame

derived from the Hill-Clohessy-Wiltshire equations:

$$\begin{cases} \delta r_{x,new/1} & \simeq (a_{new} - a_1) - a_1 \left\{ [e_{new} \cos(\omega_{new}) - e_1 \cos(\omega_1)]) \cos(u_1) + [e_{new} \sin(\omega_{new}) - e_1 \sin(\omega_1)] \sin(u_1) \right\} \\ \delta r_{y,new/1} & \simeq a_1 \{ u_{new} - u_1 + (\Omega_{new} - \Omega_1) \cos(i_1) + 2 \left[e_{new} \cos(\omega_{new}) - e_1 \cos(\omega_1) \right] \sin(u_1) \\ & \quad -2 \left[e_{new} \sin(\omega_{new}) - e_1 \sin(\omega_1) \right] \cos(u_1) \} - \dfrac{3}{2} (a_{new} - a_1)(u_1 - u_{0_1}) \\ \delta r_{z,new/1} & \simeq a_1 \left[(i_{new} - i_1) \sin(u_1) - (\Omega_{new} - \Omega_1) \sin(i_1) \cos(u_1) \right] \end{cases} \tag{4.6}$$

where the subscript 1 refers to the elements of the chief orbit, $u = \omega + M(t)$ represents the mean argument of latitude, with $M(t)$ being the mean anomaly at time t, and u_0 is the mean argument of latitude at t_0 [63]. The mean argument of latitude can be described as being the fraction of an orbit's period that has elapsed since the orbiting body passed the right ascending node, expressed as an angle. Because the chief orbit is considered circular and equatorial, $e_1 = i_1 = 0$. Also, because differences in the semi-major axis a will lead to drift over time, we consider that $a_{new} = a_1 = a$ so that the distance condition can be respected in a time-invariant manner. With these considerations, the relative motion equations are reduced to:

$$\begin{cases} \delta x_{new/1} \simeq -a e_{new} \cos(u_1 - \omega_{new}) \\ \delta y_{new/1} \simeq a \left[u_{new} - u_1 + \Omega_{new} - \Omega_1 + 2 e_{new} \sin(u_1 - \omega_{new}) \right] \\ \delta z_{new/1} \simeq a i_{new} \sin(u_1) \end{cases} \tag{4.7}$$

In [45], these equations are described with the set of description parameters $\{p, s, l, \theta, \alpha\}$ as follows:

$$\begin{cases} \delta x_{new/1} \simeq -p \cos(nt - \theta) \\ \delta y_{new/1} \simeq l + 2p \sin(nt - \theta) \\ \delta z_{new/1} \simeq s \sin(nt - \theta + \alpha) \end{cases} \tag{4.8}$$

Noting that n is the mean angular velocity of both orbits ($n = \sqrt{\mu / a^3}$), and that the mean anomaly M that is used to describe the mean argument of latitude $u = \omega + M$ can be calculated as $M = n(t - t_0)$. This motion can be visualized in Figure 4.1, in which $\phi = \theta - \alpha$.

The maximum distance between the spacecraft is defined as

$$\delta r_{max} = \max_{u_1 \in [0, 2\pi]} \sqrt{\delta r_{x,new/1}^2 + \delta r_{y,new/1}^2 + \delta r_{z,new/1}^2}. \tag{4.9}$$

The worst case scenario approximation that $\alpha = k\pi, k \in \mathcal{Z}$ is made, such that the relative motion in the along-track and cross-track directions reach their greatest magnitude simultaneously. The maximum distance is then reached when $nt - \theta = \pi/2 + 2k\pi, k \in \mathcal{Z}$ if $l > 0$ or $nt - \theta = -\pi/2 + 2k\pi, k \in \mathcal{Z}$ if $l < 0$. This maximum distance constraint is described in both cases through the following expression:

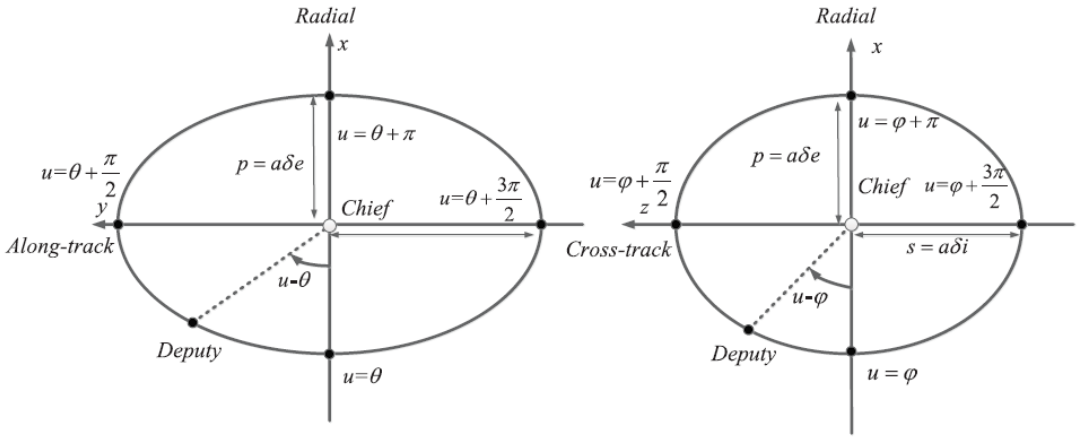

Figure 4.1: Illustration of the parameters used to describe simplified relative motion in the LVLH frame [11].

$$\begin{aligned} &\delta r_{max} < d_{max} \Leftrightarrow \sqrt{(|l| + 2p)^2 + s^2} - d_{max} < 0 \Leftrightarrow \\ &a\sqrt{(|u_{new} - u_1 + \Omega_{new} - \Omega_1| + 2e_{new})^2 + i_{new}^2} - d_{max} < 0 \end{aligned} \tag{4.10}$$

The approximation made with respect to α for the constraint formula is not carried over to the search space. The formulation of the constraint allows for the new spacecraft to always be within the sphere of distance that allows measurements to be taken, but it is over-restrictive in the sense that certain scenarios of relative orbits in the LVLH frame that should be entirely within the range of visibility will not be considered as such, due to the previous approximation being too conservative. For example, if $\alpha = \pi/2 + k\pi, k \in \mathcal{Z}$, the cross-track relative motion will be synchronized with the x radial axis and not the tangential y axis, and the real maximum distance would be somewhere between the peak of the latter or the peak of the tangential direction, which would always be lower than the expression in Eq. (4.10).

Finally, this inter-spacecraft distance restriction also leads to a considerable reduction of the search domain $\mathcal{D}$. The search domain of this problem can be reduced to the last 5 initial Keplerian elements, since the semi-major axis a_{new} will be equal to that of the chief orbit.

Taking into consideration the equations of relative motion in (4.7) and (4.8), when $l = s = 0$, the distance constraint simplifies to $2p < d_{max}$, which translates to the constraint of the search space of the eccentricity $e_{new} \in \left[0, \frac{d_{max}}{2a}\right]$. Similarly, if $p = l = 0$, $|s| < d_{max}$, leading to the constraint of the inclination's search space to $i_{new} \in \left[\frac{d_{max}}{a}, \frac{d_{max}}{a}\right]$. Finally, if $p = s = 0$, $|l| < d_{max}$, which restricts the along-track phase angle of the two orbits such that $u_{new} + \Omega_{new} \in \left[u_1 + \Omega_1 - \frac{d_{max}}{a}, u_1 + \Omega_1 + \frac{d_{max}}{a}\right]$. This constraint can be used to reduce the searh space by replacing the true anomaly ν_{new} with the variable $l_{new} = u_{new} + \Omega_{new}$, to which the latter restriction is applied. The search space of the remaining angular Keplerian elements was not reduced, being kept as $\Omega_{new}, \omega_{new} \in [0, 2\pi]$.

Free range and orbital period

Regarding the free range initial Keplerian elements of the observation spacecraft, a few restrictions are imposed. The spacecraft's altitude must stay above a certain altitude to stop the orbit from decaying too rapidly from atmospheric drag. Most LEO satellites orbit above 300 km for this reason [8]. This allows us to establish the lower boundary for the spacecraft's orbital radius at $R_\oplus + h_{min} = 6378 + 300\text{km}$, considering the Earth's equatorial radius [64]. On the other hand, the spacecraft must not leave the Earth's gravity sphere of influence (given by $R_{SOI} = 9.29 \times 10^6$ km, according to the formula in [65], after which the Sun's gravity becomes dominant). These constraints are applied to the periapse and apogee:

$$\begin{cases} r_p = a_{new}(1 - e_{new}) \geq R_\oplus + h_{min} \\ r_a = a_{new}(1 + e_{new}) \leq R_{SOI} \end{cases} \tag{4.11}$$

For the free period configuration, in order to eliminate the previous constraints, the variables a_{new} and e_{new} are replaced with the variables r_1 and r_2, denoting the apsides (apogee and perigee) of the orbit. These variables can be transformed back into a_{new} and e_{new} through the following equations:

$$\begin{cases} a_{new} &= \dfrac{r_1 + r_2}{2} \\ e_{new} &= \dfrac{|r_1 - r_2|}{r_1 + r_2} \end{cases} \tag{4.12}$$

Using these variables allows for the constraints in Eq. (4.11) to be eliminated by restricting their search space to $r_1, r_2 \in [R_\oplus + h_{min}, R_{SOI}]$. Allowing the apsis of the orbit to have such free range of movement has one major drawback, however: at its upper bound, the orbital period of the new spacecraft will be ~ 3000 times greater than that of the chief orbit, which will lead to a proportionally longer cost function computation time. A compromise was met by lowering the upper bound of the apsis's search space from R_{SOI} to $3\text{e}{+05}$km (~ 6 times greater than the chief orbit's semimajor axis), which leads to a maximum cost function computation time ~ 20 times longer than that of the fixed period configurations. Faster convergence can be achieved in this reduced search space in return for a lowered potential of the optimized solution.

In this configuration the orientation initial COE's have no domain restrictions: $i_{new} \in [0, \pi]$, $\Omega_{new}, \omega_{new}, \nu_{new} \in [0, 2\pi]$.

Free range/Fixed orbital period

For the fixed period configuration of the problem, in which a_{new} is not part of the set of variables to be optimized and is set as $a_{new} = a_1$, the nonlinear constraints in (4.11) become a constant upper bound on the search space of the eccentricity:

$$e_{new} \leq min\left(1 - \frac{R_\oplus + h_{min}}{a}, \frac{R_{SOI}}{a} - 1\right) \tag{4.13}$$

such that $e_{new} \in [0, 0.85]$. Similarly to the previously discussed configuration, the orientation initial COE's have no domain restrictions: $i_{new} \in [0, \pi]$, $\Omega_{new}, \omega_{new}, \nu_{new} \in [0, 2\pi]$.

4.1.5 Metaheuristics

The optimization problem under consideration is nonlinear, and no analytical solution for it was found. In order to find a numeric solution, a nonlinear solver is required. Out of the global nonlinear solvers that were tested, two were used: PSO and a Multi-Start Solver using *MATLAB*'s *fmincon* function's Interior Point algorithm. The *MATLAB* open-source *OPTI Toolbox* version of the PSO algorithm was used [66].

PSO

PSO (Particle Swarm Optimization) is a global optimization solver for bound and linearly constrained problems that does not require the derivatives of the objective function [67]. The algorithm can be described as a coordinate search method in which a particle swarm scheme is used in the search phase to explore the existence of multiple local minima in the objective function.

The *OPTI* Toolbox recommends both this optimizer and the NOMAD algorithm, altough the latter more than the former[1]. Having incurred into problems launching the Toolbox's NOMAD algorithm, the former was chosen instead. Because this is a solver adapted for optimization problems without nonlinear equality or inequality conditions, it was adopted for the problems regarding the observability matrix based objective function and the RF-only measurement system with the SR-SFIM based objective function.

Multi-Start Interior Point

The Interior Point algorithm is the default choice of *MATLAB*'s *fmincon* function to solve nonlinear optimization problems with nonlinear conditions. This algorithm is described extensively in [68]. Being a local optimizer, the algorithm is launched repeatedly using *MATLAB*'s *MultiStart* algorithm[2] to obtain a global solution.

This solver is used in this study for the optimization problem configurations that require nonlinear inequality conditions, mainly the SR-SFIM optimization problems considering vision-based measurements, which include the maximum distance constraint.

4.1.6 Optimization Results

In this section, the results from the different configurations of the optimization are presented and discussed. For each problem, the optimization algorithm was configured to only stop after an 8 hour period. Most optimization problem configurations ran in a computer with 8GB RAM and Intel® Core™ i5-2520M, 2.50 GHz processor. The exceptions were the RF/Vision LUI and CN-optimized configurations, which ran in computers with Intel® Xeon® CPU E5620, 2.40GHz, 49 GB RAM, and Intel® Core™ i7-5820K CPU, 3.30GHz, 32 GB RAM, respectively. The configuration of the optimization algorithms is described in greater detail in Appendix D.1.

[1] `https://www.inverseproblem.co.nz/OPTI/index.php/Probs/GNLP` (Last accessed 04-07-2020).
[2] `https://www.mathworks.com/help/gads/how-globalsearch-and-multistart-work.html` (Last acessed 18/07/2020)

The resulting COE's of the new spacecraft x are shown below in Table 4.1, with the associated optimized objective function values for each configuration of the optimization problem.

Objective function				New S/C orbit states x_{opt}						f(x)
				$a(km)$	e	$i(rad)$	$\Omega(rad)$	$\omega(rad)$	$\nu(rad)$	
Observability Matrix			**CN**	6678	0	1.51	4.9e−03	2.92	1.40	−9.91e−07
			LUI	6678	0	1.54	2.25	6.13	2.12	−9.91e−07
SR-SFIM	**RF/ vision**		**CN**	43399	5.20e−04	1.10e−02	3.41	6.19	2.96	−2.58e−09
			LUI	43399	1.71e−03	7.05e−03	3.63	3.06	5.87	−4.28
	RF only	**Free period**	**CN**	45741.51	8.54e−01	1.40	3.78	4.86	3.39	−9.39e−12
			LUI	39753.95	3.97e−01	1.57	6.28	2.74	2.89	−4.17e−02
		Fixed period	**CN**	43399	8.44e−01	1.56	3.46	4.97	3.32	−9.31e−12
			LUI	43399	3.63e−01	3.25e−01	1.58	2.62	2.08	−4.17e−02

Table 4.1: Optimized states and objective functions.

Before moving onto a detailed analysis of the results of each set of configurations shown in the Table 4.1, a few broad observations are worth noting: 1. The optimized objective function values for the observability matrix-based configurations are very close ($J^{\mathcal{O}}_{LUI} \approx J^{\mathcal{O}}_{CN}$); 2. The resulting objective function values of $J^{\mathcal{I}}_{LUI}$ and $J^{\mathcal{I}}_{CN}$ both consistently indicate that the predicted accuracy performance of the different system configurations should be (in order of most to least accurate) RF/vision $>$ RF-only free period $>$ RF-only fixed period.

Observability matrix

The observability-optimized orbital configurations for the new spacecraft are shown in Figure 4.2(a) below, and the respective reciprocal of the *condition number* and smallest singular value or *LUI* are shown in Figure 4.2(b).

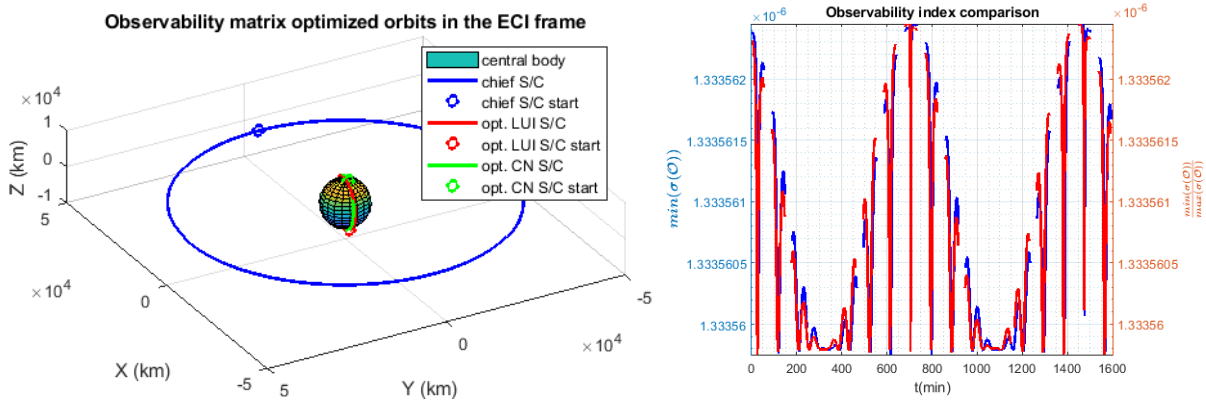

(a) Observability-Optimized new spacecraft orbits. The orbit in blue represents the formation/chief orbit, the red orbit the LUI-optimized new S/C orbit and the green orbit the CN-optimized one.

(b) Evolution of the reciprocal of the CN of the CN-optimized configuration (in red) and (positive) LUI of the LUI-optimized configuration (in blue) over time

Figure 4.2: Optimized orbital configurations, and respective objective functions over time.

The discontinuities in the LUI and CN seen in Figure 4.2(b) are a result of the eclipse condition being verified. These eclipse periods lower the time-averaged objective function, resulting in the values shown in Table 4.1. The oscillations seen in the figure are synchronized with the orbital periods of the spacecraft, (except for the lower frequency oscillations, which are at twice the frequency of the chief

orbit). The oscillations reach their peak near the eclipse periods, and their lowest between them. This might be a result of the variations in relative distance between the spacecraft, which presents similar oscillations.

As mentioned before, the optimized CN and LUI configurations lead to very close results. In trying to understand the reason behind this similarity, the time-evolution of the singular values of each local observability matrix were plotted in Fig. 4.3.

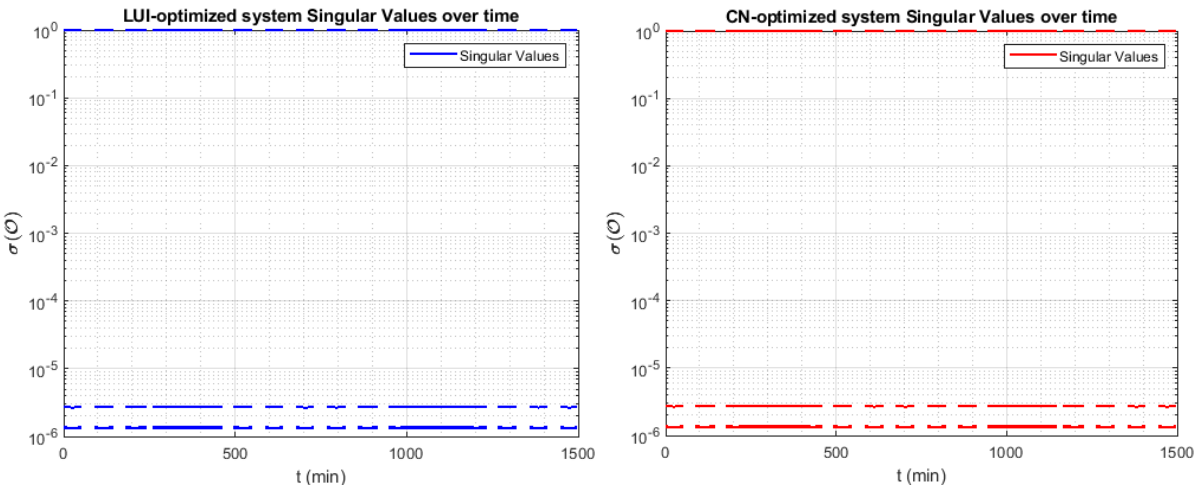

(a) Singular values of the LUI-optimized orbital configuration observability matrix

(b) Singular values of the CN-optimized orbital configuration observability matrix

Figure 4.3: Evolution of the Singular Values of the Observability Matrix over time for the optimized configurations.

As visible in Figure 4.3, the largest 6 singular values are always equal to 1, being linked to the 6 relative states that are directly observable, δr and δv. Regardless of the position of the spacecraft, these states are always equally observable, so long as the S/C are not eclipsed by the Earth. This makes both optimization problem configurations similar.

However, between the two results, the only COE that converged to similar values are the semi-major axis a_{new} and the eccentricy e_{new}. The new S/C orbit also tends to become near polar ($i_{new} \simeq 90°$), which contradicts the results from [45], although this might come as a result of minimizing eclipsed time, which is not accounted for in the article.

In [11], it was suggested that the magnitude of the relative position between the spacecraft was an essential factor for the local observability of the absolute position. While the oscillations in the local objective functions seen in Figure 4.2(b) may be linked to this factor, if greater distances were the most important factor, it would have been possible to achieve better results with auxiliary orbits sitting at the edge of the Earth's sphere of influence at an orbital radius of $R_{SOI} = 9.29 \times 10^6$ km.

We seek to visualize how the difference in orbital radius and interspacecraft distance affect observability. Noting that the observability matrix evaluates observability locally (at a specific point in time rather than a state trajectory), we take the initial states of the chief virtual orbit (described in Table 2.1) and consider that at a given point in time the deputy spacecraft's absolute position vector is aligned with the chief orbit's absolute position vector. The LUI of the observability matrix is evaluated for different

values of the deputy spacecraft's orbital radius (we consider the deputy's speed to be adjusted such that its orbit is always circular). Taking 10000 samples ranging from the edge of the Earth's atmosphere up to the edge of the Earth's gravitational sphere of influence, the plot in Figure 4.4(a) was drawn.

To evaluate the effect of the distance between the spacecraft on observability, a similar method was used, in which the deputy spacecraft was kept within the circular chief orbit, and sampled with a true anomaly covering the entire orbit. Figure 4.4(b) shows the effect that distance has on the observability of the system, when both spacecraft have an equal orbital radius.

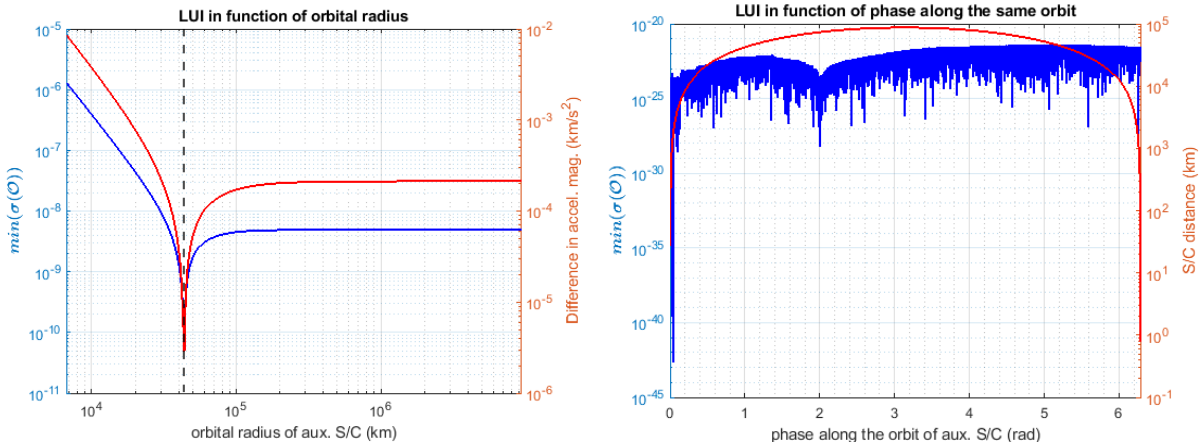

(a) LUI as a function of the orbital radius of deputy spacecraft

(b) LUI as a function of true anomaly of deputy spacecraft

Figure 4.4: Impact of the difference in orbital radius and interspacecraft distance on the observability of the system.

The difference in magnitude of gravitational acceleration was added to the plot in Figure 4.4(a) in order to observe whether its curve would be similar to that of the LUI. The vertical dashed line marks the orbital radius of the chief spacecraft. The same was done to the distance between the spacecraft in function of the difference in true anomaly between the deputy and chief spacecraft in Figure 4.4(b).

These results help to give an insight into which orbital configuration would maximize the observability of the system, and therefore its performance, if no measurement noise was accounted for. In general, these results seem to indicate that large differences in the magnitude of gravitational acceleration are the factor that most affects the local observability of the least observable (absolute) states. In [11], it was also suggested that greater relative radial distances would increase observability. This hypothesis can be derived from the formula of the critical entries of the observability matrix defined by the submatrix $G_1 - G_0$ described in Eqs. (2.32) and (2.33a). These results support this hypothesis because the optimized auxiliary orbits are those which maximize this difference in magnitude, as evidenced by its plot in Figure 4.4(a). They also indicate that increasing the maximum orbital radius of the search space of the problem from $3\text{e}{+05}\text{km}$ to R_{SOI} would likely not have resulted in a lower cost function value, since Figure 4.4(a) shows the maximum local observability taking place at the lower bound of the orbital radius of the new spacecraft.

Figure 4.4(b) shows that, when the spacecraft are at an equal orbital radius, changing the distance between them will not lead to any significant changes in observability. Regardless of the cause of the oscillations seen in Figure 4.2(b), its effect is visibly less significant than that of the difference in orbital

radius.

SR-SFIM RF/vision system

We now evaluate the results of the optimization problems that use the CN and LUI of the SR-SFIM matrix, when considering the RF ranging and vision bearing measurement system for the new auxiliary spacecraft. Because the auxiliary orbits are too close to the chief spacecraft, it is difficult to differentiate them in the ECI frame. The optimized orbits are therefore shown in the LVLH plane in Figure 4.5(a), and in the LI frame centered around the chief orbit in Figure 4.5(b).

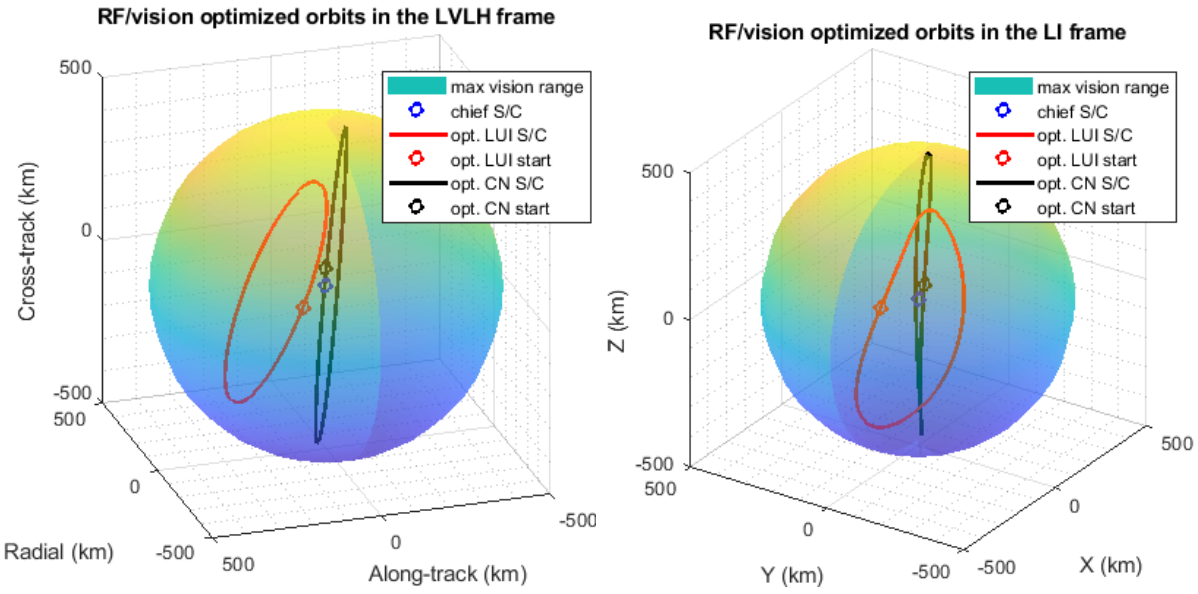

(a) LVLH frame

(b) LI frame centered around the chief orbit

Figure 4.5: Optimized orbits for the RF/vision based system. The relative orbits of the LUI-optimized and CN-optimized systems are displayed in red and black, respectively.

In these configurations, the differences in the results that come from optimizing either the condition number or the smallest singular value are more visible. Since the state error covariance of the relative states increases with the distance between the spacecraft, all singular values are affected by the orbital configuration, unlike with the observability matrix. The objective of optimizing the CN of $\mathcal{I}$ could be described as reducing the difference between the state error covariance of the least and most observable state subspaces. The objective of optimizing the LUI is to reduce the largest state subspace error covariance.

The CN-optimized configuration leads to a new relative orbit that presents wider out-of-plane (cross-track) motion than the LUI-optimized configuration, while remaining closer to the chief orbit in terms of in-plane motion (radial and along-track). Using the parameters from the simplified relative motion model in the LVLH frame described in Eqs. (4.8), the along-track position offset l of the LUI-optimized orbit is greater than that of the CN-optimized one.

By performing singular value decomposition of the SR-SFIM matrix of the optimized results, we can use the right singular vectors to know which states the smallest and largest singular values are most

associated with (similarly to how it is done with the discrete-time observability matrix in [45]). In both configurations, the largest singular value is linked with δv_y, the Y component of the relative velocity of the new spacecraft with respect to the chief orbit in the ECI frame. The lowest singular value, in turn, is associated with r_y in both configurations.

As expected from the results of the observability matrix, the relative range and bearing measurements provide "better" information on the relative states than the absolute ones. As the distance between the spacecraft increases, the impact of changes in the relative position and velocity states on the relative bearing measurements should decrease, and therefore the singular values of $\mathcal{I}$ corresponding to these states should decrease. On the other hand, Figure 4.4(a) shows that greater differences in orbital radius will increase the observability of the absolute states.

In order to better visualize how these different factors impact the LUI and the CN of $\mathcal{I}$, we calculate the values of these objective functions for a new spacecraft placed on orbits with varying degrees of inclination and eccentricity. The remaining orbital elements of the new spacecraft are kept similar to those of the chief orbit. The results in Figure 4.6 were produced by sampling the objective function 30×30 times for both the CN and the LUI, and linearly interpolating these samples for a "smoother" plot.

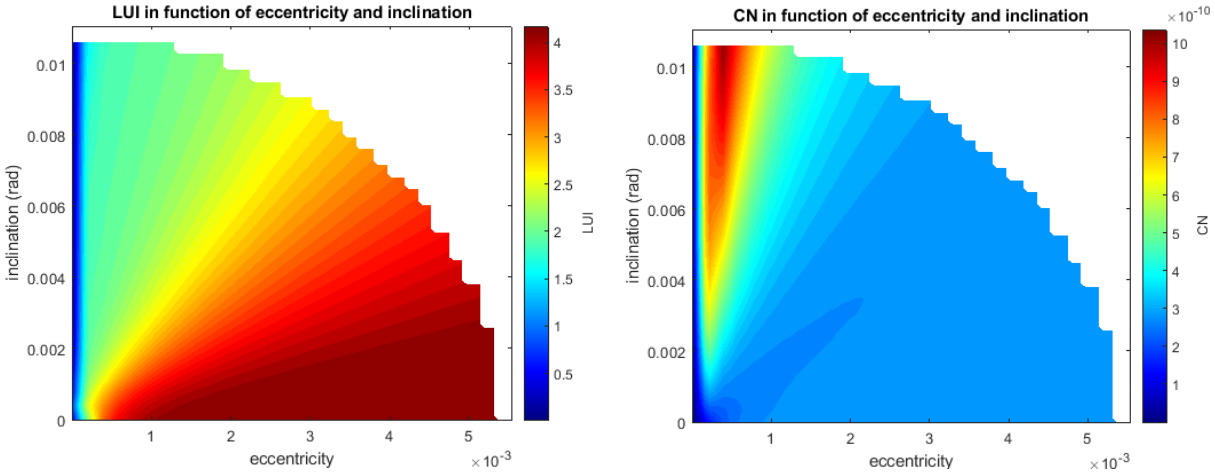

(a) LUI of $\mathcal{I}$ as a function of inclination and eccentricity

(b) CN of $\mathcal{I}$ as a function of inclination and eccentricity

Figure 4.6: Impact of the inclination and eccentricity on the absolute values of the CN and LUI of $\mathcal{I}$ with the RF/vision-based system.

Figure 4.6(a) shows that the absolute value of the LUI generally decreases with the inclination and increases with the eccentricity up until $e \sim 1.5\text{e}{-03}$, where it appears to plateau. Higher degrees of eccentricity of the new spacecraft's orbit will lead to greater differences in orbital radius, which may explain the positive impact of the eccentricity on the LUI.

Because the information available on the absolute states comes from the estimation of the relative states, we should expect the "quality" of the information on the absolute states to be linked to that of the relative states. If relative state estimation becomes more innacurate with greater interspacecraft distances, so should absolute state estimation be negatively impacted by greater distances. This may serve to explain why increasing the inclination of the new spacecraft's orbit would lower the absolute

value of the LUI, and why the latter plateaus at higher eccentricities in Figure 4.6(a). This contradicts the level of inclination and eccentricity presented by the LUI-optimized orbit, although it is important to note that the effect of the remaining orbital parameters is not shown in this plot.

Figure 4.6(b) shows that the CN is lowest at a low eccentricity and high inclination orbit. As previously mentioned, minimizing the CN (or maximizing its absolute value) is equivalent to reducing the difference in information available between the least and most observable state subspaces in order to achieve a better conditioned estimation problem. In this context, this could translate to maximizing the information available on the least observable absolute position states while minimizing that of the most observable state (δv_y in both optimized configurations).

The singular value corresponding to δv_y is lower in the high inclination zone of the search space than in the high eccentricity zone. Because δv_y is associated with in-plane relative motion (since the chief orbit is equatorial), these results lead to the conclusion that relative in-plane motion is more observable than relative out-of-plane motion in this context. By placing the new spacecraft in a high inclination, low eccentricity orbit, in-plane relative motion will be mostly observed from relative bearing measurements while out-of-plane motion will be observed by relative range measurements. At distances greater than $\sigma_\rho/\sigma_\psi = \sigma_\rho/\sigma_\theta = 1.96km$, the relative position estimation error in the plane perpendicular to the relative position vector will be greater than the error in a direction parallel to this vector, and the further away the spacecraft are, the larger this perpendicular error will be due to the fixed angular measurement noise. This would serve to explain why the singular value corresponding to δv_y is lowest at high inclination, low eccentricity orbits in the given search space.

SR-SFIM RF-only system

In this section, we will evaluate the optimized orbital configurations for the SR-SFIM RF-only system. The results are shown in Figure 4.7.

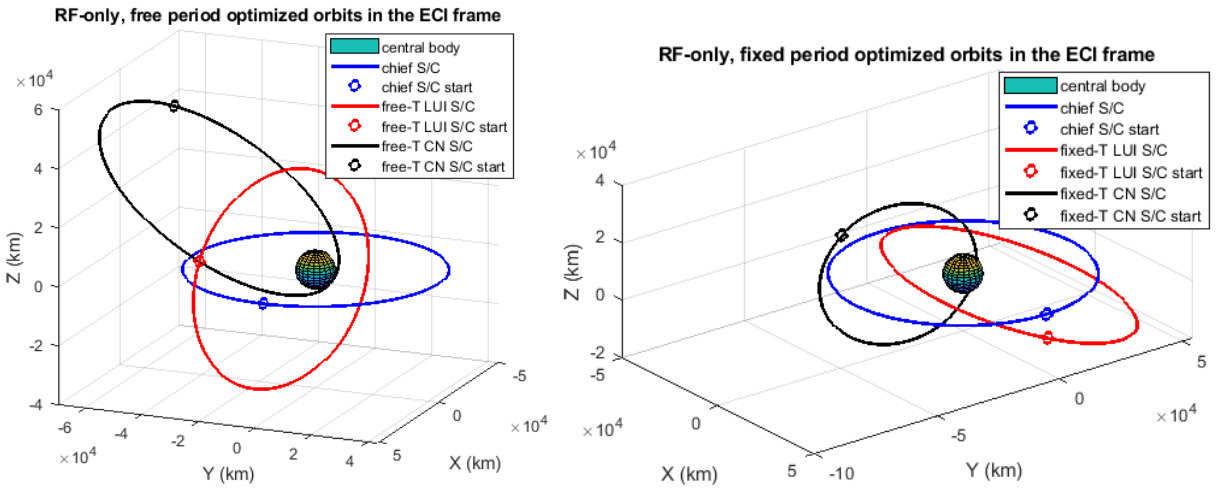

(a) Configurations with free orbital period

(b) Configurations with fixed orbital period

Figure 4.7: Optimized new spacecraft orbits for the RF-only system with free and fixed orbital period. The orbits in blue, red and green represent the formation/chief orbit, the LUI-optimized new S/C orbit and the CN-optimized one, respectively.

Table 4.1 shows that the free-period configurations achieve similar to slightly better results than the fixed-period results. This Table, along with Figures 4.7(a) and 4.7(b), also show how close the free and fixed period CN-optimized new orbits are to each other with respect to the eccentricity, inclination and orbital plane orientation. The free and fixed period LUI-optimized orbits, despite only presenting a similarity in terms of eccentricity, achieve very close results.

None of the four optimized new orbits present Earth-eclipsed periods. Whereas the CN-optimized configurations are highly eccentric, the LUI-optimized orbits present a comparatively small degree of eccentricity ($e_{new} \simeq 0.397$). All optimized orbits are near-polar ($i_{new} \simeq 90°$) with the exception of the fixed period LUI-optimized one.

We perform singular value decomposition as was described in the previous SR-SFIM RF/Vision section to observe which states are most associated with the singular values being optimized. For all the RF-only CN and LUI-optimized configurations, the state most associated with the smallest singular value is once again r_y. For the LUI-optimized and the free period CN-optimized configurations, the state most associated with the smallest singular value is once again r_y. For the fixed period CN-optimized configuration, it is δr_x. In both the CN-optimized configurations, the state most linked with the largest singular value is v_y. In the free period LUI-optimized orbit, this state is v_x, while in the fixed period LUI-optimized orbit it is δv_y.

The singular vectors of $\mathcal{I}$ lead to the belief that, for optimized orbits in which the chief and new spacecraft are relatively far apart, the most easily observed states are associated with the absolute velocity of the chief spacecraft. This conclusion is reached due to the fact that the only configuration in which the largest singular value is linked with a relative velocity state (fixed-period LUI-optimized) is also the configuration in which the chief and new orbit are closest to each other.

The results shown in Figure 4.3 left the impression that the factors that determined the optimized configuration of the auxiliary orbits for absolute positioning performance were avoiding the eclipse condition and difference of magnitude of gravitational acceleration. In these new configurations, the effect of the relative position measurement model and noise should also impact the optimized orbits.

In order to visualize how differences in orbital radius will affect the objective functions in this new configuration, similar plots to the ones shown in Figure 4.4(a) were made for these configurations. Because the SR-SFIM is obtained from a trajectory, as opposed to the observability matrix, which is obtained from a set of states at a given moment in time, the method to create these plots was different. A deputy spacecraft is considered at a circular equatorial orbit starting at its closest point to the chief orbit's initial position. Its semimajor axis is changed, and the (positive) CN and LUI of the resulting SR-SFIM are evaluated for different values of its semimajor axis. The resulting plot is shown in Figure 4.8(a). Similarly, the effect of the eccentricity of the auxiliary spacecraft orbit (when its remaining COE are equal to those of the chief orbit) on the objective function is shown in Figure 4.8(b).

In a circular orbit, the semimajor axis is equivalent to the orbital radius of every point along the trajectory. By observing the impact of a change in semimajor axis on the results, we are also observing the impact of the orbital radius. In Figure 4.8(a), we see that the LUI and CN values only rise up until a certain difference in semimajor axis, after which it starts to drop. The oscillations after this point are likely

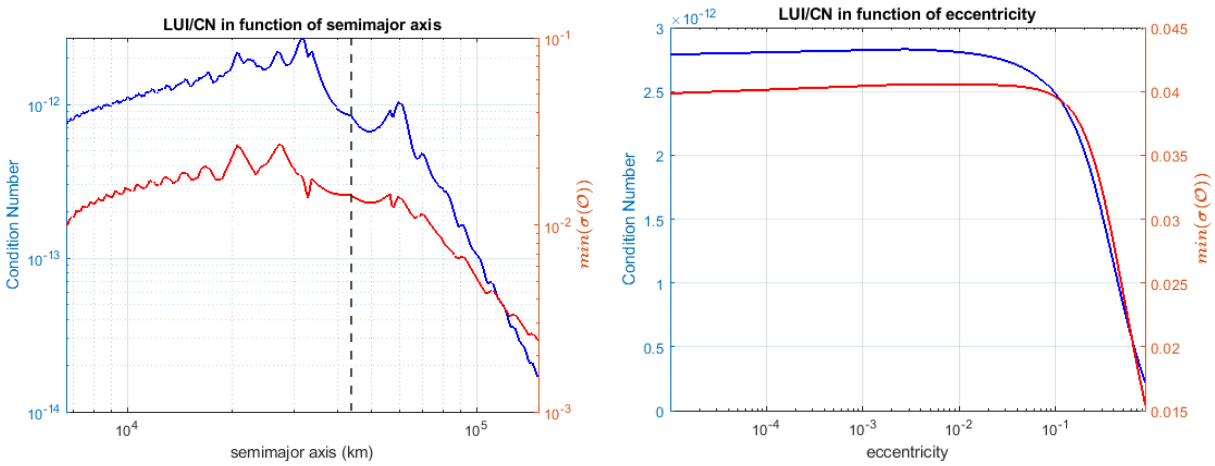

(a) LUI/CN of $\mathcal{I}$ as a function of semimajor axis

(b) LUI/CN of $\mathcal{I}$ as a function of eccentricity

Figure 4.8: Impact of the semimajor axis and eccentricity on the CN and LUI of $\mathcal{I}$ with the RF-only system.

linked with the presence of eclipse periods. This performance degradation may also be explained by the relative bearing measurement noise resulting in a relative positioning error that increases proportionally with the distance between the spacecraft. The orbital period factor f_{period} also plays a part in this degradation for $a_{new} > a_1$.

A similar behaviour takes place in Figure 4.8(b), in which the (positive) CN and LUI values peak at a given eccentricity value and subsequently drop. A maximum of the CN and LUI (or minimum of the objective function) can be found either at a lower or higher orbit of the chief spacecraft. In Figure 4.8(a), the maximum at the lower orbit is higher than that of the higher orbit for both the CN and LUI. This plot was traced for circular and equatorial orbits however, while the optimized configurations are both ellyptical and non-equatorial. The same can be said of the plots in Figure 4.8(b).

4.2 Reduced System Observability Analysis

One large disadvantage of the RF/vision-based localization method is the need for frequent attitude slews to point the cameras of the spacecraft towards one another throughout the measurement schedule described in Section 3.2.1. Considering the addition of the new observation spacecraft, it may be possible to remove the bearing measurements (declination and right ascendancy) while maintaining full state observability, and therefore eliminating the need for these maneuvers. In this section, a study is done on the observability of a new autonomous system in which the chief spacecraft performs relative range and bearing measurements with the new observation spacecraft, therefore having access to its absolute position, but in between the original 6 spacecraft in the formation, only relative range measurements are performed.

4.2.1 Study preliminaries

As described in Section 2.3.3, relative range alone is not sufficient to determine the full position and velocity vector state of a system of multiple spacecraft in the inertial frame when the orbital dynamics are reduced to the two-body problem.

Within a 2 satellite formation, inter-satellite ranging only allows for the observation of nine states out of 12, at most, for two non-coplanar and non-symmetric elliptic orbits, when considering 2-body Keplerian dynamics. The shape, relative orientation and phase along the spacecraft orbits are observable, only the absolute orientation is not [69]. In order to separate observable from non-observable states, we consider the set

$$\text{œ} = \{a_1, e_1, i_1, \Omega_1, \omega_1, \nu_1, a_2, e_2, \nu_2, \theta, \phi_1, \phi_2\} \tag{4.14}$$

in which the states of spacecraft 1 are described by the COE and the states of spacecraft 2 by the shape (a_2, e_2) and phase (ν_2) COE, along with the relative orientation states θ, ϕ_1 and ϕ_2. From these last 3, which are visually represented in Figure 4.9, θ is the angle between the orbital planes, ϕ_1 is the angular distance along the orbit of spacecraft 1 from the periapsis to one of the two intersections of the orbits (being positive in the direction of motion and negative otherwise), and viceversa for ϕ_2 with respect to the orbit of the second spacecraft.

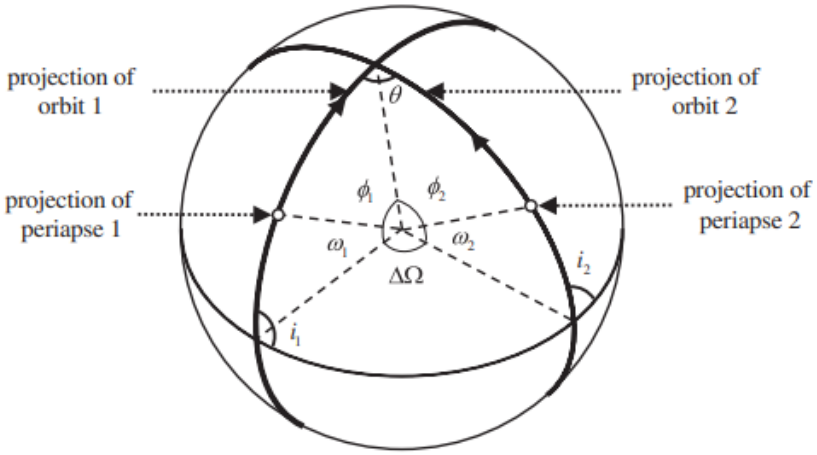

Figure 4.9: Visual representation of relative orientation states θ, ϕ_1 and ϕ_2 [69].

Within the set of states shown in Eq. (4.14), the subset of unobservable states (for two non-coplanar and non-symmetric elliptic orbits) is given by $\text{œ}_{unobs} = \{i_1, \Omega_1, \omega_1\}$, and the subset of observable states is composed by the remaining states: $\text{œ}_{obs} = \{a_1, e_1, \nu_1, a_2, e_2, \nu_2, \theta, \phi_1, \phi_2\}$. θ, ϕ_1 and ϕ_2 can be calculated from the orbital orientation COE from both spacecraft as shown in (4.15) below [69]:

$$\begin{cases} \phi_1 = g_1(\Omega_1, \omega_1, i_1, \Omega_2, i_2) \\ \phi_2 = g_1(\Omega_2, \omega_2, i_2, \Omega_1, i_1) \\ \theta = g_2(\Omega_1, i_1, \Omega_2, i_2) \end{cases}, \tag{4.15}$$

in which the functions g_1 and g_2 are defined as

$$\begin{cases} g_1(\Omega_i, \omega_i, i_i, \Omega_j, i_j) = \tan^{-1}\left(\dfrac{\sin(\Omega_j - \Omega_i)}{\sin(i_i)\cot(i_j) - \cos(i_i)\cos(\Omega_j - \Omega_i)}\right) - \omega_i \\ \\ g_2(\Omega_i, i_i, \Omega_j, i_j) = \arccos\left(\cos(i_i)\cos(i_j) + \sin(i_i)\sin(i_j)\cos(\Omega_j - \Omega_i)\right) \end{cases} . \tag{4.16}$$

Considering that all the states of the chief orbit (here denoted as spacecraft 1) can be deduced from its relative range and bearing measurements with the auxiliary spacecraft, then the knowledge of Ω_1, ω_1 and i_1 from said measurements, conjugated with the knowledge of the relative orientation elements θ, ϕ_1 and ϕ_2 obtained from the ranging measurements between the chief spacecraft and the deputy spacecraft within the original formation may allow for the system in Eqs. (4.16) to be solved with respect to Ω_2, ω_2 and i_2, therefore achieving full state observability.

Other studies led by Wang also analysed the observability of a topology of LOS/ranging-only measurements within networked satellites in a formation, concluding that the relative position within a LVLH frame would be observable in a system in which one S/C pair performs angles-only measurements and the remaining pairs ranging-only [70, 71]. However, in this study we are also interested in the observability of the absolute position in an inertial frame.

In the following section, an analysis will be made to provide empirical evidence that the system is indeed observable.

4.2.2 Observability Analysis

In order to study the observability of the system, first we will reduce the system complexity by eliminating all but one deputy spacecraft from the formation. This reduction is conservative, as it eliminates all measurements performed with other spacecraft.

We want to study the observability of this system using the observability matrix, which requires a mathematical model of state propagation and observation. We first define the set of states as

$$x = \begin{bmatrix} x_1 \\ \delta x_{2/1} \\ \delta x_{new/1} \end{bmatrix} \tag{4.17}$$

where x_1 is the set of position and velocity vector states in the ECI frame that describe the motion of the chief spacecraft, $\delta x_{2/1}$ is the set of position and vector states of deputy spacecraft indexed 2 in the LI frame centered around the chief spacecraft and $\delta x_{new/1}$ is similar for the observation spacecraft, which will be arbitrarily picked as being in the LUI-optimized orbit for the vision-based system shown in Figure 4.5.

These states are propagated considering two-body dynamics, for which the propagation model for the chief spacecraft absolute states is shown in Eq. (3.22) and for the remaining spacecraft's relative inertial states in Eq. (3.23). Because the formulation for the observability matrix of this continuous-time

system would require very complex analytical expressions with high-order Lie derivatives, the adapted formulation for discrete-time nonlinear systems described in Eq. (2.23) was used. This formulation is based on a discrete-time nonlinear system such as the one shown below:

$$x_{k+1} = \phi(x_k)$$
$$y_k = h(x_k),$$

requiring the STM $\Phi_{i/0}$ and observation matrix $H_k = \frac{dh}{dx}(x_k)$ to be calculated for all sampling times t_k in the simulation.

Relative positioning measurements between the chief and observation spacecraft are performed synchronously with range measurements with the deputy spacecraft every 90 seconds, leading to a total of 1000 samples within a simulation period of one formation orbit. Range and bearing measurements are modelled according to the Eqs. (3.15) and (3.17), respectively. The observation matrix H_k is constructed according to the partial derivatives described in Eqs. (3.19), (3.20) and (3.21).

The propagation of the STM and states x_k is performed using *MATLAB*'s *ODE45*, with absolute and relative tolerance of $3\text{e}{-14}$ and $1\text{e}{-20}$, respectively. The obtained observability matrix has full rank of 18, demonstrating the system's observability. To help evaluate the system's observability, the matrix's singular values are shown in Table 4.2 below. The singular values are shown with the most important states of their corresponding right singular vectors, obtained from the singular value decomposition of the observability matrix, as in [45].

States	Singular Values	States	Singular Values	States	Singular Values
$\boldsymbol{\delta v_{y,2/1}}$	$3.95\text{e}{+06}$	$\boldsymbol{v_{y,1}}$	$1.58\text{e}{+04}$	$\boldsymbol{\delta r_{z,new/1}}$	3.07
$\boldsymbol{\delta v_{y,new/1}}$	$2.14\text{e}{+06}$	$\boldsymbol{v_{x,1}}$	$2.86\text{e}{+03}$	$\boldsymbol{\delta r_{z,2/1}}$	1.66
$\boldsymbol{\delta v_{x,new/1}}$	$5.88\text{e}{+05}$	$\boldsymbol{v_{z,1}}$	$1.59\text{e}{+02}$	$\boldsymbol{\delta r_{y,new/1}}$	1.45
$\boldsymbol{\delta v_{x,2/1}}$	$5.35\text{e}{+05}$	$\boldsymbol{\delta r_{x,2/1}}$	21.1	$\boldsymbol{r_{x,1}}$	$2.19\text{e}{-02}$
$\boldsymbol{\delta v_{z,new/1}}$	$2.41\text{e}{+05}$	$\boldsymbol{\delta r_{x,new/1}}$	9.99	$\boldsymbol{r_{z,1}}$	$5.17\text{e}{-03}$
$\boldsymbol{\delta v_{z,2/1}}$	$1.69\text{e}{+05}$	$\boldsymbol{\delta r_{y,2/1}}$	7.62	$\boldsymbol{r_{y,1}}$	$7.13\text{e}{-04}$

Table 4.2: List of singular values and associated states of the observability matrix for the ranging-only deputy spacecraft system sorted in decreasing order.

The values in Table 4.2 show that the observability matrix has a large condition number ($5.55\text{e}{+09}$), indicating that the system is ill-conditioned. The previously mentioned studies by Wang also produced condition number results in a similar order of magnitude [71]. The smallest singular values are associated with the absolute position of the chief spacecraft in the ECI frame. The degree of observability of the relative states of the deputy spacecraft is on par with that of the relative states of the new/observation spacecraft. The reduced system's observability analysis results will be validated in the next chapter through simulation with the sequential filter described in Section 3.3, with removed bearing measurements between the formation.

Chapter 5

Simulation Results

We seek to evaluate the results from the optimization problems in the previous section. However, in order to test the new configurations with the filter proposed in Section 3.3, a new measurement schedule with the added spacecraft needs to be conceived.

Two sets of results were obtained with different measurement schedules: one in which the assumption is made that no spacecraft can measure its position with more than one other spacecraft simultaneously, and therefore an adapted schedule is needed (in Subsection 5.1); and another in which the original schedule of the formation runs parallel to the measurements between the chief and the new spacecraft (in Section 5.2).

Finally, in Section 5.3, simulations will be used to validate the hypothesis that the formation does not require relative bearing measurements between each other as long as the chief spacecraft's position is known from relative positioning measurements with the observation spacecraft.

The simulations will be run with the Monte-Carlo method, with $M = 40$ samples, in which the initial position state estimates will be placed $100\,\mathrm{m}$ away from the real initial position in a random direction, different for each simulation run. The simulation period is kept at one orbital period of the original formation (~ 25 hours).

5.1 Adapted schedule

In order to test the optimized orbital configurations in a simulation environment, a new measurement schedule is necessary. The original schedule in Table 3.1 was made with the assumption that spacecraft can only perform relative positioning measurements with one other spacecraft at any given time. Within one measurement cycle composed of five measurement sets, each spacecraft gets the opportunity to perform measurements with every other spacecraft in the formation, with three different pairs performing measurements simultaneously in each set.

The same considerations were taken in designing the new measurement schedule shown in Table 5.1 below. Because adding a spacecraft leads to an odd total number of spacecraft, one spacecraft needs to be left out every set of measurements. The schedule therefore holds 6 measurement sets,

each leaving a different deputy spacecraft excluded from the measurements. The measurement set in which the chief spacecraft should be left out was discarded from the schedule. This decision was made to improve the absolute positioning of the chief spacecraft at the expense of a slight inbalance in the measurement schedule, since three spacecraft pairs never perform measurements together.

Time Interval, min	S/C Pairs
$[t_0 + 9 + 60k, t_0 + 10 + 60k]$	**1-2 3-4 5-6**
$[t_0 + 19 + 60k, t_0 + 20 + 60k]$	**1-3 2-4 5-7**
$[t_0 + 29 + 60k, t_0 + 30 + 60k]$	**1-4 2-7 3-6**
$[t_0 + 39 + 60k, t_0 + 40 + 60k]$	**1-5 2-6 3-7**
$[t_0 + 49 + 60k, t_0 + 50 + 60k]$	**1-6 2-5 4-7**
$[t_0 + 59 + 60k, t_0 + 60 + 60k]$	**1-7 3-5 4-6**

Table 5.1: Adapted measurement schedule with observation spacecraft, where t_0 is the starting epoch and $k \in \mathbb{Z}^+$

The simulation results shown in Table 5.4 are produced with $M = 40$ Monte-Carlo simulation runs, simulation period of 89 976 s, initial absolute and relative position error of 100 m in a random direction, and 10 cm/s for the absolute and relative speed in the same manner. The process covariance matrix Q is defined with $q_j = (1\mathrm{e}{-09})^2(\mathrm{km/s}^{2.5})^2, \forall j \in \{2, \ldots, 6\}$, according to Eq. (3.9). Exceptions are made for the entries corresponding to the process noise of the chief and new spacecraft's acceleration (Q_1 and Q_7), which are multiplied by a factor α such that $q_1 = \alpha_1(1\mathrm{e}{-09})^2(\mathrm{km/s}^{2.5})^2$ and $q_7 = \alpha_{new}(1\mathrm{e}{-09})^2(\mathrm{km/s}^{2.5})^2$ that maximizes the absolute positioning accuracy of the filter, in order to explore the full potential of the new configurations. The values of α_1 and α_{new} for each configuration were found through trial and error, and are shown in Table D.4 in Appendix D.2. Finally, the mean positioning error only accounts for the position error after 200 minutes, so as to not account for the initial condition error.

			Absolute position error (km)	Relative position mean error (m)						
			$\overline{e}_{1,\mathrm{rms}}$	$\overline{e}_{2/1,\mathrm{rms}}$	$\overline{e}_{3/1,\mathrm{rms}}$	$\overline{e}_{4/1,\mathrm{rms}}$	$\overline{e}_{5/1,\mathrm{rms}}$	$\overline{e}_{6/1,\mathrm{rms}}$	$\overline{e}_{7/1,\mathrm{rms}}$	$\overline{e}_{2:6/1,\mathrm{rms}}$
Without aux. S/C	**PVA filter [30]**		—	2.811	4.072	4.177	4.172	2.638	—	3.574
	New filter		1.730	1.201e−01	1.296e−01	1.456e−01	1.373e−01	1.271e−01	—	1.319e−01
RF/ vision		**CN**	1.801	1.458e−01	1.577e−01	1.716e−01	1.656e−01	1.433e−01	5.043	1.568e−01
		LUI	1.783	1.463e−01	1.600e−01	1.778e−01	1.668e−01	1.410e−01	5.680	1.584e−01
RF only	**Free period**	**CN**	3.885	1.480e−01	1.744e−01	1.925e−01	1.778e−01	1.464e−01	8.104e+04	1.678e−01
		LUI	2.310	1.457e−01	1.579e−01	1.797e−01	1.675e−01	1.442e−01	6.103e+03	1.590e−01
	Fixed period	**CN**	3.675	1.502e−01	1.742e−01	2.001e−01	1.774e−01	1.456e−01	6.616e+04	1.695e−01
		LUI	2.286	1.455e−01	1.597e−01	1.787e−01	1.654e−01	1.451e−01	2.896e+03	1.589e−01

Table 5.2: Mean absolute and relative error for the different orbital configurations of the new observation spacecraft with the adapted measurement schedule

To help compare the results in Table 5.2, as well as their respective dispersion of values within the multiple Monte-Carlo runs, Figure 5.1 displays said data in bar plot format. Figure 5.1(a) presents the Monte-Carlo averaged absolute error values $\overline{e}_{1,\mathrm{rms}}$, with the error bars indicating the largest and smallest error values obtained in the Monte-Carlo runs. Figure 5.1(b) displays in a similar manner the values of $\overline{e}_{2:6/1,\mathrm{rms}}$, and Fig. 5.1(c) the values of $\overline{e}_{7/1,\mathrm{rms}}$.

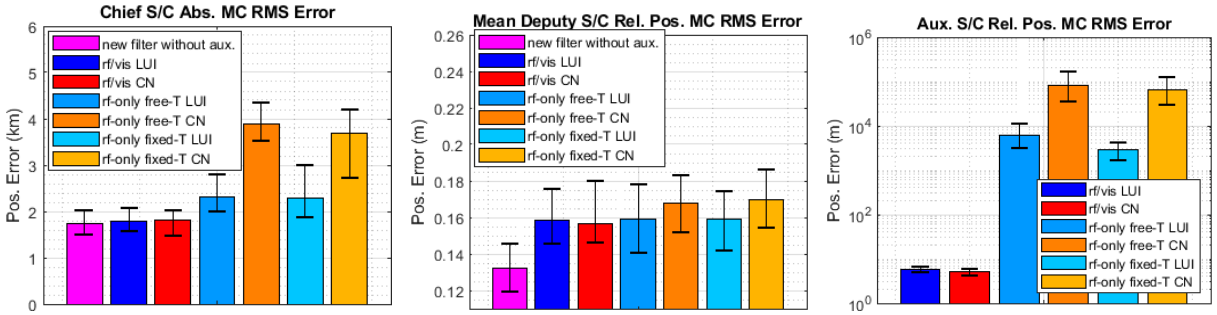

(a) Chief spacecraft absolute position Monte-Carlo averaged RMS error.

(b) Formation's deputy spacecraft mean relative position Monte-Carlo averaged RMS error (excluding the aux. spacecraft).

(c) Auxiliary spacecraft relative position Monte-Carlo averaged RMS error.

Figure 5.1: Monte-Carlo averaged RMS error results for the configurations with the adapted schedule, with upper and lower error bounds.

Regarding the results in Table 5.2 and Figure 5.1, it is possible to observe that, within this setting, no configurations of the new spacecraft are capable of improving the absolute positioning accuracy or the mean relative positioning accuracy between the original deputy spacecraft. The design of the measurement schedule is the most likely explanation. Because of the adapted schedule's design, less measurements are made per number of states (6 states were added but the amount of measurements being performed per unit of time is the same). Each spacecraft also needs to wait longer to fix its position with respect to the chief spacecraft. This has negative consequences for both the relative and absolute positioning accuracy of the system, since each spacecraft will present a greater relative positioning error when it finally fixes its position with respect to the chief spacecraft.

The RF/vision based systems outperform the RF-only system in all positioning metrics considered.

It appears that, despite the wider search space available to RF-only configurations due to the lack of a maximum distance constraint, an optimal solution that can match the absolute positioning accuracy of the RF/vision systems was not found. The comparison of the objective function values between different configurations in Table 4.1 accurately predicts the RF/vision systems to outperform the RF-only systems. It should also predict the RF-only free-period configurations either matching or outperforming its fixed-period counterparts. However, Table 5.2 shows the latter slightly outperforming the free-period configurations in terms of absolute positioning and relative positioning with respect to the auxiliary spacecraft. Figure 5.1 shows most of the differences between the fixed and free-period configurations taking place within the Monte-Carlo error bounds. This makes it unclear whether this latter observation would hold true if a greater number of Monte-Carlo samples had been used.

For the results produced with the adapted schedule, the CN and LUI optimized configurations only present one coherent difference in terms of performance: the LUI configurations outperform their CN counterparts in terms of absolute positioning. With regards to relative positioning performance, in the RF/Vision configurations the CN-optimized results outperform the LUI-optimized ones, whereas in the RF-only configurations the opposite takes place.

Below, in Figure 5.2, the Monte-Carlo averaged absolute positioning error for the different configurations compared with the results with no auxiliary spacecraft are displayed for one orbital period. A plot of the absolute positioning prediction model error is added to compare these results to the results that would be obtained if only the initial position estimate and filter's propagation model were used to generate an estimate of the resulting trajectory, with no measurement updates. In Figure 5.3, a similar plot is shown for the mean relative positioning error for the original deputy spacecraft in the formation.

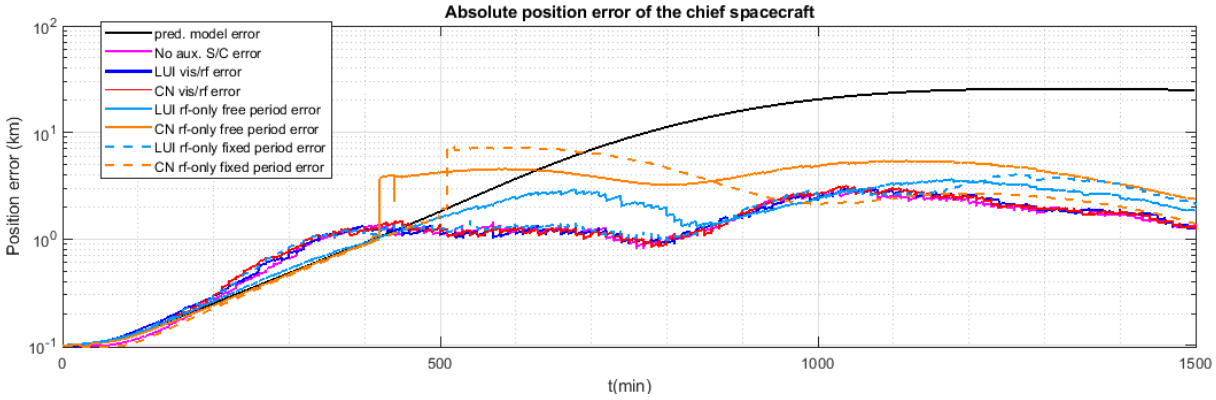

Figure 5.2: MC-averaged absolute position error of the chief spacecraft for each configuration with the adapted schedule, compared with the results from the formation without the new spacecraft and with the prediction model-only estimation.

Figure 5.2 shows how the absolute positioning error of the CN-optimized RF-only free and fixed period configurations consistently explodes at the $\sim 420\,\mathrm{min}$ and $\sim 500\,\mathrm{min}$ mark respectively, followed by a period of convergence. A more in-depth study behind this behaviour will be made further below.

Given the already described setbacks introduced by this measurement schedule, a new more favourable measurement schedule was designed. This new schedule design's objective is to eliminate these setbacks and hopefully produce results that will further improve both the absolute and relative positioning

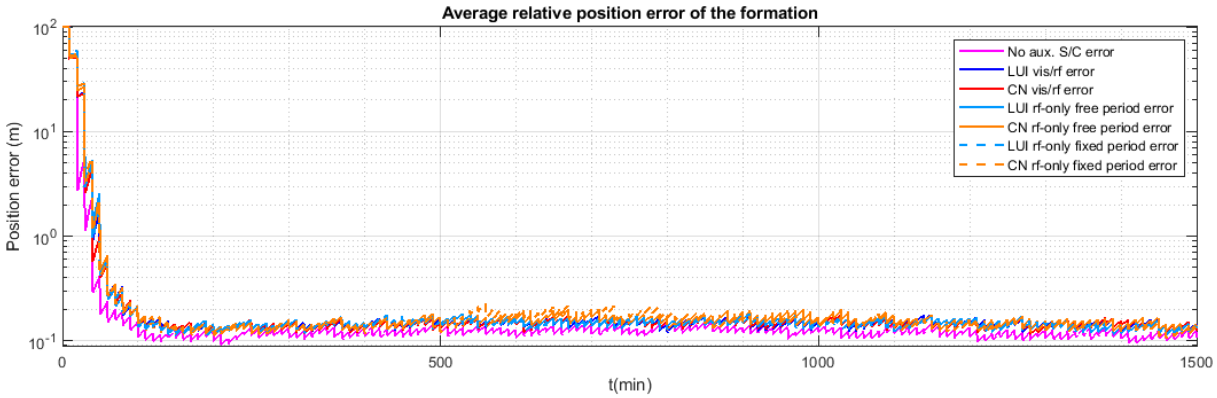

Figure 5.3: MC-averaged mean relative position error of the deputy spacecraft (not counting the added spacecraft) for each configuration with the adapted schedule, compared with the results from the formation without the new spacecraft.

of the original formation.

5.2 Parallel schedule

The simulations are now run with a new measurement schedule, set in a way such that the measurements between the chief and new spacecraft run parallel to the original measurement schedule shown in Table 3.1, so that no spacecraft is left out of any measurement set. The new measurement schedule is shown in Table 5.3. The chief spacecraft is denoted with the index 1, the new spacecraft with the index 7 and the remaining deputy spacecraft of the original formation are denoted $2-6$. The measurements between the chief and new spacecraft and within the original formation spacecraft are made simultaneously.

Time Interval, min	S/C Pairs
$[t_0+9+50k, t_0+10+50k]$	**1-2 3-4 5-6 1-7**
$[t_0+19+50k, t_0+20+50k]$	**1-3 2-5 4-6 1-7**
$[t_0+29+50k, t_0+30+50k]$	**1-4 2-6 3-5 1-7**
$[t_0+39+50k, t_0+40+50k]$	**1-5 2-4 3-6 1-7**
$[t_0+49+50k, t_0+50+50k]$	**1-6 2-3 4-5 1-7**

Table 5.3: Original measurement schedule with added measurements between chief and observation spacecraft, where t_0 is the starting epoch and $k \in \mathbb{Z}^+$

With this new schedule, the Monte-Carlo simulations are run similarly to those described in Section 5.1. The time-averaged results after 200 minutes are shown in Table 5.4 below. Analogous to Figure

5.1, the bar plots of the Monte-Carlo averaged chief spacecraft absolute position RMS error $\overline{e}_{\mathbf{1,rms}}$, the formation's original deputy spacecraft mean relative positioning RMS error $\overline{e}_{\mathbf{2:6/1,rms}}$ and the new spacecraft's relative positioning RMS error $\overline{e}_{\mathbf{7/1,rms}}$ with their error bounds are shown in Figures 5.4(a), 5.9(b) and 5.4(c), respectively.

			Absolute position error (km)	**Relative position mean error (m)**						
			$\overline{e}_{\mathbf{1,rms}}$	$\overline{e}_{\mathbf{2/1,rms}}$	$\overline{e}_{\mathbf{3/1,rms}}$	$\overline{e}_{\mathbf{4/1,rms}}$	$\overline{e}_{\mathbf{5/1,rms}}$	$\overline{e}_{\mathbf{6/1,rms}}$	$\overline{e}_{\mathbf{7/1,rms}}$	$\overline{e}_{\mathbf{2:6/1,rms}}$
Without aux. S/C	**PVA filter [30]**		—	2.811	4.072	4.177	4.172	2.638	—	3.574
	New filter		1.730	1.201e−01	1.296e−01	1.456e−01	1.373e−01	1.271e−01	—	1.319e−01
RF/ vision		**CN**	1.716	1.218e−01	1.312e−01	1.425e−01	1.353e−01	1.260e−01	5.139	1.314e−01
		LUI	1.697	1.210e−01	1.321e−01	1.502e−01	1.380e−01	1.276e−01	5.660	1.338e−01
RF only	**Free period**	**CN**	6.970	1.455e−01	1.795e−01	2.099e−01	1.705e−01	1.400e−01	9.183e+04	1.691e−01
		LUI	2.126	1.204e−01	1.317e−01	1.448e−01	1.394e−01	1.308e−01	1.434e+04	1.334e−01
	Fixed period	**CN**	3.327	1.251e−01	1.392e−01	1.590e−01	1.432e−01	1.283e−01	5.712e+04	1.390e−01
		LUI	1.971	1.221e−01	1.322e−01	1.461e−01	1.390e−01	1.289e−01	7.182e+03	1.337e−01

Table 5.4: Mean absolute and relative error for the different orbital configurations of the new observation spacecraft with the original formation measurement schedule

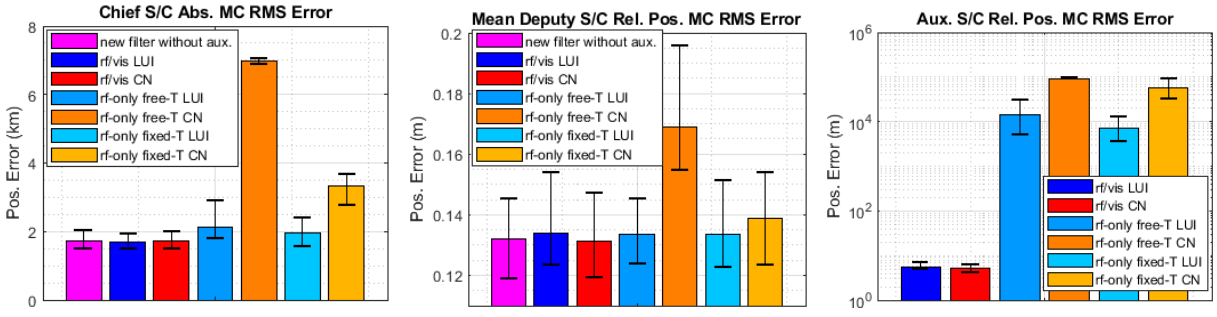

(a) Chief spacecraft absolute position Monte-Carlo averaged RMS error.

(b) Formation's deputy spacecraft mean relative position Monte-Carlo averaged RMS error (excluding the aux. spacecraft).

(c) Auxiliary spacecraft relative position Monte-Carlo averaged RMS error.

Figure 5.4: Monte-Carlo averaged RMS error results for the configurations with the parallel schedule, with upper and lower error bounds.

The new results in Table 5.4 shows most configurations matching more closely the relative positioning accuracy of the formation's deputy spacecraft ($\overline{e}_{\mathbf{2:6/1,rms}}$) of the original configuration with no auxiliary spacecraft. The differences between these accuracies occur at a negligible mm-level. The exceptions are the RF-only CN-optimized configurations, which present more visibly worsened positioning performances.

Regarding absolute positioning performance, with the parallel schedule both RF/vision configurations now match more closely the results of the original configuration, while the RF-only configurations continue to underperform it. The RF/Vision configurations achieve slightly better absolute positioning accuracies than the original formation with this schedule, although this difference is not significant compared to the Monte-Carlo error bounds seen in Fig. 5.4. These observations can be simply attributed to the more favourable aspects of the parallel schedule (spacecraft fix their position with respect to the

chief more frequently, and more measurements per set).

However, the RF-only CN-optimized configurations continue to underperform considerably with respect to the remaining configurations in both absolute and relative positioning accuracy. This may be a result of an inadequate tuning of the q_1 and q_7 parameters of the process covariance matrix Q, which are adapted for each configuration in order to maximize the system's performance as much as possible. Due to the long computation time of each simulation run, these parameters were tuned through a dedicated manual search.

No definite conclusions can be drawn regarding the worsened absolute positioning performance of the configurations with RF-only auxiliary spacecraft when compared to the formation with no auxiliary spacecraft. The following potential explanations can be given:

- A poor tuning of the q_1 and q_7 parameters, as mentioned above;
- The choice of the optimization problem's objective function does not accurately reflect the accuracy/performance of the system (this will be discussed in greater detail below);
- The RF-only system underperforms the base RF/vision system of the original formation in such a way that it is unable to improve the accuracy of the system.

Similarly to the previous schedule, no coherent difference is found between the CN and LUI optimized configurations with respect to the relative positioning performance of the new spacecraft: while with the RF/Vision system, the CN-optimized configuration outperforms the LUI-optimized one in this regard, with the RF-only system the CN-optimized configurations underperform the LUI-optimized ones instead. In terms of absolute positioning, the order of accuracy remains.

In Figure 5.5, the MC-averaged absolute positioning error for the different configurations compared with the original formation's performance are displayed for one orbital period. In Figure 5.6, the same is done for the mean relative positioning error for the original deputy spacecraft in the formation.

Figure 5.5: MC-averaged absolute position error of the chief spacecraft for each configuration with the parallel schedule, compared with the results from the formation without the new spacecraft and with the prediction model-only estimation.

For this schedule, Figure 5.5 once again shows the RF-only CN-optimized free and fixed-period configurations becoming unstable at the 420 min and 500 min marks, respectively. It is important to

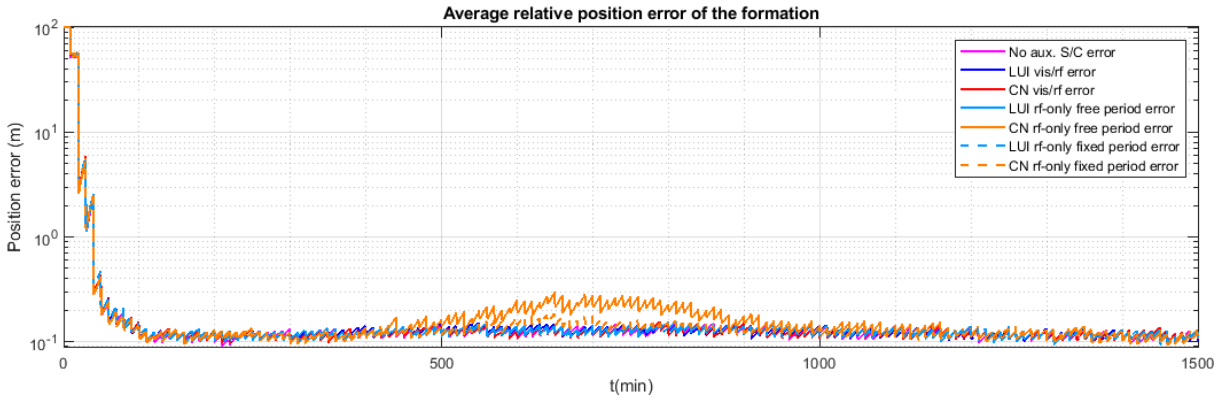

Figure 5.6: MC-averaged mean relative position error of the deputy spacecraft (not counting the added spacecraft) for each configuration with the parallel schedule, compared with the results from the formation without the new spacecraft.

understand why this takes place, and whether it can be prevented or predicted through the objective function.

In trying to explain this behaviour, the following potential justifications were put forth:

- A period of eclipse between the chief and the new spacecraft leads to a drift of the relative position knowledge;
- The RF-only CN-optimized orbits true non-keplerian trajectories are too different from the filter's keplerian prediction model;
- The EKF's relative state dynamics and/or observations drift due to a poor linear approximation to a pronounced nonlinear behaviour.

As mentioned in the previous chapter, none of the SR-SFIM optimized configurations present eclipsed periods according to the simplified measurement schedule used in the objective functions. However, the schedule considered in these simulations implies more frequent measurements, at different timestamps. Upon verification of whether or not the CN-optimized RF-only configurations had or not any instances of obstructed view with the new schedule, it was confirmed that no measurements are eclipsed.

Another possible justification is a large drift due to non-keplerian dynamics unnacounted for in the filter's prediction model. This drift should be more pronounced for these two configurations due to the perigee of these orbits being so close to the Earth, where the non-keplerian perturbations are more noticeable (as seen in Figure 2.3). To evaluate this possibility, a comparison is made in Figure 5.7(a) of the relative position error of the RF-only fixed-period CN-optimized spacecraft with respect to the chief spacecraft between the EKF (red) and its keplerian prediction model (black). The result is shown in Figure 5.7(a).

Figure 5.7(a) shows how the keplerian prediction model's error rises faster around the $500\,\mathrm{min}$ mark, when the new spacecraft passes close to its perigee. The relative position estimation error also starts diverging at this point.

The EKF in question is built on the assumption that the process noise covariance matrix is constant. The inconstant behaviour of the error between the true trajectory and the filter's prediction model may

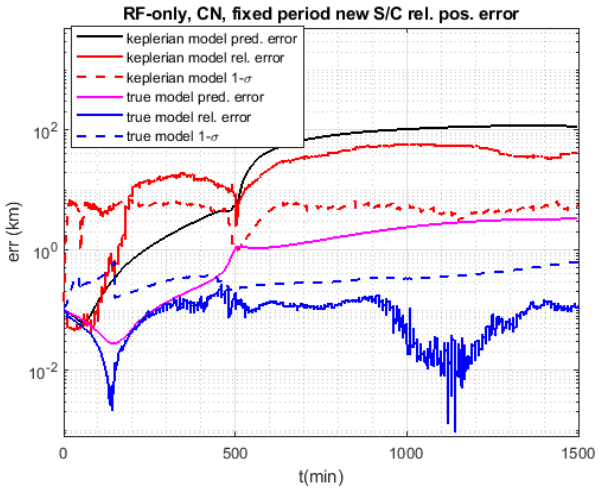

(a) Drift of the relative position error of the auxiliary spacecraft with respect to the chief spacecraft.

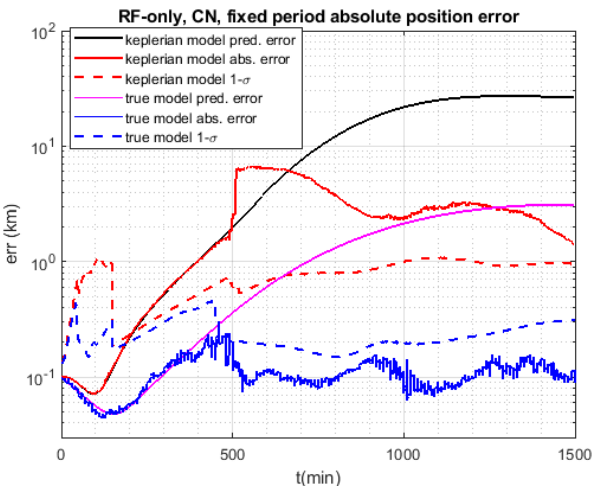

(b) Drift of the absolute position error of the chief spacecraft.

Figure 5.7: Drift of the positioning error of the RF-only CN-optimized fixed-period configuration, plotted against the drift of the filter's keplerian prediction model error and its respective estimated position state error standard deviation. These plots are compared with those of a filter with a perfect prediction model.

justify the filter's divergence. For that reason, Figure 5.7(a) also includes the plot of the evolution of the square-root of the L2-norm of the diagonal entries of P_k^+ (or P_k^- for the time steps with no new measurements) corresponding to the relative position states of the new spacecraft (dashed red). Comparing this plot with that of the real estimation error shows that the filter does not accurately keep track of the new spacecraft's relative positioning error, particularly after the $500\,\mathrm{min}$ mark.

In order to verify whether the problem disappears with a more accurate prediction model, a new simulation was run in which the filter's prediction model is based on the continuous-time model was used to generate the real trajectory (described in Appendix C). This is an excessively optimistic scenario, as it is unrealistic to expect the filter's model to be completely accurate. The discretization of the continuous-time model was still performed with *ODE45* as described in Section 3.3. The values of α_1 and α_{new} were re-tuned to this new model, such that $\alpha_1 = 1\mathrm{e}{-02}$ and $\alpha_{new} = 1\mathrm{e}{+04}$. These results were added to Figure 5.7(a), with the filter's prediction model error due to the initial position error (pink), its estimation error (blue) and corresponding estimated standard deviation (dashed blue). A similar plot was done for the absolute position error of the chief spacecraft in Figure 5.7(b).

Figures 5.7(a) and 5.7(b) show how the incorporation of the true model into the EKF's prediction phase eliminate the $500\,\mathrm{min}$ mark burst of error and greatly improved the positioning performance (both absolute and relative positioning error lowers to a $\sim 100m$-level). These results favour the hypothesis that the $500\,\mathrm{min}$ mark drift takes place due to a sudden increase in the error between the filter's predicted and the true trajectories.

Potential solutions to this problem could be the use of a more accuracte prediction model as demonstrated, or of an Adaptive EKF, capable of estimating the process noise covariance Q_k with each time-step, such as the one described in [72]. Better tuning the values of the parameters α_1 and α_{new} may also help to reduce the disparity between the estimated state covariance and the true error.

Another potential explanation for the sudden drift around the $500\,\mathrm{min}$ mark that should not be ex-

cluded could be the presence of a pronounced nonlinearity in the EKF's dynamics or observation models. The EKF is built on the approximation of nonlinear dynamic and observation models to linearized ones. If these models present strong nonlinear behaviour, this approach of linearization may cause the filter to diverge [73].

In order to verify whether or not this explanation is plausible, the range, right ascendancy and declination measurements between the RF-only fixed period CN-optimized configuration and the chief spacecraft are plotted in Figures 5.8(a), 5.8(b) and 5.8(b), respectively. The plots also show the true measurements ($y = h(x)$) and the estimated measurements ($\hat{y} = h(\hat{x})$).

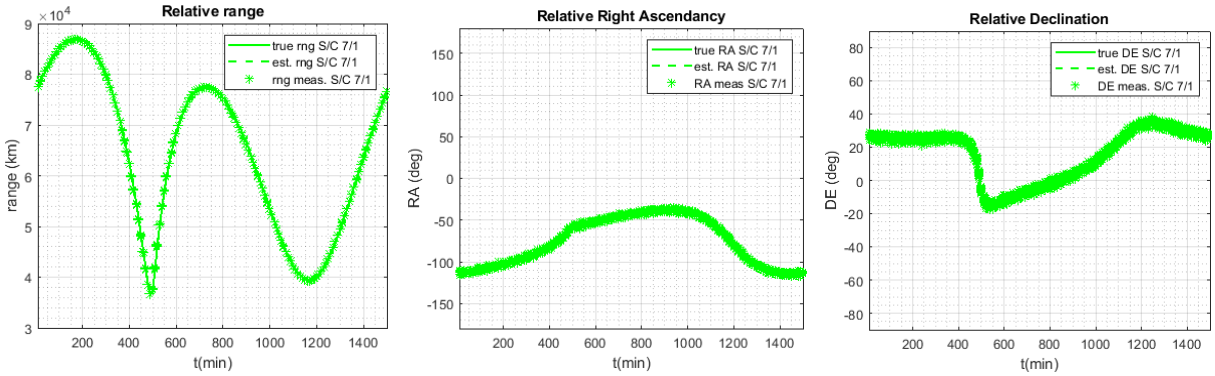

(a) Relative range measurements, true and estimated range between the chief and aux. spacecraft.

(b) Relative right-ascendancy measurements, true and estimated right ascendancy between the chief and aux. spacecraft.

(c) Relative declination measurements, true and estimated declination between the chief and aux. spacecraft.

Figure 5.8: Relative position measurements between the chief spacecraft and the RF-only, fixed period CN-optimized configuration, plotted with the true and estimated observations.

In Figure 5.8, the error between the true and estimated observations is too small for these to be distinguished in the plots. Regardless, it is possible to observe how the abrupt changes in the measurement values around the 500 min mark may have led to the filter's divergence, particularly for the ranging and declination.

If the abrupt increase in error of the RF-only CN-optimized configurations is related to either of the last two reasons, then the objective function is unable to predict it. In order to facilitate the computation of the objective function, the orbital dynamics were reduced to the keplerian model. The SR-SFIM matrix is also built on the linearization of nonlinear dynamic and observation models, and does not measure the validity of this approximation.

5.3 Sensor-reduced system

In this section, Monte-Carlo simulations will be used to evaluate and compare the performance of the different optimized configurations for the relative-bearing reduced system. These results will also be compared with those from previous sections to evaluate the drop in performance due to the loss of relative bearing observations between the original formation. The measurement schedule from the previous section, shown in Table 5.3, is used. The simulation period is extended to 2 orbital periods of the original formation, so as to better assess the convergence of the filter, and also the relative position

converges slower in this system (from $\sim$ 200 to $\sim$ 1000 min, as seen in Figure 5.11). As a result of a doubled simulation period, the number of Monte-Carlo runs is cut in half ($M = 20$). The remaining aspects of the simulation are kept similar to the previous sections. The results are shown in Table 5.5.

			Absolute position mean error (km)	**Relative position mean error (m)**					
			$\overline{e}_{1,\mathrm{rms}}$	$\overline{e}_{2/1,\mathrm{rms}}$	$\overline{e}_{3/1,\mathrm{rms}}$	$\overline{e}_{4/1,\mathrm{rms}}$	$\overline{e}_{5/1,\mathrm{rms}}$	$\overline{e}_{6/1,\mathrm{rms}}$	$\overline{e}_{7/1,\mathrm{rms}}$	$\overline{e}_{2:6/1,\mathrm{rms}}$
RF/ vision		**CN**	3.599	6.484e−01	9.230e−01	1.048	1.129	8.338e−01	3.253	9.164e−01
		LUI	3.070	6.029e−01	8.612e−01	1.007	1.141	7.889e−01	4.439	8.802e−01
RF only	**Free period**	**CN**	12.61	1.494	2.618	3.526	2.722	1.827	7.930e+04	2.438
		LUI	3.376	6.494e−01	9.639e−01	1.091	1.216	8.119e−01	3.060e+03	9.465e−01
	Fixed period	**CN**	34.243	3.767	6.680	9.101	6.991	4.891	1.580e+05	6.286
		LUI	7.353	9.916e−01	1.489	1.852	1.852	1.474	7.723e+03	1.532

Table 5.5: Mean absolute and relative error for the different orbital configurations of the new observation spacecraft with the original formation measurement schedule minus the relative bearing measurements between the original formation elements

Once again, Figures 5.9(a), 5.9(b) and 5.9(c) show the bar plots of the Monte-Carlo averaged chief spacecraft absolute position RMS error $\overline{e}_{1,\mathrm{rms}}$, the formation's original deputy spacecraft mean relative positioning RMS error $\overline{e}_{2:6/1,\mathrm{rms}}$ and the new spacecraft's relative positioning RMS error $\overline{e}_{7/1,\mathrm{rms}}$, respectively.

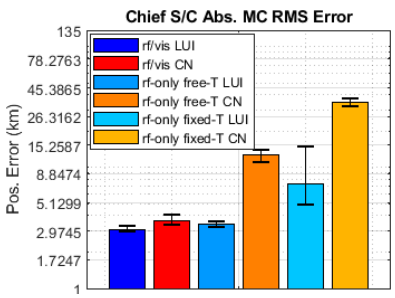

(a) Chief spacecraft absolute position Monte-Carlo averaged RMS error.

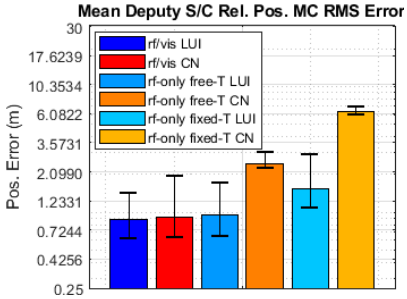

(b) Formation's deputy spacecraft mean relative position Monte-Carlo averaged RMS error (excluding the aux. spacecraft).

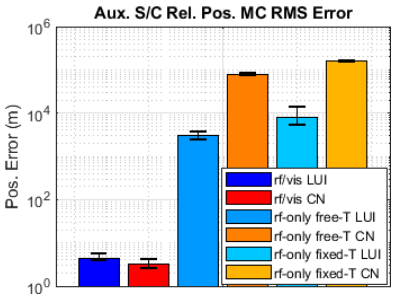

(c) Auxiliary spacecraft relative position Monte-Carlo averaged RMS error.

Figure 5.9: Monte-Carlo averaged RMS error results for the configurations with the sensor reduced system, with upper and lower error bounds.

The removal of the relative bearing measurements within the original formation leads to a general decrease in relative and absolute positioning accuracy. The results show the LUI-optimized configurations outperforming their CN-optimized counterparts in terms of absolute positioning accuracy. For the RF-only configurations, the relative positioning performance of the deputy spacecraft ($\overline{e}_{2:6/1,\mathrm{rms}}$) appears to be linked to the absolute positioning accuracy, since the configurations with lower absolute positioning accuracy also present a lower mean relative positioning accuracy. The differences in $\overline{e}_{2:6/1,\mathrm{rms}}$ between the different configurations are more pronounced as well. The RF-only free period configurations now outperform their fixed-period counterparts in positioning accuracy significantly. Despite the losses in accuracy, the formation still meets the relative positioning accuracy requirement of RMSE 3 m for all

configurations but the RF-only CN-optimized fixed period one, albeit with a lower margin.

The RF-only CN-optimized configurations continue to present the largest errors of all configurations, likely due to the discussed filter instability problems.

The absolute positioning error over time for every configuration is shown in Figure 5.10. For comparison, this figure also presents a plot of the absolute position error divergence that should be expected for the original formation with no auxiliary spacecraft and no relative bearing measurements. The prediction model estimation error plot is also included, akin to the one shown in previous figures.

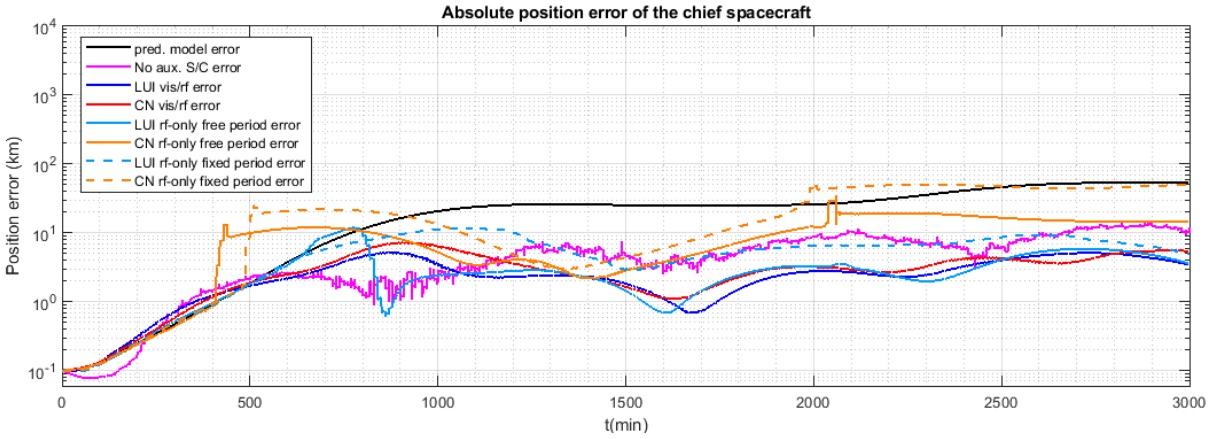

Figure 5.10: MC-averaged absolute position error of the chief spacecraft for each configuration with the parallel schedule and sensor-reduced system, compared with the single-simulation results from the formation with no relative bearing measurements or auxiliary spacecraft, and with the (MC-averaged) prediction model-only estimation.

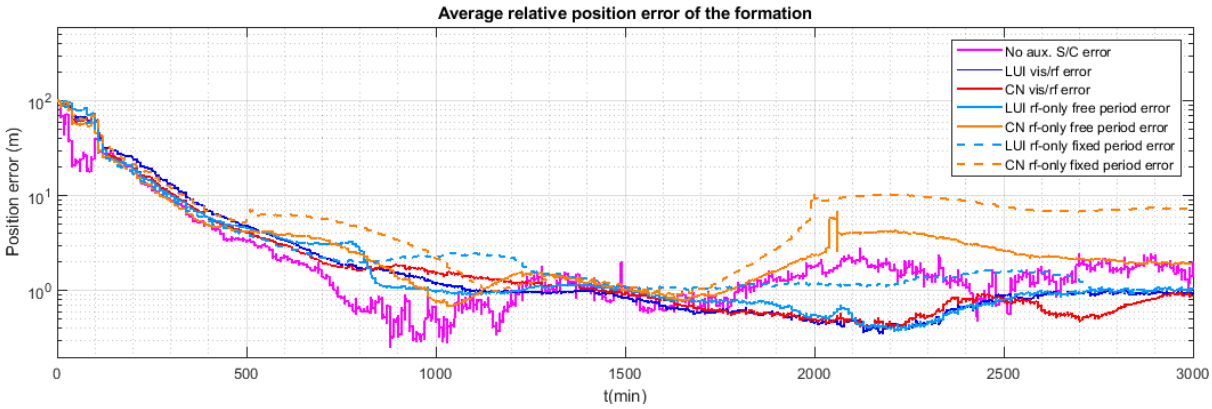

Figure 5.11: MC-averaged mean relative position error of the deputy spacecraft (not counting the added spacecraft) for each configuration with the parallel schedule and sensor-reduced system, compared with the single-simulation results from the formation with no relative bearing measurements or auxiliary spacecraft.

It is unclear from Figures 5.10 and 5.11 whether any of the shown positioning errors are converging. A longer simulation of 5 orbital periods was run for each of the configurations to better evaluate which of them are converging. The evolution of the relative positioning error within the original formation spacecraft of these simulations is shown in Fig. 5.12(a).

Figure 5.12(a) makes it more evident that the positioning error does not converge within the provided time frame in any configuration, with or without auxiliary spacecraft, when the relative bearing mea-

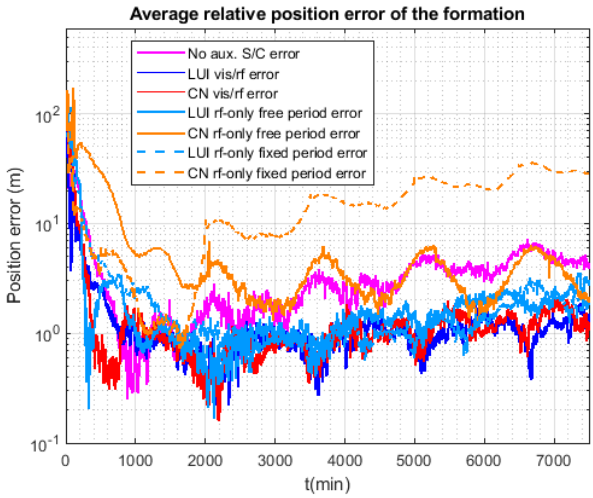

(a) Relative position error of the deputy spacecraft in the original formation of the sensor-reduced system configurations.

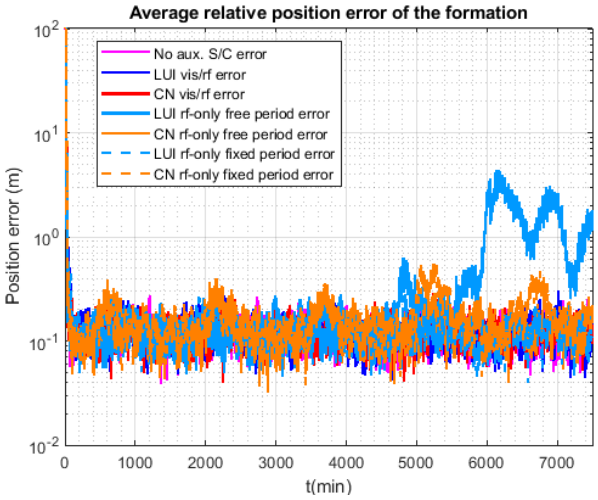

(b) Relative position error of the deputy spacecraft in the original formation of the parallel schedule configurations.

Figure 5.12: Single-simulation relative position error of the deputy spacecraft in the original formation over 5 orbital periodsfor the parallel schedule and sensor-reduced system configurations.

surements are removed from the deputy spacecraft in the original formation. The study in Section 4.2 showed the system to be observable but ill-conditioned. If the condition number of the state covariance matrix in the EKF goes beyond the floating point precision, the system becomes effectively unobservable. One potential solution would be to experiment with using square-root filters, which propagate the square-root of the state covariance matrix, of which the condition number is also the square-root of the original. These filters reduce numerical instability and could potentially allow for an ill-conditioned problem to become observable [74].

For comparison, a similar plot was drawn for the results in Section 5.2 with the parallel schedule in Fig. 5.12(b), in which only one configuration (the RF-only free-period LUI-optimized) appears to diverge at the end. This may be due to the asynchronicity between the original formation and the auxiliary spacecraft, which leads to the system having a time-variant performance that is hard to predict over extended periods of time. This could have been avoided by taking a different approach to the optimization of the free-period configurations, such as ensuring that the ratio between the orbital periods of the auxiliary spacecraft and the original formation is equal to a ratio of small integers to ensure periodicity under a short time frame.

Due to the long computation time of a simulation run, one of the main challenges of the optimization problem was choosing an objective function that would accurately reflect the performance of the simulation while being as easy to compute as possible. Several approximations were made that may have rendered the optimization problem more ineffective, such as:

- The reduction of the original formation to its chief spacecraft;
- The simplified measurement schedule;
- The approximation of the orbital dynamics to a keplerian model;
- The choice of the SR-SFIM, which reflects the inverse of the covariance of a weighted nonlinear

least squares filter rather than the EKF in question, and also does not account for second and higher-order nonlinearities in the dynamics or observations.

Besides these points, it is also important to understand whether or not the addition of the period factor f_{period} in the RF-only free-period optimization problems served its purpose or not. As mentioned in Section 4.1.3, f_{period} is a factor that is multiplied with the objective functions of the free-period SR-SFIM optimization problems to balance the increase in the amount of observations considered in the calculation of the SR-SFIM for the cases in which the orbital period of the new spacecraft is greater than that of the chief spacecraft.

In order to evaluate if this addition was beneficial to the results or not, the LUI and CN of the SR-SFIM are calculated for the dual spacecraft system of the chief spacecraft and an arbitrary deputy spacecraft from the original formation. These values are calculated for SR-SFIM's considering different simulation periods, ranging from the typical formation orbital period ($\sim 25\,\text{h}$) to 5 times its orbital period. The CN and LUI are plotted both with and without f_{period}, considering their measurement system to be the RF/Vision one. The resulting plots are shown in Figure 5.13.

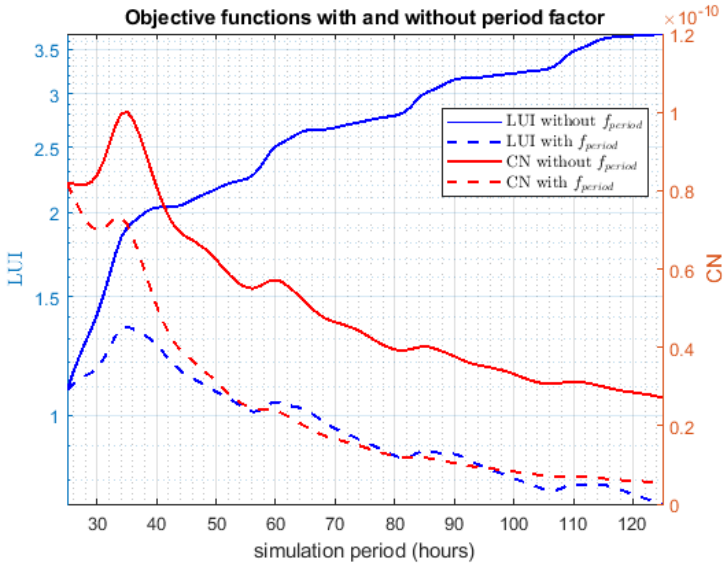

Figure 5.13: LUI and CN of the SR-SFIM calculated with different simulation periods, with and without f_{period}. The system is composed of the chief spacecraft and an arbitrary deputy spacecraft in the original formation, with their original measurement systems.

Figure 5.13 shows that, while the value of the LUI does increase with a greater simulation period and number of measurements, the CN does not. Even though the period factor helps to reduce the impact of the simulation period on the LUI, it could have been made more effective for this purpose. Perhaps adding an exponent to the factor ($f^a_{\text{period}}, a \in [0, 1]$) would have resulted in a flatter curve. In the case of the CN, it would have been better not to use a period factor entirely.

Chapter 6

Conclusions

As described in Section 1.2, this work focused on 3 main goals:

1. Implementation of the relative positioning autonomous navigation method as a localization solution for an existing spacecraft flying formation;

2. Study of the optimization of the positioning of a new spacecraft within the formation so as to maximize the performance of the new navigation method;

3. Study of the viability and performance of this system when stripped from its relative bearing measurement system.

Using the SunRISE mission as a template for the study, the results in Section 3 demonstrated that including the absolute position states and two-body dynamics into the filter results in better relative positioning accuracy than the PVA model initially proposed in [30] ($13\,\mathrm{cm}$ as opposed to $3.6\,\mathrm{m}$ mean RMS relative positioning error). The performance of the new filter, however, has the added need for an initial absolute position estimate, the accuracy of which influences the convergence speed of the filter. Compared with the performance of the chosen GPS-based solution, its absolute positioning RMS accuracy is worse by a factor of around ~ 1000, while its relative positioning RMS accuracy is better by a factor of ~ 10.

Regarding the study on the optimization of the orbital configuration of a new spacecraft so as to maximize the filter's absolute and relative positioning accuracy, the following conclusions were drawn from the results in Section 4:

- The use of the observability matrix with Lie derivatives up to $m = 3$ led to optimized configurations in line with the results shown in previous articles such as [11, 45], concluding that larger differences in orbital radius (or more correctly, in magnitude of gravitational acceleration) between spacecraft lead to better local observability of the absolute position;

- The comparison of results between the original formation's ability to perform autonomous navigation with and without the auxiliary spacecraft shows that the RF/Vision-based configurations may

be able to match or even slightly improve the absolute positioning accuracy of the original formation with no auxiliary spacecraft, whereas the RF-only configurations visibly worsen it;

- No configuration of the auxiliary spacecraft in either of the considered measurement schedules brought any substantial improvement to the relative positioning performance of the deputy spacecraft in the formation;
- The restriction of the orbital period of the new spacecraft to that of the original formation generally improved the performance of the system within the considered simulation time frame, going against the expectations established by the optimization results;
- The choice of objective function may not have been sufficiently adequate for this study in the following aspects: 1. It does not account for the deputy spacecraft in the formation; 2. It does not account for the measurement schedule; 3. Non-keplerian dynamics are not considered; 4. The choice of the SR-SFIM may not have been adequate, since it more accurately describes the performance of a batch WLS filter than that of the implemented EKF, and it also does not evaluate the second or higher order nonlinearities in the dynamics and observation models and the validity of the linearization approach; 5. The period factor f_{period} should not have been used in the CN-optimization problems, and could have been better designed for the LUI-optimization;
- The LUI-optimized configurations generally provided more accurate absolute positioning results than the CN-optimized ones;
- The asynchronicity between the RF-only free period auxiliary spacecraft and the original formation means that the performance of the free-period configurations is time-variant, and therefore unpredictable beyond the period considered in the optimization problem. The search space of these optimization problems should have been restricted to ensure orbital resonance between the spacecraft and therefore periodicity in their motion;

Finally, regarding the study on the observability and performance of the formation in question when deprived from the relative bearing measurements, the following observations can be made:

- The observability study provided evidence that a spacecraft system in which the deputy spacecraft only perform ranging measurements with the chief, while the latter also performs simultaneous relative range and bearing measurements with an auxiliary spacecraft should be observable, albeit ill-conditioned;
- The simulation results showed that the sensor-reduced system is too ill-conditioned for the EKF to converge, despite being theoretically observable.

6.1 Future Work

The localization method through relative positioning for spacecraft formations on which this study has focused shows great potential as an innovative, real-time and autonomous navigation solution for deep

space missions. Continuing research on this method should seek to further our knowledge of its potential performance and tackle the problematics that may compromise it. The following suggestions are left for a potential continuation of the line of work pursued in this thesis:

- A comparison needs to be done between the performance of filters with different state vectors and dynamics. When only relative positioning accuracy is important, the use of dynamic approximations such as the Hill–Clohessy–Wiltshire model may be more appropriate;
- The study of the RF-only CN-optimized configurations showed the EKF diverging, possibly due to the innacuracy of the chosen prediction model or to strong nonlinear behaviour. Testing other filters more robust to large variations in the algorithm's prediction model error [72], or better suited to handle nonlinearities such as the Unscented Kalman Filter [73] could potentially lead to better results;
- The removal of the relative bearing measurements within the original formation while maintaining those between the auxiliary and the chief spacecraft led to divergent EKF simulation results. It would be interesting to test whether a square-root filter would converge under the same conditions, as it would be better suited to handle a poorly-conditioned system [74];
- Other more appropriate objective functions should be considered for the new spacecraft configuration optimization problem. One suggestion that would account for the filter's process noise would be the use of the *Posterior Fisher Information Matrix* or PFIM [48];
- The approximation of the extended formation to a dual spacecraft system may have rendered the results of the optimization problem less valid, as well as the change in measurement schedule. A new approach to reduce the complexity of the computation of the objective function while maintaining the validity of the problem could prove useful for the continuation of this line of work;
- Some hypotheses were proposed to justify why the optimized orbital configurations could minimize the objective functions considered, such as the balance of the impact of measurement noise and absolute position observability. Providing empirical evidence to validate these hypotheses would help to understand the limitations of the potential accuracy of this method;
- This work adopted the simplification that all measurements within the formation are available to a central positioning system that performs the computation. In reality, the problem of the availability of measurements to a system and the distribution of computation must be discussed when proposing a positioning solution. This topic presents a line of work addressed by several recent studies [70, 75];
- The measurement noise in the ranging system is modeled as simple Gaussian white noise. More realistic models would incorporate biases such as antenna offsets, ionospheric error and time of flight, and the filtering algorithm should be designed to account for these.

Bibliography

[1] C. T. Fraser. *Adaptive Extended Kalman Filtering Strategies for Autonomous Relative Navigation of Formation Flying Spacecraft*. PhD thesis, Carleton University, 2019.

[2] G.-P. Liu and S. Zhang. A survey on formation control of small satellites. *Proceedings of the IEEE*, 2018.

[3] S. Nag, C. K. Gatebe, D. W. Miller, and O. L. De Weck. Effect of satellite formations and imaging modes on global albedo estimation. *Acta Astronautica*, 2016.

[4] G. Krieger, I. Hajnsek, K. P. Papathanassiou, M. Younis, and A. Moreira. Interferometric synthetic aperture radar (SAR) missions employing formation flying. *Proceedings of the IEEE*, 2010.

[5] P. Silvestrin, M. Aguirre, L. Massotti, B. Leone, S. Cesare, M. Kern, and R. Haagmans. The future of the satellite gravimetry after the GOCE mission. In *Geodesy for Planet Earth*. Springer, 2012.

[6] G. Di Mauro, M. Lawn, and R. Bevilacqua. Survey on guidance navigation and control requirements for spacecraft formation-flying missions. *Journal of Guidance, Control, and Dynamics*, 2018.

[7] L. Winternitz, B. Bamford, S. Price, A. Long, M. Farahmand, and R. Carpenter. GPS Navigation Above 76,000 km for the MMS Mission. In 39^{th} *Annual AAS Guidance, Navigation and Control Conference*, 2016.

[8] O. Montenbruck and E. Gill. *Satellite Orbits: Models, Methods, and Applications*. Springer Science & Business Media, 2000.

[9] S. Dutta and R. D. Braun. Statistical entry, descent, and landing performance reconstruction of the mars science laboratory. *Journal of Spacecraft and Rockets*, 2014.

[10] L. Markley. Autonomous navigation using landmark and intersatellite data. In *Astrodynamics conference*, July 1984.

[11] Y. Ou and H. Zhang. Observability-based mars autonomous navigation using formation flying spacecraft. *The Journal of Navigation*, 2018.

[12] M. L. Psiaki. Absolute orbit and gravity determination using relative position measurements between two satellites. *Journal of Guidance, Control, and Dynamics*, 2011.

[13] H. X. Yang, M. Vetrisano, M. Vasile, and W. Zhang. Autonomous navigation of spacecraft formation in the proximity of minor bodies. *Proceedings of the Institution of Mechanical Engineers, Part G: Journal of Aerospace Engineering*, 2016.

[14] K. Hill and G. H. Born. Autonomous interplanetary orbit determination using satellite-to-satellite tracking. *Journal of guidance, control, and dynamics*, 2007.

[15] J. R. Yim, J. L. Crassidis, and J. L. Junkins. Autonomous orbit navigation of two spacecraft system using relative line of sight vector measurements. In *Proceedings of the AAS Space Flight Mechanics Meeting*, 2004.

[16] J. Guinn and R. Boain. Spacecraft autonomous navigation for formation flying Earth orbiters using GPS. In *Astrodynamics Conference*, 1996.

[17] E. Canuto, C. Novara, D. Carlucci, C. P. Montenegro, and L. Massotti. *Spacecraft Dynamics and Control: The Embedded Model Control Approach*. Butterworth-Heinemann, 2018.

[18] M. G. Bernhardt, T. Prinz, W. Becker, and U. Walter. Timing X-ray Pulsars with Application to Spacecraft Navigation. In *High Time Resolution Astrophysics (HTRA) IV-The Era of Extremely Large Telescopes*. SISSA Medialab, 2011.

[19] S. Zhu, C. Reigber, and Z. Kang. Apropos laser tracking to GPS satellites. *Journal of Geodesy*, 1997.

[20] P. Teunissen and O. Montenbruck. *Springer handbook of global navigation satellite systems*. Springer, 2017.

[21] M. Ambrosini. GPS Precise Relative Positioning of Formation Flying Satellites. *The Journal of Space Operations & Communicator*, 2017.

[22] S. I. Sheikh, D. J. Pines, P. S. Ray, K. S. Wood, M. N. Lovellette, and M. T. Wolff. Spacecraft navigation using X-ray pulsars. *Journal of Guidance, Control, and Dynamics*, 2006.

[23] S. Shemar, G. Fraser, L. Heil, D. Hindley, A. Martindale, P. Molyneux, J. Pye, R. Warwick, and A. Lamb. Towards practical autonomous deep-space navigation using x-ray pulsar timing. *Experimental Astronomy*, 2016.

[24] L. Huang, P. Shuai, X. Zhang, and S. Chen. Pulsar-based navigation results: Data processing of the x-ray pulsar navigation-I telescope. *Journal of Astronomical Telescopes, Instruments, and Systems*, 2019.

[25] S. Shemar, G. Fraser, L. Heil, D. Hindley, A. Martindale, P. Molyneux, J. Pye, and R. Warwick. Feasibility and performance assessment of a practical autonomous deep space navigation system based on X-ray pulsar timing. *arXiv preprint arXiv:1805.05899*, 2018.

[26] E. Kaplan and C. Hegarty. *Understanding GPS: principles and applications*. Artech house, 2005.

[27] F. Nunes. Adaptive Robust Extended Kalman Filter for GNSS-Based Orbit Determination. Master's thesis, Instituto Superior Técnico, University of Lisbon, 2015.

[28] K. Alfriend, S. R. Vadali, P. Gurfil, J. How, and L. Breger. *Spacecraft formation flying: Dynamics, Control and Navigation*. Elsevier, 2009.

[29] R. Bevilacqua and T. Lovell. Analytical guidance for spacecraft relative motion under constant thrust using Relative Orbit Elements. *Acta Astronautica*, 2014.

[30] J. Stuart, A. Dorsey, F. Alibay, and N. Filipe. Formation flying and position determination for a space-based interferometer in GEO graveyard orbit. In *2017 IEEE Aerospace Conference*. IEEE, 2017.

[31] C. A. Kluever. *Space Flight Dynamics*. John Wiley & Sons, 2018.

[32] I. Newton. The Principia: Mathematical Principles of Natural Philosophy. *in Great Books of the Western World*, 2003.

[33] R. Van Der Hilst. Essentials of Geophysics, Chapter 2: The Earth's Gravitational Field, Sept. 2004.

[34] G. Bonin, N. Roth, S. Armitage, J. Newman, B. Risi, and R. E. Zee. CanX–4 and CanX–5 Precision Formation Flight: Mission Accomplished! In 29^{th} *Annual AIAA/USA Conference on Small Satellites*, 2015.

[35] S. Persson, P. Bodin, E. Gill, J. Harr, and J. Jörgensen. PRISMA- An autonomous formation flying mission. In *ESA Small Satellite Systems and Services Symposium (4S)*, 2006.

[36] R. W. Beard, J. Lawton, and F. Y. Hadaegh. A coordination architecture for spacecraft formation control. *IEEE Transactions on control systems technology*, 2001.

[37] S.-J. Chung and F. Hadaegh. Swarms of femtosats for synthetic aperture applications. In 4^{th} *International Conference on Spacecraft Formation Flying Missions and Technologies*, 2011.

[38] M. D&'Errico. *Distributed space missions for earth system monitoring*. Springer Science & Business Media, 2012.

[39] S. Deng, J. Liao, Z. R. Huang, M. Hella, and K. Connor. Wireless connections of sensor network using RF and free space optical links. In *Next-Generation Communication and Sensor Networks 2007*. International Society for Optics and Photonics, 2007.

[40] P. Sinogas. GAMALINK Intersatellite link. ESA AIM workshop, ESTEC, 2016.

[41] S. Wu, W. Chen, and C. Chao. The STU-2 CubeSat mission and in-orbit test results. In *Small Satellite Conference, no. SSC16-III-09*, Logan, UT, 2016.

[42] Z. Bartosiewicz. Local observability of nonlinear systems. *Systems & Control Letters*, 1995.

[43] R. Hermann and A. Krener. Nonlinear controllability and observability. *IEEE Transactions on automatic control*, 1977.

[44] A. J. Krener and K. Ide. Measures of unobservability. In *Proceedings of the 48^{th} IEEE Conference on Decision and Control (CDC) held jointly with 2009 28^{th} Chinese Control Conference*. IEEE, 2009.

[45] Y. Ou, H. Zhang, and J. Xing. Autonomous orbit determination and observability analysis for formation satellites. In *2016 35^{th} Chinese Control Conference (CCC)*. IEEE, 2016.

[46] J. Hahn and T. F. Edgar. An improved method for nonlinear model reduction using balancing of empirical gramians. *Computers & chemical engineering*, 2002.

[47] M. Niethammer, P. H. Menold, and F. Allgöwer. Parameter and derivative estimation for nonlinear continuous-time system identification. *IFAC Proceedings Volumes*, 2001.

[48] M. Rafieisakhaei, S. Chakravorty, and P. Kumar. On the use of the observability gramian for partially observed robotic path planning problems. In *Proceedings of 56^{th} IEEE Conference on Decision and Control*, 2017.

[49] K. A. Hill and G. H. Born. Autonomous orbit determination from lunar halo orbits using crosslink range. *Journal of Spacecraft and Rockets*, 2008.

[50] K. Hill, G. H. Born, and M. W. Lo. Linked, autonomous, interplanetary satellite orbit navigation (LiAISON) in lunar halo orbits. In *AAS/AIAA Astrodynamics Specialist Conference*, Lake Tahoe, CA, 2005. Citeseer.

[51] F. Alibay, J. C. Kasper, T. J. W. Lazio, and T. Neilsen. Sun Radio Interferometer Space Experiment (SunRISE): Tracking particle acceleration and transport in the inner heliosphere. In *2017 IEEE Aerospace Conference*. IEEE, 2017.

[52] G. Mao. *Localization Algorithms and Strategies for Wireless Sensor Networks: Monitoring and Surveillance Techniques for Target Tracking: Monitoring and Surveillance Techniques for Target Tracking*. IGI Global, 2009.

[53] P. Zarchan and H. Musoff. *Fundamentals of Kalman filtering: a practical approach*. American Institute of Aeronautics and Astronautics, Inc., 2013.

[54] Y. Zhu and A. Shareef. Comparisons of three kalman filter tracking algorithms in sensor network. In *2006 International Workshop on Networking, Architecture, and Storages (IWNAS'06)*. IEEE, 2006.

[55] R. G. Brown, P. Y. Hwang, et al. *Introduction to random signals and applied Kalman filtering*, volume 3. Wiley New York, 1992.

[56] P. Frogerais, J.-J. Bellanger, and L. Senhadji. Various ways to compute the continuous-discrete extended kalman filter. *IEEE Transactions on Automatic Control*, 2011.

[57] A. Beck. *Introduction to nonlinear optimization: Theory, algorithms, and applications with MATLAB*, volume 19. Siam, 2014.

[58] M. L. Psiaki. Autonomous orbit determination for two spacecraft from relative position measurements. *Journal of Guidance, Control, and Dynamics*, 1999.

[59] A. Klein and G. Mélard. Computation of the Fisher information matrix for time series models. *Journal of computational and applied mathematics*, 1995.

[60] J. Harr, M. Delpech, L. Lestarquit, and D. Seguela. RF metrology validation and formation flying demonstration by small satellites–the CNES participation on the PRISMA mission. In *Proceedings of the 4S symposium small satellites, systems and services, ESA SP-625*, 2006.

[61] D. Maessen and E. Gill. Relative state estimation and observability analysis for formation flying satellites. *Journal of Guidance, Control, and Dynamics*, 2012.

[62] M. Delpech, J.-C. Berges, T. Karlsson, and F. Malbet. Results of PRISMA/FFIORD extended mission and applicability to future formation flying and active debris removal missions. *International Journal of Space Science and Engineering*, 2013.

[63] S. D'Amico. Relative orbital elements as integration constants of Hill's equations. *German Space Operations Center (GSOC) TN*, 2005.

[64] H. Moritz. Geodetic reference system 1980. *Bulletin géodésique*, 1980.

[65] D. A. Vallado. *Fundamentals of Astrodynamics and Applications*. Springer Science & Business Media, 2001.

[66] J. Currie, D. I. Wilson, N. Sahinidis, and J. Pinto. OPTI: Lowering the barrier between open source optimizers and the industrial MATLAB user. *Foundations of computer-aided process operations*, 2012.

[67] I. Vaz and L. Vicente. A particle swarm pattern search method for bound constrained global optimization. *Journal of Global Optimization*, 2007.

[68] R. H. Byrd, J. C. Gilbert, and J. Nocedal. A trust region method based on interior point techniques for nonlinear programming. *Mathematical programming*, 2000.

[69] T. Qin, D. Qiao, and M. Macdonald. Relative Orbit Determination Using Only Intersatellite Range Measurements. *Journal of Guidance, Control, and Dynamics*, 2019.

[70] J. Wang and E. A. Butcher. Decentralized estimation of spacecraft relative motion using consensus extended Kalman filter. In *2018 Space Flight Mechanics Meeting*, 2018.

[71] J. Wang, E. A. Butcher, and T. Yucelen. Extended Kalman Filter and Observability Analysis for Consensus Estimation of Spacecraft Relative Motion. In *2018 AIAA Guidance, Navigation, and Control Conference*, 2018.

[72] S. Akhlaghi, N. Zhou, and Z. Huang. Adaptive adjustment of noise covariance in Kalman filter for dynamic state estimation. In *2017 IEEE power & energy society general meeting*. IEEE, 2017.

[73] L. Perea, J. How, L. Breger, and P. Elosegui. Nonlinearity in sensor fusion: divergence issues in EKF, modified truncated GSF, and UKF. In *AIAA Guidance, Navigation and Control Conference and Exhibit*, 2007.

[74] B. D. Anderson and J. B. Moore. *Optimal filtering*. Courier Corporation, 2012.

[75] K. Matsuka, E. Lupu, Y. Nakka, R. Foust, S.-J. Chung, and F. Hadaegh. Distributed multi-target relative pose estimation for cooperative spacecraft swarm. In 10^{th} *International Workshop on Satellite Constellations and Formation Flying (IWSCFF)*, 2019.

[76] M. Leomanni, G. Bianchini, A. Garulli, and A. Giannitrapani. A class of globally stabilizing feedback controllers for the orbital rendezvous problem. *International Journal of Robust and Nonlinear Control*, 2017.

[77] H. D. Curtis. *Orbital mechanics for engineering students*. Butterworth-Heinemann, 2013.

[78] Z. P. Olikara and K. C. Howell. Computation of quasi-periodic invariant tori in the restricted three-body problem. In *AAS/AIAA Space Flight Mechanics Meeting*, San Diego, CA, feb 2010.

[79] S. Hernandez, J. R. Stuart, D. M. Garza, S. B. Broschart, S. J. Herzig, and S. A. Chien. Satellite Constellation Orbit Design to Enable a Space-Based Radio Interferometer. In *Advances in the Astronautical Sciences AAS/AIAA Astrodynamics Conference 2017*. American Astronautical Soc. Springfield, VA, 2017.

[80] D. E. Gaylor, T. Berthold, and N. Takada. Java Astrodynamics Toolkit (JAT). In 28^{th} *Annual AAS Rocky Mountain Guidance and Control Conference-Guidance and Control 2005*, 2005.

[81] W. M. Folkner, J. G. Williams, D. H. Boggs, R. S. Park, and P. Kuchynka. The planetary and lunar ephemerides DE430 and DE431. *Interplanetary Network Progress Report*, 2014.

[82] L. F. Shampine and M. W. Reichelt. The Matlab ODE suite. *SIAM journal on scientific computing*, 1997.

Appendix A

Classical Orbital Elements

Within the two-body problem, the trajectory of a satellite orbiting a central body can be described by an ellipse when in an inertial frame centered around the main body, such as the ECI frame. The classical orbital elements first proposed by Kepler describe the shape, orientation and phase along that ellipse. Figure A.1 shows the 6 orbital elements: the semi-major axis a, the eccentricity e, the inclination i, the Right Ascension ot the Ascending Node (RAAN) Ω, the argument of the perigee ω and the true anomaly ν.

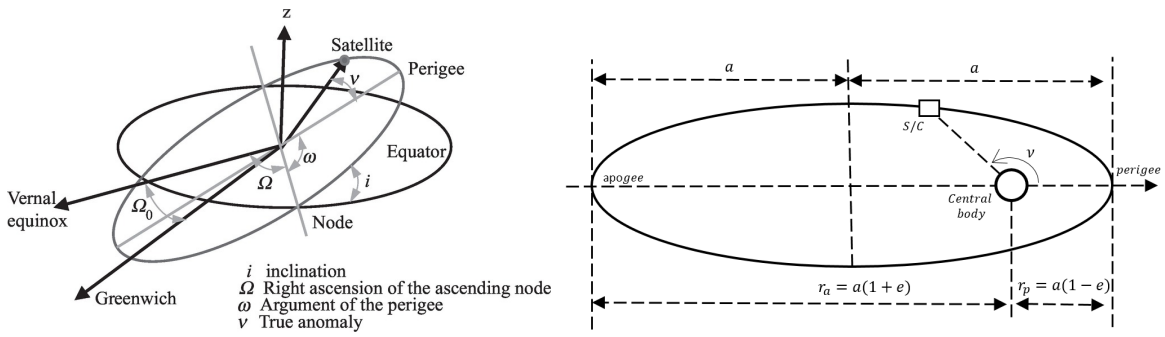

(a) Orientation classical orbital elements [76].

(b) Shape and phase classical orbital elements.

Figure A.1: Classical Orbital Elements.

The full set of orbital elements is denoted as

$$\text{œ} = \{a, e, i, \Omega, \omega, \nu\}. \tag{A.1}$$

A.1 Conversion between Cartesian and Keplerian states

Cartesian states and Keplerian elements are interchangeable, and both have their applications in this thesis. Relative position measurements are more easily described by cartesian states, and for that reason they are used in the filtering algorithms and simulations. The observability optimization problem, on the other hand, is more easily formulated (in terms of constraints and search space) with Keplerian elements. Conversion between these sets of states is therefore necessary, and is reviewed in this

section, using the algorithms described in detail in[77] and paraphrased from [1].

A.1.1 Orbital Elements to Cartesian States

From a given set of orbital elements œ such as the one in Eq. (A.1), the position and velocity vector within a perifocal frame[1] can be obtained as follows:

$$r_p = \frac{a(1-e^2)}{1+e\cos(\nu)} \begin{bmatrix} \cos(\nu) \\ \sin(\nu) \\ 0 \end{bmatrix}, \qquad v_p = \sqrt{\frac{\mu}{a(1-e^2)}} \begin{bmatrix} -\sin(\nu) \\ e+\cos(\nu) \\ 0 \end{bmatrix} \tag{A.2}$$

In order to change from the perifocal to the inertial frame, 3 rotations need to be made: first a rotation around the Z axis with the negative value of ω, followed by a rotation around the X axis with the negative value of i, with a final rotation around the Z axis with the negative value of Ω. These rotations are performed by sequentially multiplying the vectors in the perifocal frame with the rotation matrices that describe these rotations, which together describe the perifocal to inertial transformation matrix $Q_{p\to I}$:

$$Q_{p\to I} = R_Z(-\Omega)R_X(-i)R_Z(-\omega) \tag{A.3}$$

$$= \begin{bmatrix} \cos(\Omega) & -\sin(\Omega) & 0 \\ \sin(\Omega) & \cos(\Omega) & 0 \\ 0 & 0 & 1 \end{bmatrix} \begin{bmatrix} 1 & 0 & 0 \\ 0 & \cos(i) & -\sin(i) \\ 0 & \sin(i) & \cos(i) \end{bmatrix} \begin{bmatrix} \cos(\omega) & -\sin(\omega) & 0 \\ \sin(\omega) & \cos(\omega) & 0 \\ 0 & 0 & 1 \end{bmatrix} \tag{A.4}$$

We obtain the position and velocity vectors in the inertial frame by appling this transformation to the vectors in the perifocal frame:

$$r = Q_{p\to I} r_p \tag{A.5}$$

$$v = Q_{p\to I} v_p \tag{A.6}$$

A.1.2 Cartesian States to Orbital Elements

The semi-major axis a is the only COE directly linked to the orbit's specific energy, which is constant in a keplerian orbit. The specific energy ε can be used to obtain a from the position and velocity vectors r and v in the inertial frame according to the following expression:

$$\varepsilon = \frac{\|v\|^2}{2} - \frac{\mu}{\|r\|} = -\frac{\mu}{2a}. \tag{A.7}$$

[1]The perifocal frame is a frame of reference specific to a given orbit and centered on the primary, in which the X axis points towards the orbit's perigee, the Z axis is aligned and oriented according to its angular momentum vector, and the Y axis is the vector orthonormal to these two.

The specific angular momentum vector h, normal to the orbital plane, can be obtained according to

$$h = r \times v, \tag{A.8}$$

from which the eccentricity vector v_e can be obtained:

$$v_e = \frac{v \times h}{\mu} - \frac{r}{\|r\|}. \tag{A.9}$$

The eccentricity vector v_e points from the centre of mass of the central body to the perigee, and its magnitude $\|v_e\|$ provides the eccentricity e.

The inclination is defined as the angle between the orbit angular momentum vector and the Z axis in the inertial frame

$$i = \arccos\left(\frac{h_z}{\|h\|}\right), \tag{A.10}$$

where h_z is the component of h projected in the Z axis in the inertial frame. The RAAN defines the angle between the inertial X axis and the ascending node. To find this angle, it is necessary to first find the nodal vector n, which points at the ascending node in the inertial frame. This vector is defined as:

$$n = Z_{ECI} \times h. \tag{A.11}$$

The RAAN is then calculated as

$$\Omega = \arctan 2\left(n_y, n_x\right), \tag{A.12}$$

where n_x and n_y are the components of n projected in the X and Y axis in the inertial frame, respectively.

The argument of the perigee can be obtained from the nodal and eccentricity vectors:

$$\omega = \arccos\left(\frac{n \cdot v_e}{\|n\| e}\right) \tag{A.13}$$

being that if $e_z \geq 0$ then ω should be in the first 2 quadrants, otherwise it should be on the last two.

The last element to be obtained is the true anomaly ν. To obtain the latter, we must first calculate the argument of latitude $u = \omega + \nu$. This element describes the angle between the nodal vector n and the position vector r, and can be obtained from the following expression:

$$u = \arccos\left(\frac{N \cdot r}{\|N\|\|r\|}\right). \tag{A.14}$$

The quadrant of u is determined from the component of r in the Z axis of the inertial frame: if it is positive, then it is in the first 2 quadrants; if it is negative, it is in the last two. The true anomaly can then be obtained from u and ω.

Appendix B

SunRISE Orbit Design

The orbit chosen for the SunRISE formation is known as “GEO graveyard orbit”, where spacecraft are safely decommissioned. Therefore, once the mission’s operations come to a close, there would be no need to perform additional maneuvers as the formation would already be in its final disposal orbit. The chief orbit is therefore circular with no inclination, sitting at a constant orbital radius of 43 399 km [51]. *Dynamical Systems Theory* was used to define the spatial arrangement of the spacecraft around this orbit due to its flexibility, since the design process can adapt to changes in the underlying dynamical regime and baseline orbit without need for extensive modification [30]. In order to simulate the motion of the formation, the constellation design method had to be replicated.

Dynamical Systems Theory

DST is based on the linearization of motion around a baseline trajectory, in this case the chief orbit. This motion consists in the propagation of a satellite’s set of position and velocity states through two-body dynamics, as described by the following set of first-order nonlinear differential equations:

$$\begin{bmatrix} \dot{r} \\ \dot{v} \end{bmatrix} = \begin{bmatrix} v \\ -\mu \dfrac{r}{\|r\|^3} \end{bmatrix} \tag{B.1}$$

Motion relative to said trajectory is linearized, resulting in the following system:

$$\dot{x} = A(t)x \Leftrightarrow \begin{bmatrix} \dot{\delta r} \\ \dot{\delta v} \end{bmatrix} = \begin{bmatrix} 0 & I \\ G & 0 \end{bmatrix} \begin{bmatrix} \delta r \\ \delta v \end{bmatrix} \tag{B.2}$$

with G the gravity gradient tensor defined in 2.33a. The propagation of this linearized motion along a trajectory can be done through the state transition matrix (STM), $\Phi_{t_0}(t)$, which maps changes from the initial states at time t_0 to the states at time t via

$$\delta x(t) = \Phi_{t_0}(t)\delta x(t_0) \tag{B.3}$$

with the STM itself being propagated as

$$\dot{\Phi}_{t_0}(t) = A(t)\Phi_{t_0}(t) \tag{B.4}$$

with initial conditions

$$\Phi_{t_0}(t_0) = I_{6\times 6}. \tag{B.5}$$

The STM may be also referred to as the *monodromy matrix* when it maps the propagation of states for a closed orbital period T after which $x(t_0+T) = x(t_0)$. The stability of the orbit is characterized by the eigenvalues γ_i of the *monodromy matrix*, and their associated eigenvectors $\hat{\Gamma}_i$ can be used to excite the corresponding relative motion. Unstable motion is described by an eigenvalue with magnitude $|\gamma_i| > 1$, and exciting its corresponding eigenvector will lead to an orbit that asymptotically drifts from the baseline orbit along the unstable manifold. Variations in the orbital initial conditions of a deputy spacecraft due to induced perturbations in these eigenvalue/eigenvector pairs are described as

$$x_0^*(\tau) = x_0(\tau) + u(\tau, \theta, \varepsilon) \tag{B.6}$$

where τ is a time-like parameter specifying the position along the baseline orbit and u is a step into the invariant manifold space. The manifold step for a single eigenvector $\hat{\Gamma}_i$ is

$$u(\tau, \theta_i, \varepsilon_i) = \varepsilon_i \left(\cos(\theta_i)\Re[\hat{\Gamma}_i(\tau)] - \sin(\theta_i)\Im[\hat{\Gamma}_i(\tau)]\right) \tag{B.7}$$

where ε_i is the step magnitude, θ_i is an angular parameter and $\Re$ and $\Im$ are the real and imaginary components of the complex vector, respectively. ε_i is allowed by convention to encompass both negative and positive values while θ_i is restricted to the interval $[0°, 180°]$. The mathematical basis of the manifold step is now generalized to allow linear combinations of the eigenvectors, that is:

$$u(\tau, \theta, \varepsilon) = \sum_{i=1}^{n} \varepsilon_i \left(\cos(\theta_i)\Re[\hat{\Gamma}_i(\tau)] - \sin(\theta_i)\Im[\hat{\Gamma}_i(\tau)]\right). \tag{B.8}$$

This formulation allows for the selective perturbation of the relative motion of a trajectory around the baseline orbit, resulting in an intricate combined manifold motion. For the considered chief orbit, $|\gamma_i| = 1$ for all six eigenvalues, which indicates the manifold's stability and the presence of an invariant torus [78]. However, of the six eigenvectors, two form a complex conjugate pair and another two are repeated strictly real vectors (this latter repetition of eigenvectors indicates that the monodromy matrix is degenerate). The remaining two are unique and strictly real. Thus, Eq. (B.8) can be rewritten as

$$u(\varepsilon, \theta) = \varepsilon_1\hat{\Gamma}_1 + \varepsilon_2\hat{\Gamma}_2 + \varepsilon_3\hat{\Gamma}_3 + \varepsilon_4 \left(\cos(\theta_4)\Re[\hat{\Gamma}_4] - \sin(\theta_4)\Im[\hat{\Gamma}_4]\right) \tag{B.9}$$

without losing the ability to exploit the entirety of the invariant manifold space. τ was omitted from the equation as the orbits are periodic, and therefore the motion of the spacecraft is cyclical. Any periodic relative trajectory around the baseline orbit can be equally generated from initial conditions set at any

given τ, and so the latter can be defined arbitrarily. The same $\tau = 0$ as proposed in [30] was chosen, which is the location of the orbit corresponding to $x_0 = [43399km, 0, 0, 0, 3.0306km/s, 0]^T$. The 6-element vector defining the initial condition of a spacecraft within the formation can therefore be characterized by using the set of parameters $[\varepsilon_1, \varepsilon_2, \varepsilon_3, \varepsilon_4, \theta_4]^T$ in eq. (B.9), variations of which will not change the orbital energy and therefore provoke drift over time when considering two-body dynamics [30].

The eigenvectors $\hat{\Gamma}_i$ are defined in table B.1 below.

i	$\hat{\Gamma}_{i/x}$	$\hat{\Gamma}_{i/y}$	$\hat{\Gamma}_{i/z}$	$\hat{\Gamma}_{i/\dot{x}}$	$\hat{\Gamma}_{i/\dot{y}}$	$\hat{\Gamma}_{i/\dot{z}}$
$\hat{\Gamma}_1$	0	1	0	-0.0001	0	0
$\hat{\Gamma}_2$	-0.8165	0.5774	0	0	0.0001	0
$\hat{\Gamma}_3$	0.8165	0.5774	0	0	-0.0001	0
$\hat{\Gamma}_4$	0	0	1	0	0	-0.0001i

Table B.1: Monodromy matrix's eigenvectors used for the invariant manifold for formation design.

Each of these vectors excites a different type of relative motion. The effect of each eigenvector on the resulting relative motion is shown in Figure B.1, in which they are separately excited (with $\varepsilon_1 = \varepsilon_4 = -\varepsilon_2 = -\varepsilon_3$).

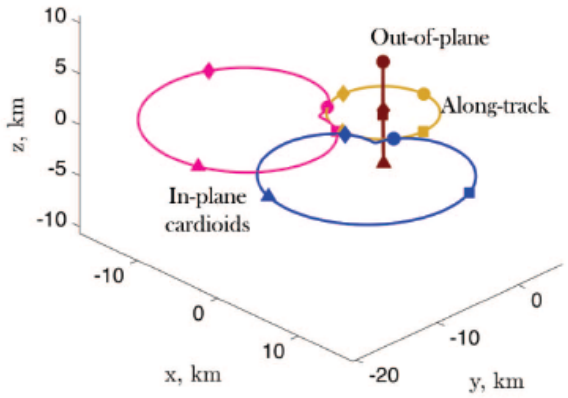

Figure B.1: Relative trajectories arising from the separate perturbation of the eigenvectors of the monodromy matrix, shown in the LI frame. The circles indicate the start of propagation, diamonds $1/4$, triangles $1/2$, and squares $3/4$ of the orbit [30].

In figure B.1, $\hat{\Gamma}_1$ describes the along-track motion, $\hat{\Gamma}_2$ the blue in-plane cardioid, $\hat{\Gamma}_3$ the pink in-plane cardioid, and $\hat{\Gamma}_4$ the out-of-plane motion. Since the optimized parameters from [30] were not available, an alternative set of parameters was used to define the initial condition θ of each of the six spacecraft in the formation. These parameters are described in table B.2 (provided in [79]).

S/C	$\varepsilon_1(km)$	$\varepsilon_2(km)$	$\varepsilon_3(km)$	$\varepsilon_4(km)$	$\theta_4(^\circ)$
1	3	0	2	2.5	150
2	0	-2	2	2	240
3	-2.5	-2	0	3	60
4	-2	0	-2.5	3	180
5	0	2	-2	2	300
6	3	2.5	0	3	120

Table B.2: Set of eigenvector excitation parameters.

With the eigenvectors from table B.1, the parameters from table B.2, Eqs. (B.6) and (B.9) are used to obtain the initial states of the formation in the ECI frame, shown in table B.3.

S/C	$u(t_0,\theta)_x(km)$	$u(t_0,\theta)_y(km)$	$u(t_0,\theta)_z(km)$	$u(t_0,\theta)_{\dot{x}}(m/s)$	$u(t_0,\theta)_{\dot{y}}(m/s)$	$u(t_0,\theta)_{\dot{z}}(m/s)$
1	1.6330	4.1547	-2.1651	-0.1289	-0.1140	0.0873
2	3.2660	0	-1	0	-0.2281	-0.1210
3	1.6330	-3.6547	1.5	0.0939	-0.1140	0.1814
4	-2.0412	-3.4434	-3	0.0389	0.1425	0
5	-3.2660	0	1	0	0.2281	-0.1210
6	-2.0412	4.4434	-1.5	-0.1087	0.1425	0.1814

Table B.3: Variations in the orbital initial condition with respect to the chief orbit for each spacecraft in the formation.

These initial states, propagated across one orbit with two-body dynamics in the Local Inertial and LVLH frame are illustrated in the relative orbits in figure B.2.

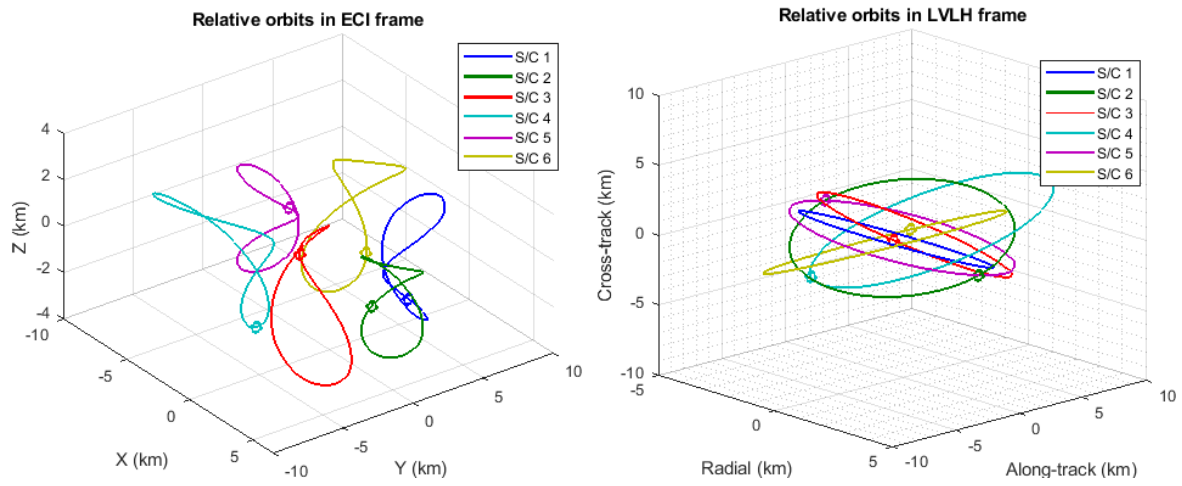

(a) Example configuration in the LI frame centered on the chief orbit.

(b) Example configuration in the LVLH frame centered on the chief orbit.

Figure B.2: Example configuration for the SunRISE flying formation. The dots mark the initial states of each spacecraft.

Appendix C

Orbit propagation

Having defined the initial states of the formation, these ought to be propagated with a model as accurate as possible. The propagated states will provide the baseline trajectory for the simulation, testing and validation of the filtering algorithms. For the simulation and numerical integration of the orbit dynamics described in section 2.1.3, NASA Goddard Space Flight Center's open source *ODTBX* (Orbit Determination Toolbox) was used [1]. *ODTBX* is a *MATLAB* Toolbox that uses *JAT* (JAVA Astrodynamics Toolbox) as a tool for orbital numerical propagation [80]. In this section, a brief description will be made on the methods used by *JAT* to simulate and compute these dynamics.

Geopotential Model

The most significant deviation from the two-body problem at GEO is due to the asymmetrical gravity field of the Earth. Current Earth gravity models are characterized by the accuracy of their gravity potential zonal and tesseral terms, as well as their degree and order.

ODTBX's default choice is the *EGM96*, which is an updated version of the *WGS84* with equal ellipsoid (shape of the Earth's spheroid) but more accurate geoid (mass distribution anomalies along the surface)[2]. This model was therefore chosen, with coefficients going up to degree and order 20.

Third-body gravity

The most significant sources of gravitational force on an Earth-orbiting satellite other than the Earth itself are the Moon and the Sun.

In order to simulate the gravity acceleration of these bodies on the formation's satellites, it is necessary to have their position available at all times within the simulation. *JAT* uses NASA' JPL *DE405* ephemeris for this purpose. Although these are not the most precise ephemeris currently available (the latest JPL ephemeris with fully consistent treatment of planetary and lunar laser ranging data is *DE430* [81]), it is sufficiently accurate for this purpose.

[1] `http://odtbx.sourceforge.net/` (Last accessed 18/06/2020)
[2] `https://earth-info.nga.mil/GandG/publications/tr8350.2/tr8350_2.html` (Last accessed 25-03-2020)

Solar pressure

JAT includes solar pressure into the perturbations that can be calculated within its orbit determination capabilities. It uses the canonball model with partial illumination described in section 2.1.3, which requires the mass m, cross-sectional area exposed to solar radiation S and reflectivity coefficient C_r. The mass of each spacecraft was set to $6\,\mathrm{kg}$ and its exposed surface to $0.14\,\mathrm{m}^2$ according to the information provided on the SunRISE mission in [51]. The coefficient of reflection C_r is dependent on the types of materials used on the surface of the spacecraft, and is typically within the range of $1.2 < C_r < 1.9$ for operational spacecraft [8]. For this simulation, C_r was arbitrarily set at 1.5.

All of the aforementioned non-keplerian dynamics are time-variant (the Earth's position with respect to the Sun affects the solar pressure, the Earth's rotation with respect to the ECI frame affects the asymmetrical gravity field, etc). The simulated true trajectories are all set to begin at the arbitrarily chosen date of 1-Oct-2008 $9\,\mathrm{h}\ 27\,\mathrm{min}\ 52\,\mathrm{s}\ 832\,\mathrm{ms}$. Using the previously mentioned JPL ephemeris, the trajectories of the considered bodies are defined for the simulation period.

Atmospheric drag

Despite atmospheric drag not being a considerable source of acceleration in near-GEO, some of the auxiliary spacecraft (the RF-only CN-optimized configurations) both present a periapsis low enough to justify its inclusion in the orbit propagation. We consider a canonball model such that the cross-sectional surface A facing the atmosphere is constant and the drag coefficient C_D is not affected by the spacecraft's orientation. We consider A to be equal to S ($0.14\,\mathrm{m}^2$). The drag coefficient lies tipically in the $1.5 - 3.0$ range [8]. The default value of 2.2 in the *ODTBX* Toolbox was arbitrarily chosen. Finally, the Harris-Priester Density Model was used to obtain ρ for altitudes in the $100 - 2000\mathrm{km}$ range, beyond which the drag force is not considered.

Numerical integration

MATLAB presents a number of inbuilt numerical integrators in its *ODE suite* [82]. For the purpose of orbit propagation, *ODE113* was chosen. *ODE113* is a multi-step solver based on a a PECE (Predict–Evaluate–Correct–Evaluate) implementation of Adams-Bashforth-Moulton methods, and is recommended by MATLAB for when the function to be propagated is expensive to evaluate, or for smooth problems with high precision requirements, such as orbital dynamics and celestial mechanics problems[3]. *MATLAB* allows for the definition of the relative and absolute tolerance of the numerical integration, which is set at $1\mathrm{e}{-3}$ and $1\mathrm{e}{-6}$ respectively by default, although in this scenario the values were set to $3\mathrm{e}{-14}$ and $1\mathrm{e}{-20}$, respectively, for increased accuracy.

[3] `https://blogs.mathworks.com/loren/2015/09/23/ode-solver-selection-in-matlab/` (Last accessed on 29-08-2020)

Appendix D

Optimization/EKF parameters

D.1 Optimization problem configuration

Tables D.1 and D.2 show the configuration parameters of the optimization algorithms that were changed from their default values for the *fmincon* and PSO optimization problems, respectively. Both RF/Vision LUI and CN-optimization algorithms were configured similarly, even though the values being optimized are in completely different value ranges. Rather than reconfiguring *fmincon*, the CN function was multiplied by a factor of $1\mathrm{e}{+10}$ such that the optimization would occur within a similar objective function value range. The resulting CN-optimized objective function was then divided by that same factor.

Table D.3 shows the initial optimal solution estimates provided to the optimization algorithms. It is worth noting that, for the RF-only configurations, the values of the COE of the initial estimates x_0 are very close to those of the final optimized solutions shown in Table 4.1. These initial estimates were obtained from previous optimizations of these same problems with minor differences in the objective function and search space. These optimization problems were re-launched to test whether the algorithm would converge to better minima, and the results presented only minor variations ($< 1\%$ in the objective function).

		Max. Func. Evals	**Step Tolerance**	**Function Tolerance**	**Multistart Max. Iter.**	**Max. Time (h)**
RF/Vision	**LUI-opt.**	$1\mathrm{e}{+04}$	$1\mathrm{e}{-07}$	$1\mathrm{e}{-06}$	$1\mathrm{e}{+04}$	8
SR-SFIM	**CN-opt.**	$1\mathrm{e}{+04}$	$1\mathrm{e}{-07}$	$1\mathrm{e}{-06}$	$1\mathrm{e}{+04}$	8

Table D.1: Non-default configuration parameters of the *fmincon* optimization problems.

			Max. Func. Evals	Max Nodes	Max Iter	Swarm Size	Max Time (h)
Observability Matrix		**LUI-opt.**	1e+06	1e+05	1e+04	300	8
		CN-opt.	1e+06	1e+05	1e+04	300	8
RF-Only SR-SFIM	**Free period**	**LUI-opt.**	1e+06	1e+05	1e+04	1000	8
		CN-opt.	1e+06	1e+05	1e+04	1000	8
	Fixed period	**LUI-opt.**	1e+06	1e+05	1e+04	1000	8
		CN-opt.	1e+07	1e+06	1e+05	2000	8

Table D.2: Non-default configuration parameters of the PSO optimization problems.

			Initial S/C states x_0						$f(x_0)$
			$a(km)$	e	$i(rad)$	$\Omega(rad)$	$\omega(rad)$	$\nu(rad)$	
Observability Matrix		**LUI-opt.**	87470.724	0	3.02	6.28	6.28	0	−4.27e−09
		CN-opt.	87470.724	0	3.02	6.28	6.28	0	−4.27e−09
RF/Vision SR-SFIM		**LUI-opt.**	43399	5.34e−03	1.91e−03	0	0	0	−4.17
		CN-opt.	43399	3.81e−04	1.07e−02	0	0	0	−1.04e−09
RF-Only SR-SFIM	**Free period**	**LUI-opt.**	40050.22	0.39	1.57	6.28	2.74	2.89	−4.17e−02
		CN-opt.	45864.67	0.85	1.41	3.75	4.86	3.39	−9.19e−12
	Fixed period	**LUI-opt.**	43399	0.364	0.33	1.58	2.62	2.08	−4.17e−02
		CN-opt.	43399	0.84	1.56	3.46	4.97	3.32	−9.31e−12

Table D.3: Initial states provided to the optimization problems.

D.2 EKF Q Matrix Parameters

Table D.4 shows the chosen α_1 and α_{new} parameters for each of the configurations with an optimized auxiliary spacecraft shown in the results in Chapter 5.

	Adapted schedule		**Parallel schedule**		**Sensor reduced**	
	α_1	α_{new}	α_1	α_{new}	α_1	α_{new}
RF/vis LUI	1e+06	1e+04	1e+06	1e+04	1e+01	1e+01
RF/vis CN	1e+06	1e+04	1e+06	1e+04	2.5e+01	1e+02
RF-only free-T LUI	1e+05	1e+07	2.5e+05	2.5e+07	1	1e+05
RF-only free-T CN	1e−02	1e+08	1e−02	1e+06	1e−02	1e+06
RF-only fixed-T LUI	1e+06	1e+06	1e+06	1e+07	1e+04	1e+05
RF-only fixed-T CN	1e−02	1e+08	1e−02	1e+08	1e−02	1e+06

Table D.4: EKF's process covariance matrix α_1 and α_{new} parameters.